Eindhoven University of Technology

MASTER

Design of a slotless linear permanent-magnet tubular actuator

Smetsers, R.C.J.

Award date:
2006

Link to publication

TU/e technische universiteit eindhoven

Capaciteitsgroep Elektrische Energietechniek
Electromechanics & Power Electronics

Master of Science Thesis

Design of a Slotless
Linear Permanent-Magnet
Tubular Actuator

R.C.J. Smetsers
EPE.2006.A.03

Coach:
dr. E.A. Lomonova

Eindhoven, June 6, 2006

/ faculteit elektrotechniek

I Abstract

A tubular linear actuator is designed for a novel actuation system in the pick-and-place machines of Assembléon in cooperation with Eindhoven University of Technology (TU/e). The main goal of the design study was to build an actuation system with the same output specifications as the system that is currently used, but can be placed twice in the volume that is currently occupied.

The tubular motor has a rotation symmetric configuration. The mover consists of axially magnetised permanent magnets separated from each other by iron inter-spacer rings. Through the centre of the mover, an iron inner rod is placed that provides stability to the mover. This configuration makes the mover easy and cheap to build. The stator consists of airgap winding coils (no slotting) separated from each other by small insulator rings. The coils are placed inside an iron tube. The only difficult part in the stator configuration is the connection of the coils.

After an initial analysis, the actuator is modelled by means of a magnetic equivalent circuit (MEC). The MEC model calculates the flux in different parts of the actuator, saturation of the iron and most important the (statically) produced force as a function of the configuration. MEC allows fast calculations to get a proper understanding how configuration changes influence the actuator behaviour.

For verification of the MEC model, the finite element method (FEM) is used for creating a numerical model. The FEM model is a 2D axial symmetric model constructed with the software package: Maxwell by Ansoft. FEM is also used to obtain more information on the tubular actuator configuration, and to predict the measurements carried out on a test set-up.

A test set-up has been built. With this set-up, the EMF of the actuator is measured and the force is estimated as a function of the mover displacement. A thermal measurement is also carried out on the test set-up.

The tubular actuator design is optimised for (static) force production. This process starts with determining the goal of the design process. Expected dimensions and output specifications are derived. After the actuator dimensions are set, the coil configuration is estimated.

II Preface

Assembléon is a producer of pick-and-place machines located in Veldhoven. Assembléon is formerly known as Philips Electronics Manufacturing Technology (EMT). Within the Assembléon organisation there is a constant drive to increase machine productivity and lower the cost per placement to serve the customers. R&D at Assembléon reflected the idea of changing one unit in the machine, responsible for a linear and rotary movement. The solution would be found in the electromechanical design of the unit, in other words, creating a next generation model. With little experience and knowledge in this area, Assembléon turned to the Technical University of Eindhoven (TU/e) for assistance. It was found at the Electromechanics and Power Electronics group (EPE) at the Department of Electrical Engineering (TU/e). Initial conversations between Assembléon and TU/e resulted in this project, entitled:

"Design of a Slotless Linear Permanent Magnet Tubular Actuator"

The project is a cooperation between Assembléon and the Technical University of Eindhoven (TU/e). The first phase of the project was organised as an internship. This internship dealt with a study towards possible concepts that met the demand of Assembléon. After the internship, of which the results will be treated briefly in this report, the graduation project was started. This project contains the modelling of a part of one of the concepts developed in the first phase, the building of a test set-up, and the evaluation of models and test results.

I would like to thank Dr. Elena Lomonova, and ir. Rik van der Burg for creating the possibility to complete my Master of Science project in the field of electromechanics. I also want to thank both for their support, ideas and comments on the thesis.

I am grateful to prof.dr.ir. André Vandenput for his motivation and his comments.

I also would like to thank Marijn Uyt De Willigen and the technical service of Assembléon for building the test set-up.

Furthermore, I would like to thank all the other people that helped me during the project.

III Contents

IV List of symbols

Symbol	Description	Dimension
a	Acceleration	$[ms^{-2}]$
A	Area	$[mm^2]$
a_{norm}	Normalised mover acceleration	$[ms^{-2}]$
A_p	Airgap area (per pole)	$[mm^2]$
at	Linear movement acceleration	$[ms^{-2}]$
B	Airgap flux density (or magnetic loading)	$[T]$
B_r	Magnet remanence	$[T]$
c_1	Scaling constant for the force and electric loading	$[Am^{-2}]$
c_2	Scaling constant for the acceleration	$[kgm^{-2}]$
D_{act}	Diameter of the actuator	$[mm]$
D_{cm}	Mean diameter of the coils	$[mm]$
D	Diameter	$[mm]$
E	Electric field strength	$[Vm^{-1}]$
$\hat{e}_c$	EMF amplitude per coil	$[V]$
$\hat{e}_{ll}$	Line voltage amplitude	$[V]$
E_{rms}	RMS phase voltage	$[V]$
e_{sc}	Scaling factor for radiation	$[\ ]$
F	Force	$[N]$
$\mathcal{F}$	Magneto Motive Force (MMF)	$[A]$
F_{norm}	Normalised force	$[N]$
F_{res}	Force resultant	$[N]$
H	Magnetic field strength	$[Am^{-1}]$
H_c	Magnet coercivity	$[Am^{-1}]$
I	Current	$[A]$
$\hat{i}$	Current amplitude	$[A]$
i_{max}	Maximal supply current	$[A]$
I_{rms}	RMS phase current	$[A]$
I_w	Winding current	$[A]$
J	Current density	$[Amm^{-2}]$
jr	Rotational movement jerk	$[revs^{-3}]$
jt	Linear movement jerk	$[ms^{-3}]$
k	Thermal conductivity	$[JK^{-1}m^{-1}s^{-1}]$
k_E	EMF constant	$[Vsm^{-1}]$
k_F	Force constant	$[NA^{-1}]$
L	Mover section length ($= \tau_p$)	$[mm]$
l	Length	$[mm]$
l_{tm}	Mean length of a turn	$[mm]$
l_{wire}	Wire length	$[mm]$
m	Mass	$[kg]$
N	Number of conductors per winding	$[\ ]$
n_{acw}	Number of coils per winding in which the EMF is induced	$[\ ]$
n_{atw}	Number of turns per winding in which the EMF is induced	$[\ ]$
n_{cw}	Number of coils per winding	$[\ ]$
n_m	Number of magnets on the mover	$[\ ]$
n_{ph}	Number of phases	$[\ ]$
n_{tc}	Number of turns per coil	$[\ ]$
n_{wr}	Number of windings in radial direction	$[m^{-1}]$
n_{wz}	Number of windings per meter of stator length	$[m^{-1}]$

P	(output) Power	$[W]$
P_{elec}	(Total) Electric power	$[W]$
$P_{loss,copper}$	Copper loss	$[W]$
Q	Electric loading (= ampere conductors per meter)	$[Am^{-1}]$
Q_{hf}	Heat flow	$[Js^{-1}]$
$\mathcal{R}$	Reluctance	$[H^{-1}]$
R	Resistance	$[\Omega]$
r_2	Inner rod radius	$[mm]$
r_4	Mover radius	$[mm]$
r_5	Inner radius of the coils	$[mm]$
r_6	Inner radius of the outer iron (= outer radius of the coils)	$[mm]$
r_8	Outer radius of the tubular actuator	$[mm]$
r_c	Mean radius of the coil	$[mm]$
R_{el}	Electric resistance	$[\Omega]$
r_i	Inner radius of a radial flux tube	$[mm]$
r_j	Outer radius of a radial flux tube	$[mm]$
$\mathcal{R}_m$	Magnetic reluctance	$[H^{-1}]$
r_{mc}	Mean radius of the coils	$[mm]$
T	Temperature	$[K]$
t_{at}	Time for constant (maximal) acceleration	$[s]$
t_{jt}	Time to go from 0 to maximal acceleration	$[s]$
t_{vt}	Time for constant (maximal) velocity	$[s]$
v	Speed	$[ms^{-1}]$
$V_{DC,s}$	DC supply voltage	$[V]$
V	Volume	$[m^3]$
vr	Rotational movement velocity	$[revs^{-1}]$
vt	Linear movement velocity	$[ms^{-1}]$
w	Heat source density	$[Jm^{-3}s^{-1}]$

α_{conv}	Convection heat coefficient	$[JK^{-1}m^{-1}s^{-1}]$
ar	Rotational movement acceleration	$[revs^{-2}]$
Δz	Mover displacement	$[mm]$
λ	Flux linkage	$[Vs]$
μ	Magnetic permeability	$[Hm^{-1}]$
μ_0	Permeability of vacuum	$[Hm^{-1}]$
μ_m	Mean permeability of a radial flux tube	$[Hm^{-1}]$
μ_r	Relative permeability	$[\ ]$
ρ	Resistivity	$[\Omega m]$
ρ_{copper}	Resistivity of copper (=1.7 10^{-8})	$[\Omega m]$
ρ_{ir}	Mass density of iron	$[kgm^{-3}]$
ρ_{mag}	Mass density of the magnets	$[kgm^{-3}]$
σ	Conductivity	$[\Omega^{-1}m^{-1}]$
σ_{SB}	Stephan-Boltzmann constant	$[JK^{-4}m^{-2}s^{-1}]$
τ_c	Coil pitch	$[mm]$
τ_m	Magnet pitch (= l_{mag})	$[mm]$
τ_p	Pole pitch	$[mm]$
Φ	(Airgap) Flux	$[Vs]$

Subscript	Desription
1	Fundamental
a	Ambient
ax	Axial
c	Coil
g	Airgap
gap	Airgap
ir	Iron ring
m	Mover (or magnet (τ_m))
mag	Magnet
max	Maximal
min	Minimal
mov	Mover
oi	Outer iron
rad	Radial
rod	Inner rod
s	Structure
$stat$	Stator
$turn$	Turn
w	(copper) Wire
win	Winding
$wire$	(copper) Wire

1 Introduction

1.1 Initial task description

The project is created by Assembléon in cooperation with the Technical University of Eindhoven (TU/e). The subgroup Mechatronics of the R&D department of Assembléon, particularly Ir. R van der Burg, responsible for Measurement and Control Engineering, coordinates the project. The Electromechanics and Power Electronics (EPE) group at TU/e was contacted on helping Assembléon in this project. They proposed to turn the project into a practical training for one of their students. The project is supervised by Dr. E.A. Lomonova, MSc. and L. Encica, MSc., both working at the EPE-group.

A description of the project by R. van der Burg is:
"Study to an optimal concept of a PM servo controlled electromechanical actuator that combines multiple (linear and rotary) movements."
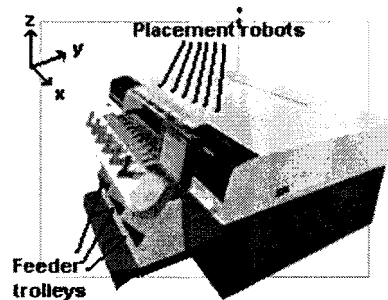
Figure 1.1: The AX-3 robot

To this description the following was added:
"Characteristics of such an actuator are:
Enhanced force control range;
Should fit (preferably) on existing control hardware;
Complex commutation algorithms can be implemented in the motion control FW (FirmWare);
Ideal actuator is small, so that multiple (two or more) actuators can be used on an AX robot."

The AX robot is a product type of Assembléon, used for chip shooting. Two different models exist: the AX-5 and AX-3 with a 5-segment and a 3-segment frame, respectively.

1.2 Project goals

The goal of the project is the development of a new module in the pick-and-place robot, responsible for the picking and placing actions (z-theta module). The new module will be designed for possible usage in an AX machine and will therefore preferably have the same dimensions. The current module contains a rotational motor stacked on a linear voice coil actuator, so the two motors are not on one axis. The expectation is that combining both motors into one single actuator can benefit the system in more than one way. This means that the machines can place more components in the same time, lowering the cost per placement.

The primary goal is to minimize the space occupied by the actuators, creating the possibility to place multiple actuators inside one module. The concept of more actuators results in picking and placing multiple components without making a large transition movement for every single component. This gives a time reduction for transition movements. A study within Assembléon showed that placing two actuators in a one module results in a higher output rate of approximately 30 percent.
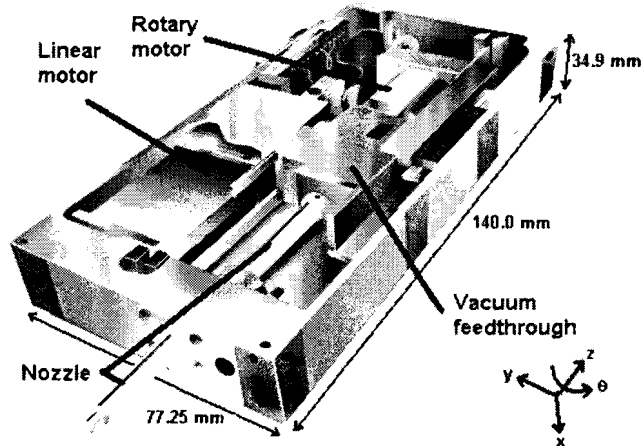
Figure 1.2: The current z-theta module, with the important subparts indicated, and the dimensions of the (closed) module

A possible advantage of the minimisation is weight reduction. Combining both movements can result in less volume and weight for electric coils, permanent magnets and core material. Reducing the weight can result in higher accelerations and lower impact momentum on components and board. Higher accelerations result in faster placement and a lower impact enables the fast placement of delicate components. In addition to a high acceleration, the actuator must also be able to produce a constant force that can hold the nozzle at the right position.

Another advantage can be found within the actuator control. The cascade of actuators, not on one single axis, in the current module has a deviating bandwidth range, constant for low frequencies, but unpredictable for higher frequencies. The new design can have a more predictable and larger bandwidth, enabling faster and more accurate control.

To optimise the bandwidth the use of brushes or another kind of mechanical commutation is unwanted, since brushes can introduce disturbance forces. Also maintenance must be minimised and for machines running up to 24 hours a day, wear is a significant problem.

As a safety measure an automatic retraction needs to be added to the design. This part ensures that on power failure the nozzle is retracted up the z-theta module, so it cannot damage and be damaged by (still moving) PCB's.

1.3 AX robot layout

The AX machine (in figure 1.1 an AX-3 machine is shown) consists of several machine parts. The base of the machine, therefore called machine base, is the frame on which all other parts are fixed. This rigid base is specially designed to withstand and reduce vibrations originating from moving parts in the machine. On the left of figure 1.1 the three feeder trolleys of the AX-3 are shown. Each of these trolleys can carry up to 24 feeders. The trolleys are used to make fast feeder changeover possible, the trolleys are simply docked onto the machine base.

Figure 1.3: Standard placement robot with translation platform, on which the z-theta module is mounted

In the middle of the machine base, above the feeder trolleys, the placement robots are placed. An AX-3 can accommodate up to 6 standard robots (shown in figure 1.3) or 12 compact placement robots. On the placement robot the translation platform provides a large y-stroke and a small x-stroke, dependent whether it is a standard or compact robot. The module and camera (shown in figure 1.4) are mounted on the translation platform. The placement robot is used for planar positioning of the robot, whil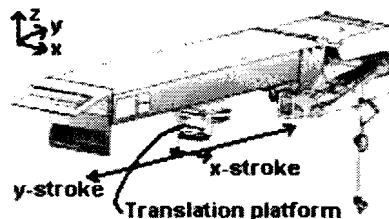e the z-theta module provides vertical stroke and rotation of SMD (Surface Mounted Device) components. The principle of the drive system of the z-theta module is explained in [1].

From the project description and goals can be derived that the 2DOF actuator, that will be developed, should fit at least two times in the dimensions of the current z-theta module. The outer dimensions of the module (in [mm]) can be found in figure 1.2.
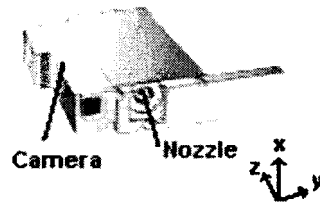

Figure 1.4: Z-theta module with camera module on the left

A restriction is that the module should preferably fit on the existing hardware. The places of contacts of the module (for instance for electric signals and vacuum) should remain the same. This includes both the connections of the module to the translation platform and the connections of the camera to the module. Extra contacts that are needed for the second actuator can be placed freely. The camera is placed on the front of the module and is used for positioning. A deviation of the z-theta module dimensions in y-direction is possible without harming the compatibility. A decrease in this dimension results in a larger active y-stroke for the translation platform. Figure 1.5 shows a top view of the z-theta module, located in the extreme (negative) y position. Changing the y-dimension of the module has no effect on the space that is available for placing the actuator z-axis inside the module. This place is restricted by the length of the camera module and the design of the feeders. The power sources currently available are a one-phase 2.5 [A] and a three-phase 2.5 [A] (per phase) amplifier. The control of the actuator (and amplifiers) is implemented in the control FW.

The module also has to be compatible with the current feeders. The feeders are the devices that transport the parts to the picking place. The compatibility implies a restriction for the place of the axis of the actuators inside the module. It must be not too far to the rear of the module. A schematic top view of different feeders (ITF2, Single Bulk, Twin Tape and Twin Bulk) and their picking places is given in figure 1.5. Dimensions in this figure are in millimetres. The feeders are placed against the machine base (MCS). The machine base is the line where y is defined 0. When there is a 1 [mm] safety gap between the camera module and the platform end, the centre of the camera is located maximally 123 [mm] from the MCS. The centre of the camera is 16 [mm] from the end of camera module. The feeders provide a picking place that is located maximally 80.45 [mm] from the MCS. To enable the picking of parts for all feeder types, the nozzle must be placed maximally (123 − 80.45 − 16 =) 26.55 [mm] from the front of the z-theta module. In the current module, the nozzle is placed 25 [mm] from the front of the module. The centre of the camera is therefore at (16 + 25 =) 41 [mm] from the nozzle. A safety margin of 1.55 [mm] is present to make sure that the picking action is possible. It is possible to enable parallel picking (picking of two nozzles at the same time) by both nozzles for one of the feeder types. But then it is possible that, for other feeders, the second nozzle cannot be used at all. So process-time is not gained by parallel picking, but by eliminating one large translational y-stroke of the translation platform for the picking and placing of two components.
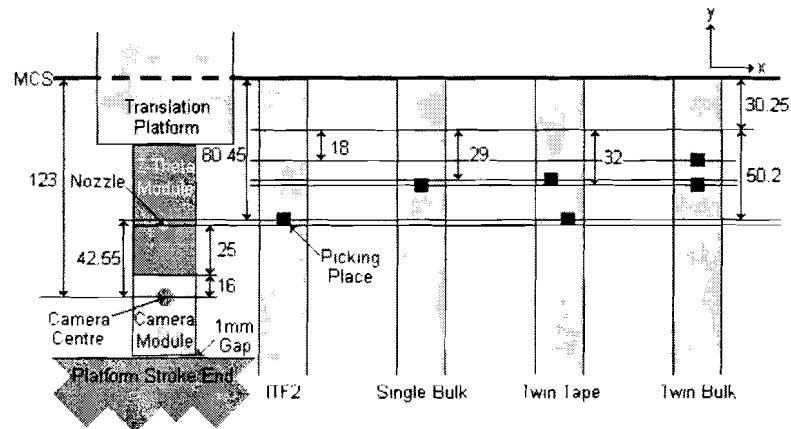
Figure 1.5: *Schematic top view of feeders (ITF2, Single Bulk, Twin Tape and Twin Bulk) and active stroke*

A vacuum circuit is present to create a vacuum between the nozzle and the device, thereby making a picking action possible. A structure is needed to be able to apply the vacuum to the nozzle, which is rotated and translated by the actuator. This vacuum structure occupies room inside the module. A minimisation of the dimensions of the vacuum circuit or a smart placement will maximise the volume available for the actuator. If the device has to be in line with the actuator axis, the maximum length of the actuator is reduced.

The compatibility with the feeders cancels the possibility to place the two actuators that are wanted in one module, next to each other in y-direction. Therefore, the actuators must be placed next to each other in x-direction, parallel to the MCS. There is also the possibility to place the actuators on top of each other, but the nozzle must leave the module through the lower face of the module. This means the axes, on which the nozzle will be placed, must be next to each other in the x-y plane. Therefore the optimal remaining solution is to construct long thin actuators next to each other in x-direction. This limits the x-dimension of each of the actuators to half of the available space. Because the inner x-dimension of the module box is 32 [mm], this results in a maximum x-dimension of the actuator of 16 [mm].

1.4 Module specification

The expected cycle time of a pick-and-place action is 500 [ms]. This is a little shorter than the current duty cycle (600 [ms]), so it is accounting for a rise in running speed. The different actions of one duty cycle are shown in Table 1.1. Placing components is a repetitive process, so after step 9 is completed, the pick-and-place machine continues with step 1. Since in this report the z-theta module is under investigation, the main interest is on the actions carried out by the z-motor and the theta-motor.

Table 1.1: *Actions in a duty cycle*

Step	Action	Responsible system
1	Moving towards the pick position	Robot (x and y transition)
2	Lowering the nozzle	z-motor (of z-theta module)
3	Picking up the device	Vacuum system
4	Rising the nozzle together with the device	z-motor
5	Moving towards the place position	Robot
6	Rotating the device towards the right alignment	theta-motor
7	Lowering the nozzle together with the device	z-motor
8	Placing the component on the board	Vacuum circuit
9	Rising the nozzle	z-motor

There is some overlap in the different steps, to be able to reach a higher placement output rate. For instance the lowering of the nozzle starts when the nozzle gets in the vicinity of the pick position (steps 1 and 2 in Table 1.1).

In one cycle, there is a pick action and a place action (step 3 and step 8 of Table 1.1, respectively). When a device is picked up there is also a rotation to get the right alignment for placing the device. The rotation is carried out during the transition towards the place position (step 5 and 6 of Table 1.1 are parallel steps). The movement features of the current z-theta module are visible in Table 1.2. These figures are the minimum requirements for the new system. Preferably the jerk, acceleration and velocity of both degrees-of-freedom must be improved.

Table 1.2: Features of the current z-theta module

translation				Rotation			
quantity	symbol	value	[unit]	quantity	symbol	value	[unit]
Velocity	vt	0.5	$[ms^{-1}]$	Velocity	vr	10	$[revs^{-1}]$
Acceleration	at	40	$[ms^{-2}]$	Acceleration	ar	300	$[revs^{-2}]$
Jerk	jt	12500	$[ms^{-3}]$	Jerk	jr	50000	$[revs^{-3}]$

1.5 Concepts

In advance of the graduation period an internship of three months was spent on a study for possible implementations in the new z-theta module. During the first period of the internship, the restrictions as described in section 1.2, were determined. After this a study was started to feasible solutions. Papers (conference- and journal-papers) and patents are the base for this study. The search for implementations resulted in three different categories, which were evaluated. In the next sections (1.5.1 to 1.5.3) the concept categories that were found, will be explained and their feasibility will be discussed. The eventual design, of which the actuator under investigation in this reports is a part, will be discussed more extensively in section 1.5.3.

1.5.1 Wrapped planar motor concept

The first concept category is derived from a common planar (x-y) motor. To convert the x-y movement towards a z-theta movement, the magnet plain is wrapped to make it envelope a cylinder. The advantage of this configuration over a normal planar motor is that the airgap can be kept constant by physical bearings instead of magnetic bearings. This simplifies the control significantly, by taking away several degrees of freedom of the planar motor structure. An impression of a wrapped planar motor is shown in figure 1.6. This specific figure is an impression of this type of actuator developed at Philips AT.
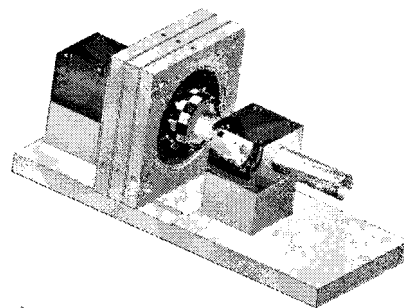

Figure 1.6: Impression of a wrapped planar motor

Both degrees of freedom have individual stator windings. For a three-phase excitation for both axes this would result in 6 phases. The magnet array on the mover is common for both degrees of freedom.

1.5.2 Conical motor concept

The second category originates from the electromechanical machines used in elevators and cranes. Often the induction machine is used in this field for its high power handling capabilities. The conical motor is an induction motor with a conically shaped rotor and stator (see figure 1.7). Because of this conical shape the rotor is retracted into the stator by the stator field. This field is only present when there is a stator current. When there is no stator current and therefore stator field (or a current that is not strong enough) the rotor is subtracted out of the stator. When the rotor is subtracted out of the stator, the elevation system is locked into brake condition. The subtraction is forced by a spring attached between the stator and rotor for instance. When the stator field is restored the rotor is retracted again, enabling rotational movement.
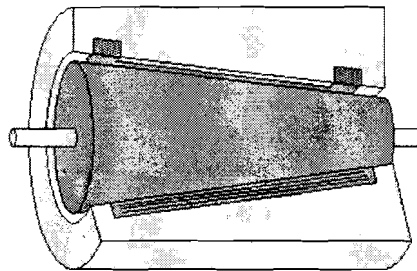
Figure 1.7: Impression of a conical motor

Because the length of the airgap changes with the rotor position, the conical motor concept has a force characteristic that is strongly dependent on the position. Another disadvantage of this design type is that the reluctance force only works in one direction. To enable a subtraction of the rotor out of the stator, an external force is necessary. Some examples that can provide that force are gravity, a spring or another conical motor with opposite conical angle.

1.5.3 Combined actuators concept

The current actuator system in the z-theta module is the base for the final concept: combined actuators concept. In this concept two one-Degree-Of-Freedom (1DOF) actuators are stacked, to get a two-Degree-Of-Freedom (2DOF) system. The performance of the actuator system can be improved by stacking the two separate actuators in a smarter way. The motors are placed on one single fixed axis. The expectation is that this will result in a larger and more predictable control bandwidth than the stacked actuators in the present design.

The combined actuators design consists of two separate machine parts, one for translational or linear movement and one for rotational movement. The total available space is not only limited, but also reduced by the placement of sensors and a vacuum circuit. To compensate for the stroke length either the stator or the mover (translator and rotor for linear and rotational motor, respectively) is enlarged with this stroke length. This is done to keep the force and torque characteristic as independent as possible of the vertical (z-) position. This results in four options for the total actuator design. These options are visualised in figure 1.8.

Solution A of figure 1.8 has long stators for both machine parts, and therefore short movers. This has a minimum total mover mass as major advantage. The mover of the rotary part is not penetrating the linear stator and the linear mover is not penetrating the rotary stator. Area of interest is the space between both (rotary and linear) machine parts because it provides an opportunity to integrate a sensor system into the design.

Solution B has a long linear stator and short rotary stator, so the movers are short and long of both parts, respectively. The total length needed is the same as with solution A. A disadvantage of this solution is that the rotary mover is penetrating the linear stator. The interference caused by this effect is expected to be minimal, contrary to solution C.

Figure 1.8: Four design possibilities with either rotary or linear, mover length or stator length compensating for the stroke length

Solution C has a short linear stator and a long rotary stator. The movers are long and short respectively. Still, the total length needed is 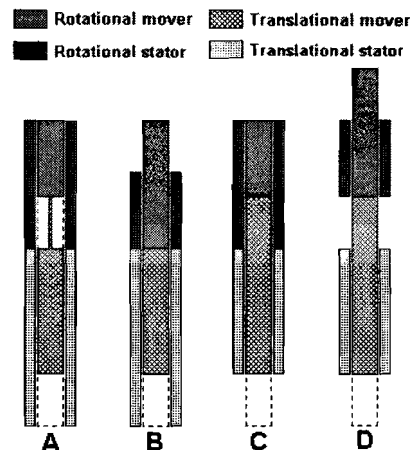the same as with solution A. In this option, the linear mover penetrates the rotary stator, thereby inducting a magnetic field in the rotary windings. This could cause a significant interference.

Solution D has short stators for both parts. Since the movers of both parts are long, this option has the highest mover mass. Besides a high mass, the total length needed for this option is one stroke length more than the other options. This extra length can slightly be reduced since rotation is primarily present in the retracted state. A decrease in active length of the rotary machine, occurring when the mover is extracted, can and will change the motor coefficients. This effect will make the motor coefficients position dependent. The efficient machine length changes and [2] and [3] state that the produced torque is proportional to this length.

A similar opportunity is available in solution B creating the smallest total length for this solution. However, the mover mass of this solution will always be higher than that of solution A. The length of the iron tube on the outside of the structure is equal to the total length needed. It is possible to make it shorter, especially in solutions C and D, but when the linear mover leaves this outer iron tube a significant cogging force is introduced.

The final solution is not present in figure 1.8. This solution is equal to the solution in the current z-theta module. The stator of the rotary motor is stacked on the mover of the linear motor. Therefore, there is no displacement between the rotary motor's stator and rotor. The fact that the linear motor and rotary motor are placed on the same axis is a major advantage of the new actuation system.

Making a choice for these configurations is not only dependent on the minimisation of total structure length and total mass of the mover, but also depends on opportunities in the design to place a sensor device and vacuum circuit in a smart way.

1.6 Structure of the thesis

The study describes the design, manufacturing and testing of an electrical machine. This process includes many moments at which choices and decisions are made. The base for these decisions are the results obtained in the previous work, combined with the availability of the resources that are needed. At the start, the span of the project is wide, investigating multiple solutions of a multi-degree-of-freedom motor. At the start of the graduation the restrictions were narrowed to in first place a brushless linear tubular actuator, which will be combined with a brushless permanent magnet (PM) rotational machine.

In chapter two, the principle of the linear tubular micromotor is introduced. Some initial calculations are made to get an indication of the performance of the motor. The materials that will be used are discussed and a case study is performed to see the possibilities of the linear tubular motor, adapted to the limits of the project. This means that a study is carried out towards the duty cycle of the linear actuator and the mass, the force that needs to be produced and the machine constants are estimated.

The analytical model of the linear tubular actuator is introduced in chapter three. A simple derivation of the model is shown. The Magnetic Equivalent Circuit (MEC) model is determined. After this, the results for the parametric variable MEC model are discussed.

The Finite Element Method (FEM) is used to make a numerical model. The software package that is used to construct the FEM model is Maxwell 9 2D. This means that the model is axisymmetric. The 3D actuator is designed in the z-r plane. In the beginning of chapter four, the construction of the FEM model is discussed. Then the results of the FEM model are shown and finally these results are compared with the MEC model.

Chapter 5 discusses the experimental set-up. The first section of this chapter contains the construction of the set-up and the problems encountered during construction. After the layout of the set-up is discussed the results of measurements, carried out on the set-up are shown. At the end of the chapter, the results of the measurements are compared to both MEC and FEM models.

Chapter 6 describes the process to come to an optimal design of the tubular actuator. Chapter 7 concludes this thesis and formulates conclusions and recommendations.

2 Linear Micromotor Principle

2.1 The slotless linear permanent-magnet tubular actuator

In figure 2.1, an example is shown of a commercially available tubular linear motor. The permanent magnet tubular motor consists of a outer stator containing flux conducting iron and copper windings, and a mover equipped with permanent magnets. Figure 2.2 shows how a rotor of a brushless permanent magnet rotational motor is transferred into the mover of the tubular machine. First the rotor is unrolled to get a linear machine mover. Then the linear mover is rolled again, but in the other direction, to get the tubular mover. Characteristic for the tubular motor is its rotation symmetrical design, which makes it possible to turn the mover inside the stator without consequences for the force production. This makes the design very suited for use in combination with a rotational machine on one fixed axis.
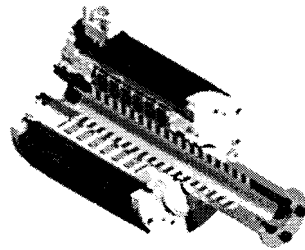
Figure 2.1: Example of a commercially available tubular motor

In the case of the slotless linear permanent magnet tubular motor described in this report, the magnets are not magnetised radially, as figure 2.2 would suggest, but axially. To get a radial field in the airgap, which is needed to create a force in z-direction, the magnets in the mover are oppositely polarised and alternated with ferromagnetic (iron) inter-spacers. In figure 2.3, the polarisation of the magnets is indicated with arrows. It is also possible to replace the iron inter-spacers with radially magnetised magnets. The topology created this way is a Halbach array. The Halbach array mover layout will be discussed briefly in chapter 4. An increase in force output that can be gained by this mover topology is estimated by means of FEM calculations.
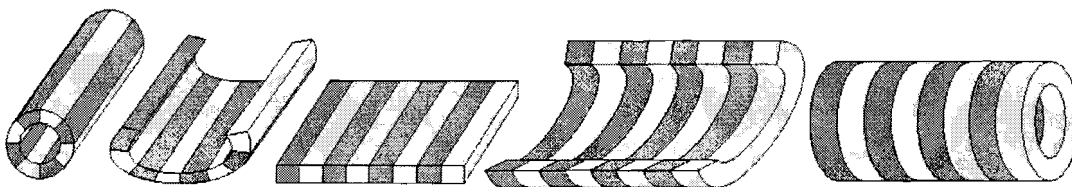
Figure 2.2: From brushless PM machine rotor to brushless tubular PM machine mover

The stator of the tubular actuator under investigation is slotless. This means that the stator windings are placed in the airgap, and not in teeth in the stator iron. The electric circuit is driven by a three-phase source. In figure 2.3, the different phases are indicated by *A*, *B* and *C*. The airgap perceived by the magnets is large because of the airgap windings. This results in a low airgap flux density. This will be explained further in the next section (2.2). The use of airgap windings has two major advantages. The first advantage is that because of the large airgap, the magnets are less susceptible for the demagnetising field of the stator windings. The second advantage is that the magnets do not produce a cogging force, caused by the interaction of the iron inter-spacers with the iron stator teeth.

The tubular permanent magnet motor is constructed from repeating segments (of length τ_p). Because the analytical analysis is not able to cover the end effects that occur at both mover ends, it is sufficient to derive a model for one segment. With the model of one segment, the behaviour of the total actuator can be derived by multiplying the solution with the number of segments in the actuator.

2.2 Initial calculation

The initial analysis is derived from the analysis of a rotational cylindrical machine. The shape of the tubular motor is similar to that of the cylindrical machine only the direction of the windings and the alternation of the magnetic field is perpendicular (in the r-phi-z coordinate system). Therefore the output of the motor is a force and a linear displacement instead of a torque and a rotational displacement. In the design of an electrical machine, so also for a tubular motor, two key variables are: electric loading (Q) and magnetic loading (B). The magnetic loading is the flux density in the airgap. The electric loading is the number of windings per meter of stator length.
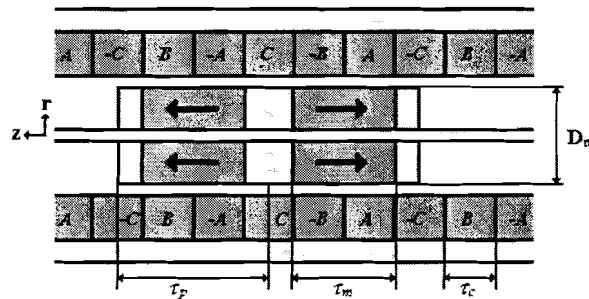
Figure 2.3: Tubular motor layout

For the tubular motor the force (F) on a single current loop, carrying current I, with mover diameter D_m in an airgap flux density B [T] is [11]:

$$F = BI\pi D_m \qquad (2.1)$$

For a winding consisting of N conductors the total force becomes

$$F = BNI\pi D_m \qquad (2.2)$$

Now Q is defined as the ampere-conductors per meter of motor length.

$$Q = \frac{NI}{L} \qquad (2.3)$$

In this equation I is the RMS (Root Mean Square) value of the current. A sinusoidal three-phase current source will be used, so the current will not be equally distributed over the total stator length. The windings carry a sinus waveform current, 120 degrees out of phase with the other phases. In (2.3) L is the length of a tubular motor segment. Later in this chapter the term τ_p (pole pitch) will be used as shown in figure 2.3, instead of L. Substituting (2.3) in (2.2) gives

$$F = \pi BQD_m L \qquad (2.4)$$

From (2.4) the power output (P) of the motor at a speed of v_m [ms^{-1}] is

$$P = Fv = \pi BQD_m Lv_m \qquad (2.5)$$

The active volume of the mover is

$$V_m = \tfrac{\pi}{4} D_m^2 L \qquad (2.6)$$

In this equation L is the same length as the L in (2.3), (2.4) and (2.5). Now the force and power per unit mover volume are:

$$\frac{F}{V_m} = \frac{4BQ}{D_m} \qquad (2.7)$$

$$\frac{P}{V_m} = \frac{4BQv}{D_m}$$

(2.8)

In the application of servo drives, for which the tubular actuator will be used, the force to mass ratio is important. For a cylinder of material of mass density d the mass is given by

$$m_m = dV_m = \tfrac{\pi}{4} dD_{m}^2 L$$

(2.9)

So the force to mass ratio is:

$$\frac{F}{m_m} = \frac{4BQ}{dD_m}$$

(2.10)

The force to mass ratio is a measure for the acceleration the actuator can achieve. The mass is just the mass of the mover. When there is a load attached to the mover, the mass changes. (2.10) shows that the force to mass ratio is inversely proportional to the diameter of the mover (D_m). So creating a thinner motor will result in higher accelerations. However, the total amount of force produced by the machine is direct proportional to the mover diameter (2.4). This is also important because not only the mover is accelerated but also the load of the machine must be accelerated. Besides moving other parts of the z-theta module, the tubular motor must be able to perform a constant holding force that is sufficient to hold the mover in position in spite of other forces that are acting on the mover.

Intuitively the reflection of (2.10) seems right because according to the Lorenz equation the total force is proportional to the length of the wires (equal to πD_m, see (2.1)), and the mass is proportional to the square of the diameter (2.9). But what is the influence of the mover diameter on the electric loading (Q) and magnetic loading (B) of the motor? This question can be answered with two different considerations for the magnetic loading and electric loading individually.

2.3 Materials

In the linear tubular actuator, the three most important materials that are used are: copper, permanent magnetic material, and iron. The copper is used for the electric circuit. The electric circuit consists mainly of windings, which are placed on the stator. The resistive character of the copper causes the windings to heat up as a current is flowing through it. The amount of heat produced in the windings together with the ability of the structure to loose heat to its surroundings determines the temperature in and around the actuator. The permanent magnetic material and the flux conducting iron together form the magnetic circuit of the actuator. In the next paragraphs all three materials (copper, permanent magnets and iron) are treated individually.

2.3.1 Electric loading

The electric loading is defined as the ampere-conductors per meter of stator length (2.3). Of course using thicker or thinner wires can easily modify the number of windings, but this results in a different thermal behaviour of the actuator. Thermal sensitivity is a very important restriction when investigating the electric loading of an electromechanical device. The copper (or resistive) loss is together with the iron loss the most important source of heat in an electrical machine. The copper loss is the dissipated electrical energy, caused by the resistive character of the windings. The amount of heat produced in a copper wire $(P_{loss,copper})$ is a function of it's resistance (R_{wire}) and the current through it (I). More windings will result in a longer copper wire length (l_{wire}) and a smaller wire diameter (D_{wire}).

$$P_{loss,copper} = I^2 R_{wire} = I^2 \frac{\rho_{copper} l_{wire}}{A_{wire}} = I^2 \frac{4\rho_{copper} l_{wire}}{\pi D_{wire}^2}$$

(2.11)

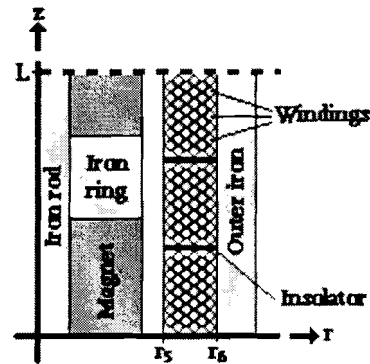ρ_{copper} is the resistivity of copper in $[\Omega m]$.

Figure 2.4 Impression of variables in electric loading

Besides increasing the temperature of the electrical machine, heat will be transferred to the surroundings of the machine. Not only the amount of heat produced but also its ability to lose heat to its surroundings determines the temperature in a machine. The surroundings can possibly contain temperature sensitive equipment. Not only overheating the machine but also overheating parts in its vicinity must be prevented. In this case the possible temperature sensitive parts that are in the direct neighbourhood of the machine are electronics inside the z-theta module and most important the smd-parts that will be picked up by the nozzle.

In the design of this tubular actuator the copper windings are placed on the stator. The windings form a ring of copper in the cross-section of the actuator (see figures 2.3 and 2.4). This ring of copper is separated from the rest of the module by an iron ring. Because the electric loading is specified as the total number of windings per unit of length, it cannot be modified by adding extra length to the stator, but only on the inner side and outer side of the winding ring. Both options have an effect on different parts of the machine. Enlarging the electric loading on the inner side, results in a smaller mover diameter, since the airgap is constant. When the electric loading is increased towards the outside of the actuator, the outer iron will become thinner. In this case, it is presumed that the total diameter of the actuator is kept constant. It is possible to vary the total diameter, but this will result in a different force and mover mass. Making the total diameter larger than 16 [mm], would make it impossible to place two actuators next to each other in the sizes of the current z-theta module. Anyhow, enlarging the electric loading will always result in a larger airgap, since the windings are not placed in slots. Changing the electric loading has a direct effect on the magnetic field density in the airgap, also called magnetic loading. This effect will be described in the next section.

For the first estimation the current density is constant. When the current density is constant, the electric loading is proportional to the copper area indicated in the z-r cross-section of figure 2.4.

$$Q = c_1 \left(r_6 - r_5 \right) \tag{2.12}$$

in which the constant c_1 [Am^{-2}] is defined as:

$$c_1 = I_w n_{wz} n_{wr} \tag{2.13}$$

where I_w is the winding current, n_{wz} is the number of windings per meter of stator length (in z-direction) and n_{wr} is the number of windings in radial (r-) direction. The constant is determined by the thickness of the round copper wire, and the way of winding the wire to a coil (the fill factor). In addition, the use of insulation material between the coils has an influence on this constant. In other words, the constant c_1 corresponds to the current density in the stator windings. The current density can be derived with the winding area, the winding number, the winding current and the fill factor.

2.3.2 Magnetic loading

At the preliminary design stage, the magnetic loading (*B*) is considered to be the airgap flux density produced by the magnets. Distortion of this field, for instance by the armature reaction field, is neglected. The saturation of iron parts and leakage flux are also neglected.
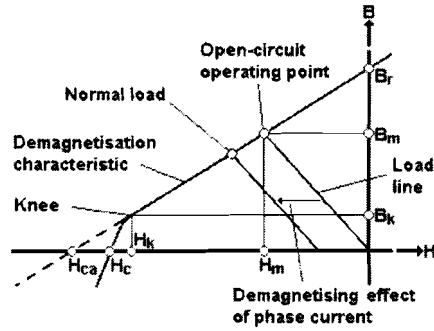
Figure 2.5: Demagnetisation characteristic of hard magnetic material

The B-H curve of a material is also called hysteresis loop. The second quadrant of the hysteresis loop of a hard magnetic material is shown in figure 2.5. This part of the curve is called the demagnetisation characteristic. The hysteresis loop is temperature dependent for all hard magnetic materials. The slope of the demagnetisation characteristic is the recoil permeability. The airgap applies a constant demagnetising effect to the magnet. Therefore, the operation point of the magnet is below its remanent flux density (B_r) at the open circuit operation point. The line from the origin through the open-circuit operating point is called the load line.

The fact that the leakage flux is neglected means in this case that there is no flux going through the inner rod of the mover (see figure 2.5). This implies that the magnet area (A_m) is equal to:

$$A_m = \tfrac{\pi}{4} D_m^2 - A_{rod} = \tfrac{\pi}{4}\left(D_m^2 - D_{rod}^2\right) = \pi\left(r_4^2 - r_2^2\right)$$ (2.14)

The flux density in the airgap becomes:

$$B = \frac{1}{\dfrac{2\mu_{r,mag}l_g}{l_{mag}} + \dfrac{A_g}{A_m}} B_r$$ (2.15)

where:

B_r is the remanent flux density of the magnet
$\mu_{r,mag}$ is the relative permeability of the magnet
l_{mag} is the length of the magnet
l_g is the length of the airgap ($= r_6 - r_4$)
A_g is the mean area of the airgap

Because the area of the airgap is a linear function of the radial position the mean area is taken. In other words, the area is determined in the middle of the airgap. The airgap envelopes not only the actual gap between the mover and stator, but also the volume occupied by the copper windings, since this design uses a slotless stator. The mean area of the airgap is:

$$A_g = \tfrac{1}{2} l_{ir}\pi\left(r_4 + r_6\right)$$ (2.16)

A z-r cross-section with the flux path and magnet and airgap areas is shown in figure 2.6 for one of the segments of the tubular motor. The fact that the magnet path crosses the airgap twice is represented by the factor two in (2.15). The use of airgap windings results in a relatively large gap. The combination of both previous statements leads to an airgap flux density that is relatively low for electrical machines.
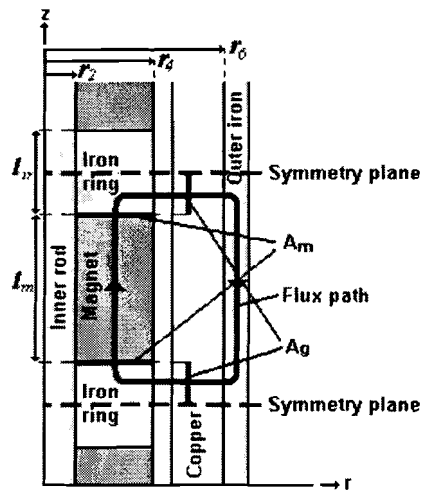
Figure 2.6: z-r cross-section with flux path

When current is flowing through the phase windings, another demagnetising effect is added on top of that of the airgap. The magnetic field due to the current drives the operating point below the open-circuit operation point. When the phase current is removed, the operating point will normally return to the open-circuit operation point, unless it has been forced below the knee of the characteristic. In the case the operation point was driven below the knee, the magnet will recover along a lower recoil line and part of its remanent flux will be lost. This loss is irreversible.

The open-circuit operation point of the magnets can be changed by the parameters described in (2.15). For the tubular motor design these parameters are linked to the mover diameter, the electric loading and the length of the magnets. By changing the mover diameter the area of the magnets (A_m) is changed. Modifying the electric loading is related to modifying the airgap length (l_g), since the airgap consists of the actual gap between mover and stator and the copper windings. When changing the length of the magnets (l_{mag}) the total mover length is changed. It is questionable whether the extra magnet length outweighs the possible use of an extra segment.

2.3.3 Selection of the iron

Iron is present in different parts of the actuator. For the total actuator the restriction is set that there must be no maintenance needed. Also for the type of iron used this is a mayor restriction. The type of iron selected for the various iron parts must be corrosion resistant. Because the iron is used as a flux-conducting medium, the relative permeability must be high. The permeability of iron can be characterised by the B-H curve. In this case, a type of iron is chosen that is commonly available: steel 37. The B-H curve of this steel type is shown in figure 2.7.

As discussed in paragraph 2.3.1, the iron loss is one of the major sources of heat in an electromechanical actuator. The iron losses can be subdivided in hysteresis losses, and eddy current losses.

The hysteresis losses are inherent to the use of iron in an actuator. The losses can be minimised by choosing a type of iron with a small hysteresis loop area. Iron has a hysteresis loop that is similar to the loop for permanent magnet material, shown in figure 2.5. For the hysteresis loop of iron the area inside the hysteresis loop is smaller than the area in the hysteresis loop of permanent-magnet material (see figure 3.2). The area in the hysteresis loop corresponds to the energy that is lost in each loop. The area in the hysteresis loop is also dependent on how far the iron is driven into saturation. How far the iron is driven into saturation depends on the configuration.
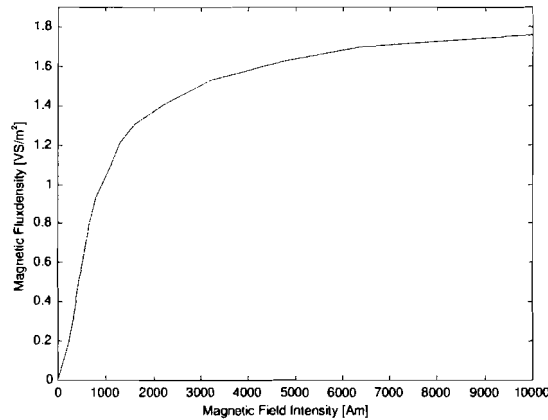
Figure 2.7: B-H curve of steel 37

Eddy currents are cyclic currents in the iron that occur because the iron is trying to resist a magnetic field that is changing in time. Laminating the steel is a way to suppress the eddy currents. The iron is laminated in such a direction that the laminations do not interfere the flux path. The laminations are therefore perpendicular to the flux path. In the slotless permanent magnet tubular linear actuator, the only place where eddy currents can occur is in the outer iron. Because this is a thin piece of iron, it is very difficult to make laminations. Another way to suppress eddy currents over the total outer iron circumference is making a slice in the iron over the whole length of the outer iron.

2.4 Initial selection of sizes

2.4.1 Case study

As described in section 2.2, the 'optimal' design can be found by finding the balance between electric loading, magnetic loading, total diameter and total length. The total diameter of the actuator has a maximum of 16 [mm], to be able to place it twice in parallel in the x-direction in the z-theta module. In paragraph 2.3.1 it is described that the electric loading (Q) is not a function of the length. And because the magnets are axially magnetised, we saw in paragraph 2.3.2 that the magnetic loading (B) is a function of the total length. To get an indication of the balance between magnetic loading and electric loading, as a function of the mover diameter, some parameters have to be fixed.

The fixation of these parameters is not arbitrary, but is based on information found in papers, and on preliminary FEM results. For instance r_6, which is the inner radius of the outer iron, is fixed at 7.0 [mm]. This value is chosen because an outer iron tube with a thickness of 1.0 [mm] does not show any saturation in the preliminary FEM results and the iron tube is mechanically strong enough to support the stator. In [4], it is described that the force ripple is best suppressed at a magnet-pitch (τ_m) to pole-pitch (τ_p) ratio of approximately 0.7 to 0.75 and the force density is near the maximum for these ratios. At this stage this information slightly influences the initial selection of the sizes. The magnet-pitch is equal to the magnet length. The pole-pitch is equal to the magnet length (l_{mag}) plus the iron ring length (l_{ir}). The total length is also chosen with some help from [4]. The magnet length is set at 6 [mm] and the iron ring length at 3 [mm]. Other literature that contributed to the initial selection of sizes is [5], [6], [7] and [8].

In section 2.2 the force produced by the actuator is described as (2.4):

$$F = \pi BQD_m L = 2\pi BQr_4 L \qquad (2.17)$$

From paragraph 2.3.2 comes (2.15):

$$B = \cfrac{1}{\cfrac{2\mu_{r,mag}l_g}{l_m} + \cfrac{A_g}{A_m}} B_r \qquad (2.18)$$

and in paragraph 2.3.1 (2.12):

$$Q = c_1 \left(r_6 - r_5 \right) \qquad (2.19)$$

Since the exact value of the constant c_1 is not known, a normalised force is calculated. c_1 is chosen to make the maximum of the force equal to unity. The force is therefore not an absolute force, but a normalised force. The parameters used in the calculation are shown in table 2.1. A second constant (c_2) is used to scale the acceleration. This will be explained later.

Now the mover radius $(r_4 = \frac{1}{2} D_m)$ makes a sweep from 0.0 to 6.5 $[mm]$. r_4 equal to 0.0 $[mm]$ means that there is no mover. r_4 equal to 6.5 $[mm]$ means that there is no electric loading, in other words: there is copper in the design, since the inner diameter of the outer tube is 7.0 $[mm]$ and the gap between mover and stator is 0.5 $[mm]$. The result is the normalised force as a function of the mover radius shown in figure 2.8.

Table 2.1: Parameters used in the initial calculation

Parameter	Description	Value [unit]
r_2	Outer radius of inner rod	0.0 $[mm]$
r_4	Outer radius of the mover	5.0 $[mm]$
r_5	Inner radius of the stator (= inner radius of electric loading)	$r_4 + 0.5$ $[mm]$
r_6	Inner radius of outer tube (= outer radius of electric loading)	7.0 $[mm]$
r_8	Outer radius of outer tube (= total diameter)	8.0 $[mm]$
l_{mag} $(= \tau_m)$	Length of the magnet	6.0 $[mm]$
l_{ir}	Length of the iron rings	3.0 $[mm]$
L $(= \tau_p)$	Total length $(L = l_{mag} + l_{ir})$	9.0 $[mm]$
$\mu_{r,mag}$	Recoil permeability of the magnet	1.05 $[\,]$
B_r	Remanent flux density of the magnet	1.2 $[T]$
c_1	Constant 1	$4.54 \cdot 10^6$ $[Am^{-2}]$
c_2	Constant 2	$7.50 \cdot 10^4$ $[kgm^{-2}]$

Next, the force is divided by the square of the mover radius, to get the normalised acceleration. The square of the mover radius is proportional to the mover mass. Since not the absolute force is calculated, but a normalised force, the amplitude of the acceleration cannot be estimated. The constant c_2 is used to scale the maximal acceleration to unity. This constant consists of the mass density of the materials used, the length of the mover and a factor π, so its unit is $[kgm^{-2}]$. The normalised
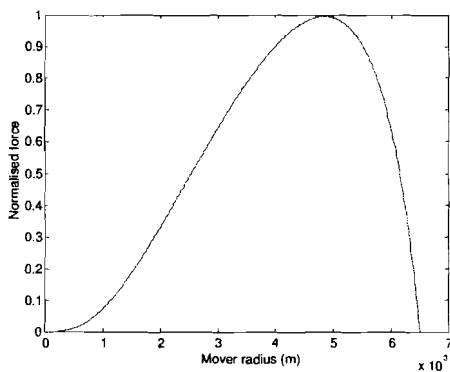

Figure 2.8: Normalised force as a function of the mover radius
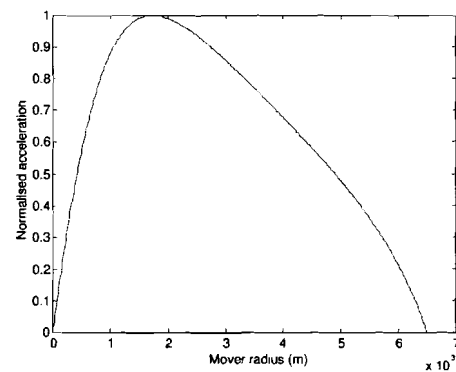

Figure 2.9: Normalised acceleration as a function of the mover radius

acceleration is:

$$a_{norm} = \frac{F_{norm}}{c_2 r_4^2}$$ (2.20)

The normalised acceleration as a function of the mover radius is shown in figure 2.9.

2.4.2 Estimation of mass and inertia

When the duty cycle is known, the mass and inertia of the mover must be known in order to be able to derive the force (and torque) that are needed to reach the desired acceleration and speed. In Table 2.2 the expected mass and inertia of the different mover parts are given. This expectation is based on the rules of thumb for electromechanical machines described in section 2.2. It is only an indication of the eventual mass and inertia. The nozzle for instance is attached to the mover. The nozzle and nozzle holder add extra mass and inertia to the moving parts of the machine. An estimation of this mass and inertia of the nozzle and the nozzle holder is also present in Table 2.2. These figures do not represent a currently available nozzle, but a new nozzle will be designed for the new actuator. Currently, a common nozzle is about 16.4 [mm] long and has a radius of 6.6 [mm]. This results in a mass of 16.6 [gram] for a solid steel nozzle and holder. The expectation is that the new nozzle can have about half the mass of the current nozzle. For instance, a length of 12 [mm] and a radius of 5.5 [mm] will result in a mass of 8.44 [gram] and an inertia of 12.70 10^{-8} [kgm^2].

Table 2.2: Expected mass and inertia of the mover

Part	Sub-part	Rho [kg/m^3]	Length [m]	Radius (out – in) [m]	Mass [kg]	Inertia [kgm^2]
Translation	magnets	7350	30 10^{-3}	4.5 10^{-3} (- 0)	14.0 10^{-3}	14.18 10^{-8}
	steel	7400	10 10^{-3}	4.5 10^{-3} (- 0)	4.7 10^{-3}	4.76 10^{-8}
Rotation	magnets	7350	45 10^{-3}	5.5 10^{-3} - 4.0 10^{-3}	19.6 10^{-3}	13.97 10^{-8}
	steel	7400	45 10^{-3}	7.0 10^{-3} - 5.5 10^{-3}	13.4 10^{-3}	12.56 10^{-8}
Intersp. rod	steel	7400	30 10^{-3}	4.5 10^{-3} (- 0)	14.1 10^{-3}	14.27 10^{-8}
Nozzle	(total)	7400	12 10^{-3}	5.5 10^{-3} (- 0)	8.4 10^{-3}	12.70 10^{-8}
total					74.2 10^{-3}	72.44 10^{-8}

The total mass of the other parts without the linear motor (rotation, interspacing rod and nozzle) is: 55.5 10^{-3} [kg]

2.4.3 Linear motion analysis

In table 1.1 the duty cycle of the pick-and-place machine is described. Movements of the actuator in z-direction are present in step 2, 4, 7 and 9 of the duty cycle. A profile of a translation containing acceleration (a), velocity (v) and z-position (z) is shown in figure 2.10. Table 2.3 shows the timing of the different intervals in figure 2.10, when the specifications of the current actuation system are used.

Table 2.3: Duty cycle timing analysis

Interval	Description	*1	Time [ms] *2	Total time [ms] *3
(t_0,t_1), (t_2,t_3), etc.	Time of maximum jerk	16	3.2	51.2
(t_1,t_2), (t_5,t_6)	Time of maximum acceleration	8	9.3	74.4
(t_3,t_4)	Time of maximum velocity	4	44.3	177.2
Total	Total time of one duty cycle			302.8

*1   The number of times this interval is in a total duty cycle. Note that one cycle contains four transitions as described in figure 2.10.
*2   The time that is needed for one individual action
*3   The time this action occupies in one total duty cycle (= *1 x *2)

Since one pick-and-place action takes four transitions, the time needed for one transition is 75.7 [ms]. The total linear motion time per duty cycle (302.8 [ms]) occupies a rather great portion of the total duty cycle time. When this total duty cycle time becomes 500 [ms] (currently it is 600 [ms]), the linear
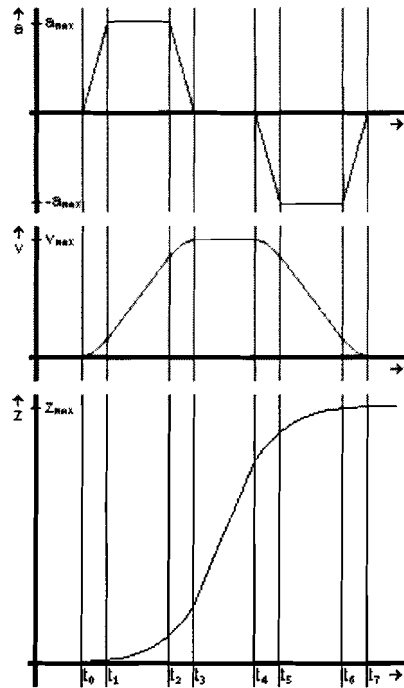
Figure 2.10: *Profile of acceleration (a), velocity (v) and z-position (z) in one transition.*

motion would occupy 60.6 % of the total duty cycle. As discussed in chapter 1, the actions in table 1.1 take place simultaneously in some cases, but there is a limit to this. The performance of the new linear motor will need to be better than that of the current linear motor.

The peak force is needed for maximum acceleration and deceleration. As can be seen in table 2.3, during one total duty cycle the maximum acceleration or deceleration occurs 8 times and the maximum jerk 16 times. This means that the peak force, and therefore peak current, is needed during 125.6 [ms]. Again seen on a total duty cycle of 500 [ms] the percentage of time during which the maximal current is applied, is 25.1 %. This data is important when analysing the thermal behaviour of the linear motor.

Between the translational strokes, the mover needs to stay at its position. Even when there is no electric supply, forces are acting on the mover. The most obvious force that is present is gravitation. Another force that can be present is a reluctance force, which pulls the mover to the middle of the stator of the linear motor. The gravitation force is constant for all z-positions, but the reluctance force is position dependent. The magnitude of this reluctance force is not clear at this stage yet, and needs to be analysed later. This analysis will be carried out with the Finite Element Method (FEM) and can therefore be found in section 4.4.

The static force, which is the resultant of gravity and reluctance force, is constantly present. To keep the velocity of the mover constant this static force has to be compensated, together with the friction force. It also causes a position dependent acceleration and deceleration, because the static force is expected to be position dependent. To get an acceleration (or deceleration) of 40 $[ms^{-2}]$ the resultant of all forces that act on the mover has to be:

$$F_{res} = m_m \cdot a \qquad\qquad (2.21)$$

The mover mass (m_m) is estimated at 75.2 [gram] in table 2.2, so F_{res} is 3.0 [N]. Only accounting for the gravitation force, which has a magnitude of 0.75 [N], the force generated by the translating actuator is either 3.75 [N] for accelerating in the opposite direction of the gravity force or 2.25 [N] for accelerating

in the direction of the resultant force. This example indicates that the gravitation force and other disturbance forces can drastically change the maximum force that is demanded from the linear motor.

2.4.4 Machine constants

The electric circuit is designed to fit to a three-phase current source that is present at Assembléon. The specifications of this source are shown in appendix C.2. To match the linear motor to its controller the force constant k_F and back-EMF constant k_E are derived with [10]. k_E is defined as:

$$k_E = \frac{\hat{e}_{ll}}{v_m} \tag{2.22}$$

with units $[Vsm^{-1}]$. v_m is the mechanical speed of the mover and $\hat{e}_{ll}$ is the peak line-to-line induced voltage (or peak line-to-line back-emf). k_F is defined as:

$$k_F = \frac{F}{\hat{i}} \tag{2.23}$$

with units $[NA^{-1}]$. F is the force produced in the motor [N] and $\hat{i}$ is the peak line current [A], which is equal to the peak phase current in y-connection. For the ideal three-phase sine-wave excitation motor: the electromechanical power conversion (P_{elec}) is:

$$P_{elec} = 3E_{rms}I_{rms} = \frac{\sqrt{3}}{2}\sqrt{6}E_{rms}\sqrt{2}I_{rms} = \frac{k_F}{k_E}\hat{e}_{ll}\hat{i} = Fv_m \tag{2.24}$$

where E_{rms} and I_{rms} are the RMS value of the phase voltage and phase current, respectively. Now, the ratio between k_E and k_F is:

$$k_F = \frac{\sqrt{3}}{2}k_E \tag{2.25}$$

The back EMF (e) is derived from the flux-linkage waveform (λ) according to Faraday's Law:

$$e(\Delta z) = \frac{d\lambda}{dt} = v_m \frac{d\lambda(\Delta z)}{d(\Delta z)} \tag{2.26}$$

The notation $e(\Delta z)$ means the EMF plotted as a function of mover displacement Δz, rather than plotting it as a time waveform $e(t)$. The wave-shape is unaffected because $\Delta z = v_m\Delta t$ and v_m is $d(\Delta z)/dt$. In other words: the back EMF is a function of the mover displacement (Δz) and a linear function of the mechanical speed (v_m).

In the ideal sine-wave motor only the fundamental space-harmonic component needs to be considered. The flux density in the airgap (B) can be described as a Fourier series:

$$f(x) = \tfrac{1}{2}a_0 + \sum_{n=1}^{\infty} a_n \cos\left(\frac{n\pi x}{L}\right) + \sum_{n=1}^{\infty} b_n \sin\left(\frac{n\pi x}{L}\right) \tag{2.27}$$

where:

$$a_0 = \frac{1}{L}\int_{-L}^{L} f(x)\,dx$$

$$a_n = \frac{1}{L}\int_{-L}^{L} f(x)\cos\left(\frac{n\pi x}{L}\right)dx$$

$$b_n = \frac{1}{L}\int_{-L}^{L} f(x)\sin\left(\frac{n\pi x}{L}\right)dx$$

Instead of the interval [-L, L] every interval with length 2L can be used, so a convenient choice is made. This choice results in the fact that either all the coefficients a_n, or all coefficients b_n are zero. Because for a sine-wave motor the first harmonic is producing the wanted force, only a_1 and b_1 have to be

derived. All higher harmonic components produce disturbances. By choosing the integration interval as in figure 2.11, L is equal to $l_{ir} + l_{mag}$, and the coefficients b_n are all zero.
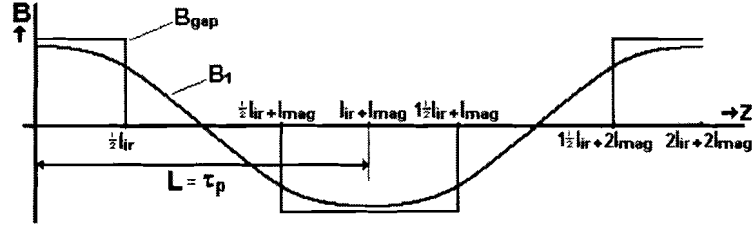
Figure 2.11: Ideal magnetic flux density distribution in the airgap (B_{gap}) and fundamental component (B_1)

The amplitude of the fundamental of B (B_1) is equal to a_1 and can be calculated by:

$$B_1 = \frac{1}{l_{ir} + l_{mag}} \int_0^{2(l_{ir}+l_{mag})} B(z) \cos\left(\frac{\pi z}{l_{ir} + l_{mag}}\right) dz \qquad (2.28)$$

$$= \frac{4B_{g0}}{\pi} \sin\left(\frac{\pi l_{ir}}{2(l_{ir} + l_{mag})}\right)$$

where B_{g0} is the amplitude of the magnetic field density in the airgap (B). In the next equations $l_{ir} + l_{mag}$ is replaced with τ_p (pole pitch) and l_{mag} is replaced with τ_m (magnet pitch). The fundamental of the flux (Φ_1) can be derived from B_1:

$$\Phi_1 = B_1 A_p = B_1 2\pi r_c \left(\tau_p - \tau_m\right) \qquad (2.29)$$

where A_p is the airgap area per pole, and r_c is, for a slotless configuration, the mean radius of the coils. The fundamental of the lux linkage is therefore:

$$\lambda_1 = N_t \Phi_1 = n_{tc} B_1 2\pi r_c \left(\tau_p - \tau_m\right) \qquad (2.30)$$

where n_{tc} is the number of turns per coil. The amplitude of the induced voltage per coil is:

$$\hat{e}_c = v_m \frac{1}{\tau_p} \lambda_1 = v_m \frac{1}{\tau_p} n_{tc} \Phi_1 \qquad (2.31)$$

The total EMF per phase (e_{ph}) is the EMF per coil multiplied by the number of coils in series in which the EMF is induced (n_{acw}), The amplitude of this EMF is:

$$\hat{e}_{ph} = n_{acw} \hat{e}_c = n_{acw} v_m \frac{1}{\tau_p} n_{tc} \Phi_1 \qquad (2.32)$$

In a balanced sinusoidal operation in a y-connection, the peak line voltage is defined as:

$$\hat{e}_{ll} = \sqrt{3} \hat{e}_{ph} \qquad (2.33)$$

With (2.22), (2.29), (2.32) and (2.33), k_E can be written as:

$$k_E = \sqrt{3} n_{acw} n_{tc} \frac{1}{\tau_p} B_1 2\pi r_c \left(\tau_p - \tau_m\right) \qquad (2.33)$$

and k_F can, according to (2.24), be specified as:

$$k_F = \tfrac{3}{2} n_{acw} n_{tc} \frac{1}{\tau_p} B_1 2\pi r_c \left(\tau_p - \tau_m\right) \qquad (2.34)$$

3 Analytical Analysis

One of the possibilities in modelling an electromechanical actuator is by means of a Magnetic Equivalent Circuit (MEC) model. The main advantage of MEC, compared to the also commonly used Finite Element Method (FEM) analysis, is that the model is relatively simple. Therefore, the calculation time needed to solve the model is short. The main disadvantage is that the direction of the field must be known throughout the structure. Therefore, knowledge of electromechanics must be present, before this method can be used. Besides that, the accuracy of the model is not as good as FEM, but better than the initial analysis derived in chapter 2. For these reasons MEC is often used in the design process as a first indication. A MEC model allows deriving how parametric changes in the design influence the motor performance. Performance in this case is a subjective term, since every design has a different background and different demands. In this case, the demands are determined in chapter 2. When the MEC model has given an indication of the optimal layout, the design process is continued in a more focussed and accurate way by means of FEM. Because of the low complexity of the model, a MEC model can easily be implemented in any kind of programming language, for instance C (or C++) or in this case MATLAB.
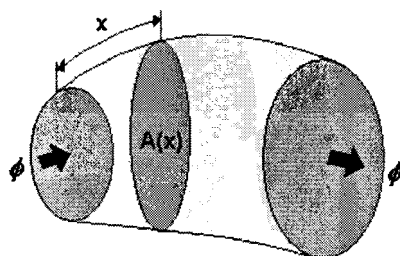
Figure 3.1: flux tube

3.1 Deriving the model

A MEC model of an electromechanical structure consists of a limited number of elements. Each element represents a flux path or flux tube. A flux tube is defined as a geometrical figure, in which all flux lines are perpendicular to their bases and no flux lines cut their sides [9]. Perpendicular to flux lines are lines of equal magnetic scalar potential. Therefore, the bases of a flux tube are equipotential planes. The potential difference between the bases is equal to the magneto-motive force (MMF or $\mathcal{F}$) drop in [A]. Generally, the ratio of the potential difference between the bases of the flux tube and the flux through it is a function of the geometry of the tube and the characteristics of the medium. Mathematically, this ratio is described by:

$$R = \int_0^l \frac{dx}{c(x)A(x)} \qquad (3.1)$$

where l is the total flux tube length, $A(x)$ is the cross-section area of the flux tube and $c(x)$ is a function of material properties. The quantity R is defined as reluctance in magnetic fields and is analogous to resistance in electric fields. For magnetic fields the quantity $c(x)$ is equal to the material permeability ($\mu(x)$) and for electric fields $c(x)$ is equal to the conductivity ($\sigma(x)$). Mathematically, reluctance and resistance can be described as, respectively:

$$\mathcal{R}_m = \int_0^l \frac{dx}{\mu(x)A(x)} \qquad (3.2)$$

$$R_{el} = \int_0^l \frac{dx}{\sigma(x)A(x)} \tag{3.3}$$

The elementary relationships between flux density and magnetic field strength for magnetic field and current density and the electric field strength for electric fields are given by the Maxwell equations:

$$B = \mu H \tag{3.4}$$

$$J = \sigma E \tag{3.5}$$

A table of magnetic and electric analogies is shown in appendix A.3.
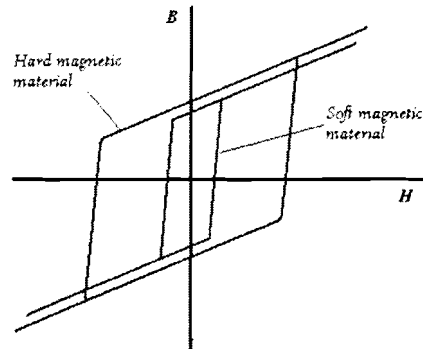
Figure 3.2: Hysteresis loop for hard and soft magnetic materials

According to [9], there is one difference in the analogy between electric and magnetic fields. To maintain a certain energy level in a magnetic field, no external support is needed. In an electric field the energy is irreversibly converted into heat, therefore a source is needed to maintain a constant energy level. When all quantities in a magnetic field are constant, the energy stored in the field is constant, while under the same conditions the energy lost in an electric field increases proportional to the time.

The MEC model starts with a simple circuit model, and then increases in complexity. When the non-linearity of the materials is added, the model is not completely analytic anymore. Field solutions are in that case found with iterative processing.

The equivalent circuit is described as a function of the actuator's parameters (sizes, materials etc.). Goal of the model is to find an expression for the force (or torque) produced by the actuator. The model starts with finding the electric equivalent of the permanent magnet. To be able to derive this equivalent some understanding of permanent magnetic material is needed.
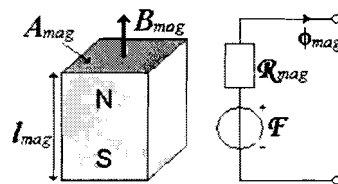
Figure 3.3: The permanent magnet and its equivalent model

As described in paragraph 2.3.2 and shown in figure 2.4, permanent magnets are characterised by their B-H hysteresis curve. Based on the area inside the hysteresis loop we distinguish hard magnetic material from soft magnetic material. For hard magnetic material, this area is large compared to soft magnetic material, as shown in figure 3.2. The area inside the loop indicates the energy loss per unit volume per cycle. The hysteresis loop is not only a function of the material, but also a function of the applied fields. With magnetic flux analogue to electric current, the electric equivalent of a permanent

magnet (PM) is an electric source. This can either be a voltage of a current source dependent on using a Thevenin or a Norton equivalent. As shown in figure 3.3 the magnet consists of a mmf source ($\mathcal{F}$) and an internal resistance ($\mathcal{R}_m$), where:

$$\mathcal{F} = H_c l_{mag} \tag{3.6}$$

with H_c the magnetic coercivity which is a property of the permanent magnet material, and:

$$\mathcal{R}_{mag} = \frac{l_{mag}}{\mu_0 \mu_{r,mag} A_{mag}} \tag{3.7}$$

After describing the permanent magnets, the magnetic reluctances in the structure are determined. In the tubular actuator structure of this report, there are two different categories of flux tubes: flux tubes with a flux path in axial direction and flux tube with a flux path in radial direction. For the flux tubes with a flux path in axial direction the reluctance can be calculated analogue to (3.7), with:

$$\mathcal{R}_{ax} = \frac{l_{ax}}{\mu_0 \mu_r A_{ax}} \tag{3.8}$$

Where: l_{ax} is the length of the flux tube from base to base
$\qquad A_{ax}$ is the area of the flux tube
$\qquad \mu_0$ is the permeability of vacuum
$\qquad \mu_r$ is the relative permeability of the medium
The area of the flux tube is constant and equal to the area of the bases.

For the flux tubes with a radial flux, (3.2) becomes:

$$\mathcal{R}_{rad} = \int_{r=r_i}^{r_j} \frac{dr}{\mu(r)\varphi r l} \tag{3.9}$$

In figure 3.3, a flux tube with radial flux is shown. For a flux tube that envelops a full circle, φ is equal to 2π. In (3.9), the permeability of the medium is a function of the radial position. Especially for material with a non-linear B-H characteristic, this gives some problems. To keep the model simple, only one value of permeability is calculated and further used for the total flux tube. The location of the point where the permeability is calculated is at the mean radius of the flux tube ($r = \frac{1}{2}r_i + \frac{1}{2}r_j$). This results in the reluctance:

$$\mathcal{R}_{rad} = \frac{1}{2\pi\mu_m l} \ln\left(\frac{r_j}{r_i}\right) \tag{3.10}$$

where μ_m is the permeability of vacuum times the relative permeability at the mean radius of the flux tube:

$$\mu_m = \mu_0 \mu_{rel}\big|_{r=\frac{r_i+r_j}{2}} \tag{3.11}$$
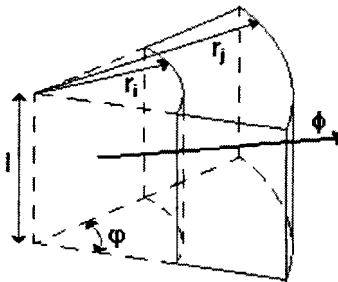
Figure 3.3: Reluctance calculation for a flux tube with radial flux

3.2 The Magnetic Equivalent Circuit model

Now a MEC scheme can be drawn in which all the flux tubes in the tubular motor have a place. In figure 3.4 this scheme is shown, for one segment of the total machine. The corresponding mechanical dimensions are shown in figure 3.5. To get the model of the total machine this segment is repeated several times, dependent on the number of segments on the mover. Each segment represents a pole on the mover and has the length $l_{mag} + l_{ir}$ ($= L$). The MEC calculations are carried out over only one segment and repeated over the number of segments in the mover of the machine. Fringing of the flux lines from the iron ring upper and lower surface, that occurs at both mover ends, is therefore not in the model. A list of the reluctances and how they are calculated from the fixed and variable parameters is available in appendix A.2.
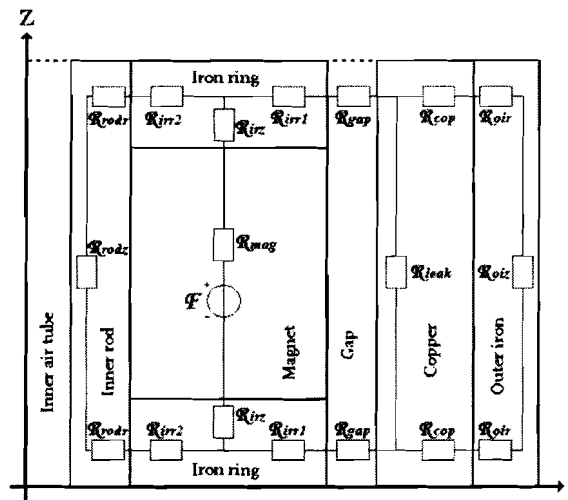
Figure 3.4: MEC model of a segment of the linear machine

The matlab m-files describing the MEC model are in appendix A.4. In this model, there are several variables. Some variables represent geometrical parameters of the structure, other parameters represent material properties. The variables related to the geometry that can be varied and how they are related to the geometry, are shown in figure 3.5. In some occasions, the variable r_5 is not used. Instead of this variable, the variable airgap is used. The reason for this change in variable is that for a constant airgap, the variable airgap is constant, but the parameter r_5 changes together with the
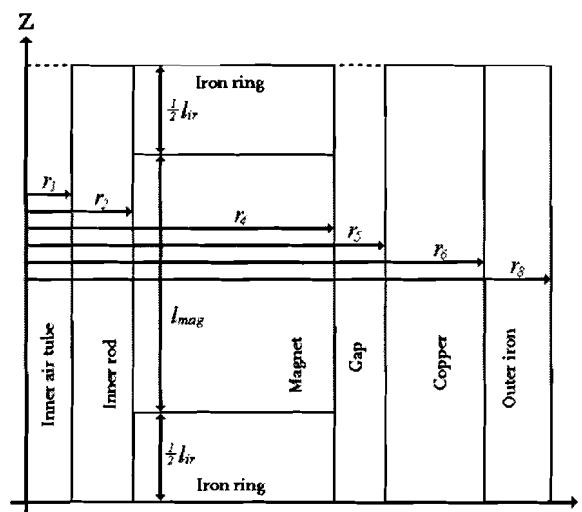
Figure 3.5: Geometrical parameters in the MEC model

parameter r_4. By using the parameter airgap, the evaluation of the results of the parametric calculations can be simplified.
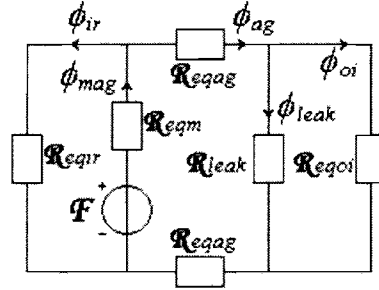
Figure 3.6: Simplified MEC circuit

The circuit of figure 3.4 is simplified into the circuit shown in figure 3.6. In this figure, the fluxes over the different paths in the actuator (ϕ_{mag}, ϕ_{ir}, ϕ_{ag}, ϕ_{leak} and ϕ_{oi}) are indicated. In figure 3.6:

$$\mathcal{R}_{eqir} = \mathcal{R}_{rodz} + 2\mathcal{R}_{rodr} + 2\mathcal{R}_{irr2} \tag{3.12}$$

$$\mathcal{R}_{eqm} = \mathcal{R}_{mag} + 2\mathcal{R}_{irz} \tag{3.13}$$

$$\mathcal{R}_{eqag} = \mathcal{R}_{irr1} + \mathcal{R}_{gap} \tag{3.14}$$

$$\mathcal{R}_{eqoi} = \mathcal{R}_{oiz} + 2\mathcal{R}_{oir} + 2\mathcal{R}_{cop} \tag{3.15}$$

With Kirchhoff's laws the circuit can now be described as a system of linear equations:

$$[A][\Phi] = [f] \tag{3.16}$$

where $[A]$ is the coefficient matrix given by:

$$[A] = \begin{bmatrix} 1 & -1 & -1 & 0 & 0 \\ 0 & 0 & 1 & -1 & -1 \\ \mathcal{R}_{eqm} & \mathcal{R}_{eqir} & 0 & 0 & 0 \\ \mathcal{R}_{eqm} & 0 & 2\mathcal{R}_{eqag} & \mathcal{R}_{leak} & 0 \\ \mathcal{R}_{eqm} & 0 & 2\mathcal{R}_{eqag} & 0 & \mathcal{R}_{eqoi} \end{bmatrix} \tag{3.17}$$

The fluxes in the different paths in the actuator are in the column matrix:

$$[\Phi] = \begin{bmatrix} \phi_{mag} & \phi_{ir} & \phi_{ag} & \phi_{leak} & \phi_{oi} \end{bmatrix}^T \tag{3.18}$$

and the column vector [f] is:

$$[f] = \begin{bmatrix} 0 & 0 & \mathcal{F} & \mathcal{F} & \mathcal{F} \end{bmatrix}^T \tag{3.19}$$

3.3 MEC results

In the next paragraphs, the results of the MEC model are treated. In each paragraph, one or two (geometrical) variables are varied while the others remain constant. The constants c_1 and c_2, used in paragraph 2.4.1, are not used in this derivation. Instead of c_1, the current density (J) (with a value of 6 10^6 [Am^{-2}]) is used. The mass of the mover (m_m) replaces c_2. The mass of the mover is not the mass estimated in paragraph 2.4.2, but it is calculated as a function of the geometrical variables. This mass incorporates only the mass of the mover of the linear tubular actuator. In some cases a load mass is added to the mover mass, but only where this is explicitly indicated in the text. With these new variables, the absolute force can be calculated, contrary to the normalised force calculated in paragraph 2.4.1.

Table 3.1: Variables used in the MEC calculations, and their constant value

Parameter	Description	Value [unit]
r_2	Outer radius of inner rod	0.0 [mm]
r_4	Outer radius of the mover	5.0 [mm]
r_5	Inner radius of the stator (= inner radius of electric loading)	$r_4 + 0.5$ [mm]
r_6	Inner radius of outer tube (= outer radius of electric loading)	7.0 [mm]
r_8	Outer radius of outer tube (= total diameter)	8.0 [mm]
$\tau_m (= l_{mag})$	Magnet pitch (= length of the magnet)	6.0 [mm]
l_{ir}	Length of the iron rings (= τ_p - τ_m)	3.0 [mm]
$\tau_p (=L)$	Pole pitch (= total length (= $l_{mag} + l_{ir}$))	9.0 [mm]
$\mu_{r.mag}$	Recoil permeability of the magnet	1.05 [ ]
B_r	Remanent flux density of the magnet	1.2 [T]
J	Current density	$6.0 \ 10^6$ [Am^{-2}]
m_m	Mover mass (calculated as a function of r_2, r_5, r_6, r_8, l_{mag} and l_{ir})	- [kg]
Δz	Displacement in z-direction	0 [mm]

The mover mass is calculated by:

$$m_m = \pi r_2^2 \tau_p \rho_{ir} + \pi \left(r_4^2 - r_2^2 \right) \left(\tau_m \rho_{mag} + \left(\tau_p - \tau_m \right) \rho_{ir} \right) \tag{3.12}$$

where ρ_{ir} is the mass density of iron (7400 [kgm^{-3}]) and ρ_m is the mass density of the magnets (7350 [kgm^{-3}]). The force is calculated with the Lorentz volume integral:

$$F = \iiint J \times B dV \tag{3.13}$$
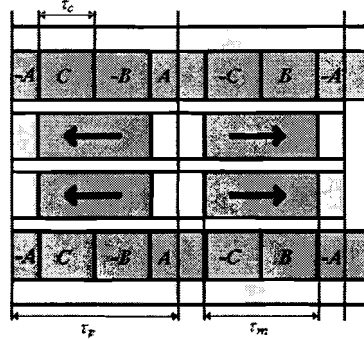
Figure 3.7: Mover position for force calculation

This is possible because FEM models showed that the field caused by the stator windings is approximately a factor 500 times smaller than the field of the permanent magnets (section 4.4). The field of the magnets is hardly influenced by the winding currents. The force is only calculated at one distinguished point of mover displacement (see figure 3.18). This is the configuration indicated in figure 3.7. At the end of this section, the force will be estimated as a function of the mover displacement. Because the flux lines cross the airgap perpendicularly in the model, (3.13) can be rewritten as:

$$F = 2J\phi_{oi} \left(r_6 - r_5 \right) \tag{3.14}$$

This is only true when the length of the iron rings (l_{ir}) is smaller than the coil pitch (τ_c). ϕ_{oi} is that part of the flux that crosses the airgap to the outer iron and is calculated by the MEC model. The coil pitch is:

$$\tau_c = \tfrac{1}{3} \left(\tau_p \right) \tag{3.15}$$

When l_{ir} is larger than τ_c (3.14) becomes:

$$F = 2J\phi_1\left(r_6 - r_5\right)\left(\frac{\tau_{mag}}{6l_{ir}} + \frac{2}{3}\right)$$

(3.16)

The reason for a different force formula is that the current density in the neighbouring coils of the coils A and –A is not equal to J. There is a phase difference of 120° between the phases A, B and C. This means the magnitude of phase B and C is $J\ cos(120) = -0.5\ J$ Because the neighbouring coils of phase A are the coils –B and –C the magnitude of the current density is $0.5\ J$.

3.3.1 Variable mover radius

For the initial estimation of sizes in section 2.4, the normalised force and acceleration produced by the tubular motor is analysed as a function of the mover radius. An equivalent analysis is carried out with the MEC model. As indicated before, not a normalised, but an absolute force is calculated with the MEC model. The geometrical parameters used in the preliminary derivation of section 2.4 are also used in the MEC analysis. These parameters are shown in table 3.1. The variable in this test is the mover radius (r_4). The airgap is constant (0.5 [mm]), so r_5 changes together with r_4. The results of the calculation for the (absolute) force and acceleration are shown in figure 3.8 and 3.9 respectively. These figures can be compared to the normalised force and normalised acceleration shown in figure 2.8 and 2.9, respectively.
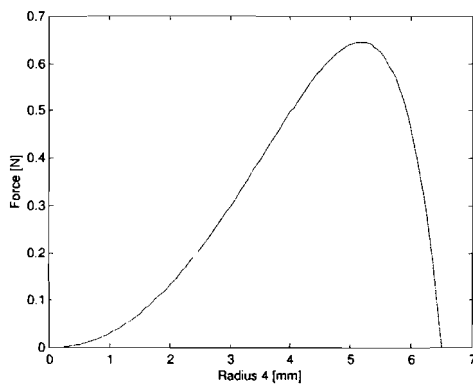
Figure 3.8: Force per segment as function of the mover radius
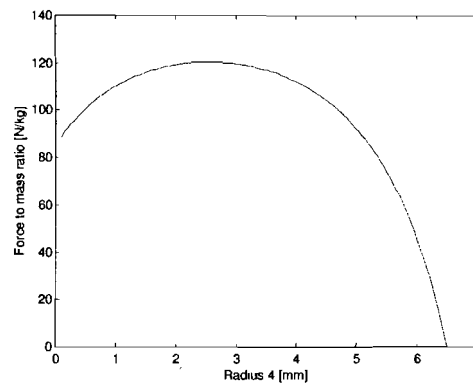
Figure 3.9: Acceleration (per segment) as function of the mover radius

The amount of force shown in the plots is the force produced by one tubular actuator segment. To get the total force produced by the actuator the value in the figure has to be multiplied by the number of segments. Since the mass also has to be multiplied with the number of segments, the acceleration of the actuator needs no scaling factor.

The acceleration shown in figure 3.9 is the acceleration that is achieved when there is no load attached to the linear tubular actuator. When the actuator is implemented in the z-theta module the load of the motor will consist of a rotary motor, a vacuum system and other parts. An estimation of the mass of the moving parts in the z-theta module is presented in table 2.2. Not all moving parts in the system are in this table. For instance, parts of the vacuum system that are moving and parts of the bearing system are not in the table. When a constant mass is added to the varying mass of the tubular motor mover, the acceleration characteristic changes. In figure 3.10, the calculated force is multiplied by a factor 4 (for 4 segments) and then divided by 4 times the calculated mass. To the calculated mass of 4 segments, a mass of 25, 50, 75 and 100 [gram] is added, respectively. Therefore, this figure shows the acceleration of a four segment tubular actuator with these different loads. Figure 3.10 shows that when a constant mass is added as load, the value and place of the maximum acceleration change. For a larger mass the maximal acceleration gradually shifts to that mover radius (r_4) for which the force characteristic has a maximum (see figure 3.8).
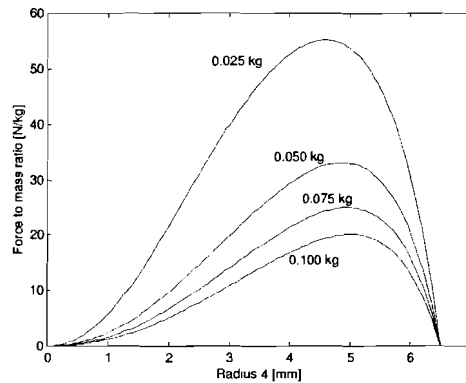
Figure 3.10: Acceleration of 4 segments for different load masses

3.3.2 Variable magnet and iron ring length

The length and width of the actuator are limited because of the limited space that is available in the z-theta module. To get the maximum amount of force out of the limited space the force density has to be optimal. In radial direction, the total diameter of the actuator is limited, because only an integer number of actuators can be placed next to each other in the z-theta module. For the solutions given in this report, this number is set at two. Looking at the length of the actuator this is a different story. Over the total length of the z-theta module (in z-direction), several parts occupy space: the linear motor, the rotary motor, the vacuum system, the sensor system and bearing system. How much of the total length is occupied by other systems than the linear motor is not yet clear at this stage. Even when looking only at the linear motor several solutions are possible. When using less long segments, it is possible to use more segments in the same space. Therefore, the force and acceleration are studied as a function of the segment length in this section. The two parameters that determine the length of the segment are the magnet length (l_{mag}) and the iron ring length (l_{ir}). The mover radius (r_4) is set at 5 [mm]. The other variables are still the same as described in table 3.1.

In figure 3.11, the force is shown that is produced per meter of tubular linear actuator length (force density). The figure shows that enlarging the iron ring length does not benefit the force that is produced. Only for small iron ring lengths, the rings are saturated and adding extra length to the rings could be beneficial. When varying the magnet length, a clear maximum force density is found. This maximum is located around $(\tau_m =)$ 8 [mm], and it ranges approximately from 6 to 11 [mm]. When using magnets that are longer than 11 [mm], the segment length could better be divided over more than one segment.

Because the mass density of iron (7400 $[kgm^{-3}]$) is only slightly higher than that of permanent magnetic material (7350 $[kgm^{-3}]$), the mover mass per meter length is nearly constant. Therefore, the acceleration as function of the magnet length and iron ring length has the same characteristic as the force characteristic of figure 3.11.
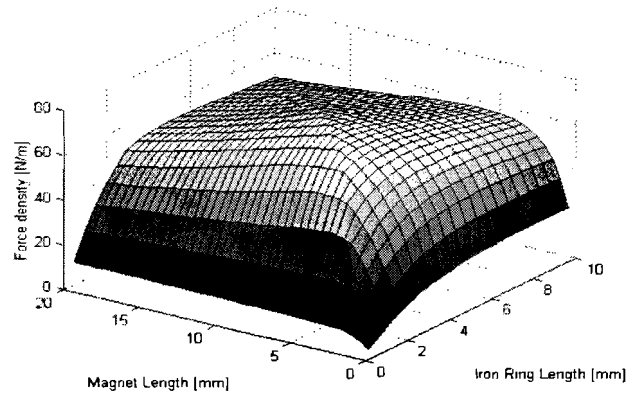
Figure 3.11: Force per meter length as function of the magnet length and iron ring length

3.3.3 Variable inner rod radius

Up to now, the inner rod placed on the mover axis is neglected. The magnets and iron inter-spacers were presumed to be solid cylinders. In this paragraph, the inner rod shown in figures 3.4, 3.5 and 3.6 is introduced to the model. The inner rod is used to create a mechanically strong, rigid mover. The magnets and iron inter-spacers are now rings. The hole in the ring is filled by the iron rod. In the MEC model the inner rod radius is indicated as radius 2 or r_2. Enlarging this radius not only results in removing permanent magnet material, but also creates a path for leakage flux, especially when using high-permeability iron as material for the rod. Figure 3.12 shows the force that is created as a function of the inner rod radius for high-permeability steel. The mover radius (r_4) is set at 5 [mm] and the magnet length (l_m) and iron ring length (l_{ir}) are 6 and 3 [mm], respectively. For a small inner rod radius (< 1 [mm]) the produced force does not decrease significantly. For a larger radius, the produced force diminishes rapidly.
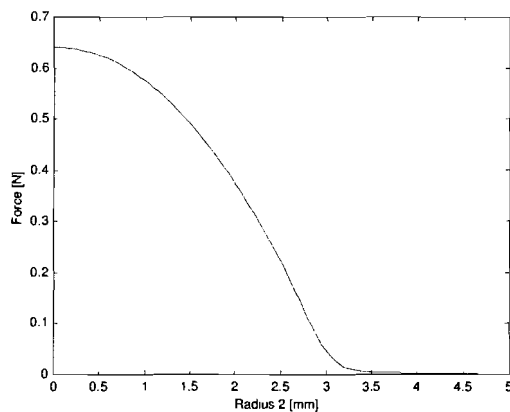
Figure 3.12: Force per segment as function of the inner rod radius (for a steel rod)
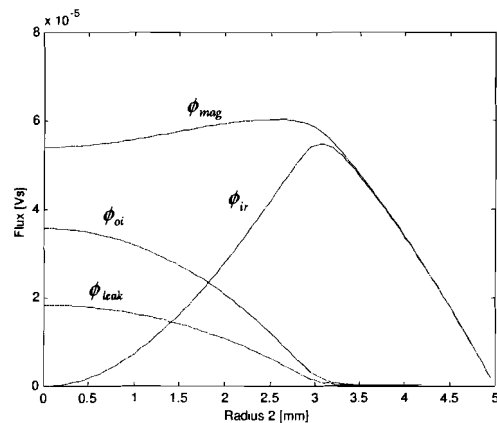
Figure 3.13: Magnitude of the flux in a segment in different flux paths as function of the inner rod radius (for a steel rod)

The use of an inner rod is necessary to create sufficient mechanical mover stiffness, but it can also be beneficial for the magnetic circuit. Looking at the flux in the different paths in the magneto electric analog scheme (figure 3.6) can prove this. In figure 3.13, the magnitude of the flux in the different paths is shown as function of the inner rod radius. ϕ_{mag} is the total flux coming from the magnet and this is the sum of the fluxes ϕ_{ir}, ϕ_{leak} and ϕ_{oi}. The figure shows that the magnet flux is increasing, up to

an inner rod radius of 3 [mm]. This means that the flux leaving the permanent magnet base is increasing, while the area of the permanent magnet is decreasing. Because the total reluctance of the magnetic circuit is lowered, the operating point of the magnet, as discussed in paragraph 2.3.2, is shifted upwards. This makes the permanent magnets more resistive to demagnetisation by both armature fields and temperature rise. However, while the magnet flux does not change in this interval, ϕ_{oi} decreases significantly. The flux that is indicated as ϕ_{mag} in figure 3.6 is the sum of ϕ_{ir}, ϕ_{leak} and ϕ_{oi}. The inner rod radius does not influence the airgap length and airgap area. Because the force is calculated with the Lorentz volume integral, the force is proportional to the airgap flux, as can be seen by comparing the airgap flux in figure 3.13 with the force plot in figure 3.12.

When the inner rod is not made of high-permeability steel, the leakage flux through the inner rod will change. In figure 3.14, the fluxes as shown in figure 3.13 are recalculated, but this time the inner rod consists of air. The fact that air is used originates from the preliminary MEC model. In this model, the inner rod is a hollow rod, to enable a vacuum feed through in the mover. The vacuum is responsible for locking the nozzle to the SMD component. Using any other material with a relative permeability near one instead of air, gives identical results.
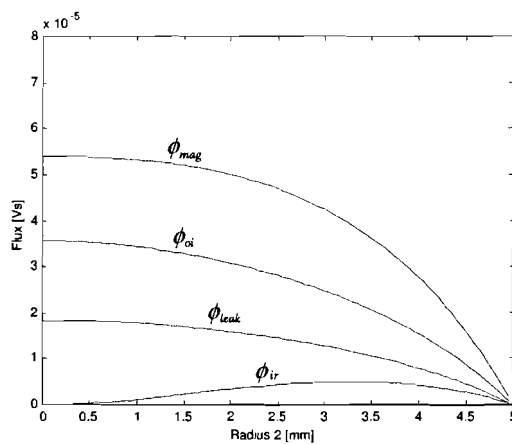
Figure 3.14: Magnitude of the flux in a segment in different flux paths as function of the inner rod radius (for an air rod)
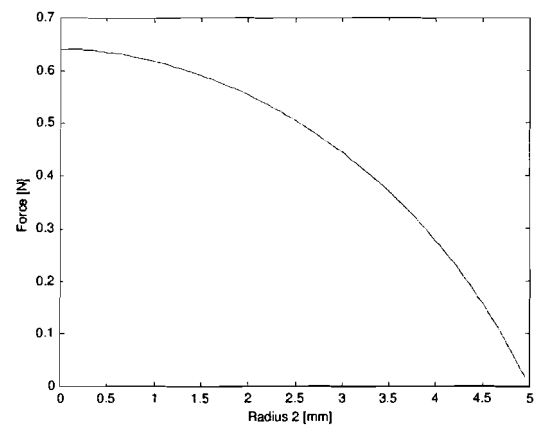
Figure 3.15: Force as function of the inner rod radius (for an air rod)

Figure 3.15 shows that the produced force can be increased for higher inner rod radii. This is achieved by using a material with low relative permeability. The advantage of shifting up the operation point is not present when using material with low permeability, as shown in figure 3.14.

3.3.4 Variable outer iron thickness

At the start of this section, the outer iron thickness $(r_8 - r_6)$ was set at 1 [mm]. This value was chosen because it was the exected that this value would not give any saturation in the outer iron, and would supply a rigid base for the stator build-up. In this paragraph, the thickness of the outer iron is varied to study at which point saturation in the outer iron starts to suppress the operating point of the magnets. The MEC model prevents the study for local saturation in stress points, but general saturation over the total length of a flux tube can be investigated.

In this paragraph, only the magnetic circuit is studied. Mechanical aspects that are a result of the magnetic optimisation are not considered. This means that this paragraph could indicate a certain outer iron thickness that would result in a fragile stator construction. This report does not cover a mechanical study.
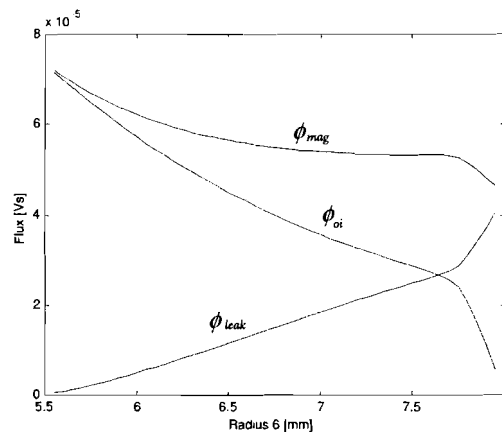
Figure 3.16: Magnitude of the flux in different flux paths as function of the inner radius of the outer rod

A smaller thickness of the outer iron, combined with a constant mover diameter, results in a longer airgap. This means that four reluctances in the MEC circuit of figure 3.4 change ($\mathcal{R}_{cop}$, $\mathcal{R}_{leak}$, $\mathcal{R}_{oir}$ and $\mathcal{R}_{oiz}$). The longer airgap over the copper volume gives a higher reluctance ($\mathcal{R}_{cop}$). A thinner outer iron results in higher reluctance for $\mathcal{R}_{oiz}$ and a smaller reluctance for $\mathcal{R}_{oir}$. The change in $\mathcal{R}_{oir}$ is small compared to the change in $\mathcal{R}_{oiz}$, so the total reluctance of the flux path trough the outer iron ($\mathcal{R}_{oqoi}$ in figure 3.6) increases. Besides these effects, the airgap leakage reluctance ($\mathcal{R}_{leak}$) decreases, because of a larger area of the flux tube base. All changes in reluctance cause a lowering of the flux that is contributing to the force production (ϕ_{oi}), as shown in figure 3.16. Where paragraph 3.3.1 was about finding the balance between magnetic and electric loading, this paragraph is about finding the balance between the electric loading and the reluctance circuit.

As shown in figure 3.16 the airgap leakage flux increases linearly with increasing inner radius of the outer iron, up to the point where the outer iron starts to saturate. This point is located around radius 6 equal to 7.8 [mm]. Before the saturation of the outer iron is present the airgap flux decreases, but not linearly. The magnet flux is nearly constant over the interval 6.5 to 7.8 [mm]. This means that, in this interval, the operation point of the permanent magnet material is hardly influenced by the inner radius of the outer iron.

Since the active (or airgap) flux is not decreasing very much and the electric loading increases linearly with increasing radius 6, the force produced by the actuator increases with increasing radius. Figure 3.17 shows the rise of the force for increasing the inner radius of the outer iron. This rise in force starts to saturate around a radius of 7 [mm]. From this point, only a small amount of force can be gained, before the force starts to drop due to the saturation of the iron. Since the mover radius is constant in
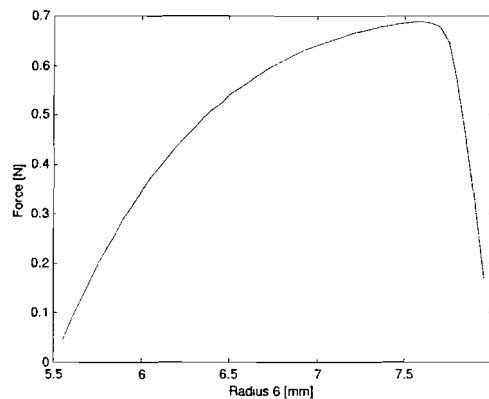
Figure 3.17: Force per segment as a function of the inner radius of the outer iron

this paragraph, the acceleration and the force have the same characteristic, with only a different scale.

3.3.5 Z-displacement

Up to now, the force is calculated for one single position in the movement interval. In this paragraph, the change in force is estimated as a function of the mover position. In other words, the force variation caused by a translational movement, equal to the distance between the coils (τ_c), is estimated. Using the values in table 3.1, $\tau_c = 3$ [mm]. In figure 3.18, the result of this simulation is shown. Figure 3.18 indicates that when the position of the iron ring is in the middle between two coils ($\Delta z = \tau_p/6 = \tau_c/2$) the force has a minimum value. This value is 86 % of the maximum value. A disadvantage of the MEC model is that the flux is presumed to cross the airgap perpendicularly. In practice, there is fringing of the field. Therefore, the B-field in radial direction has no block shape as shown in figure 2.10, but rather a more sinusoidal shape. A more sinusoidal field gives a more constant force. The shape of the B-field and therefore the force variation is dependent on the magnet pitch – pole pitch ratio (τ_m/τ_p) [4].
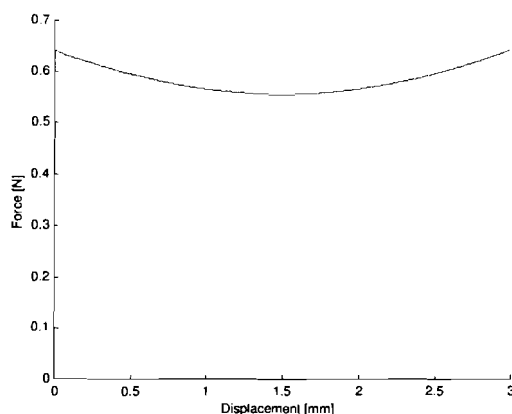
Figure 3.18: Force per segment as function of the mover displacement

3.4 Conclusions of the MEC model

After analysing the results of the parametric search with the MEC model, the initial selection of the sizes turned out to be well chosen. Paragraph 3.3.1 showed that the variable r_4 has a force optimum near 5 [mm]; this value was chosen in the initial estimation. A magnet length (l_{mag}) of 7 to 8 [mm] and an iron ring length (l_{ir}) of half l_{mag} give a force density maximum, where the initial estimated value was 6 and 3 [mm] for l_{mag} and l_{ir}, respectively. The force density for the initial values is about 95 % of the maximal force density, as shown in paragraph 3.3.2. The inner rod does not significantly influence the flux path, when the radius of the rod is small. Paragraph 3.3.3 shows that when this radius gets larger, the influence of the rod is dependent on the material it is made of. When the rod consists of air or another material with low relative permeability, the only problem is that the rod occupies part of the magnet volume. When an iron rod is used, the leakage flux through the rod becomes a significant problem. So the advise from this paragraph is: a small inner rod made of high permeability material does not influence the force production significantly, but for larger inner rod diameters, it is better to use material with low permeability. The produced force as a function of the inner radius of the outer rod, discussed in paragraph 3.3.4, shows that a thinner outer iron does not improve the force production of the tubular motor. When the outer iron becomes much too thin, saturation of the outer iron causes a force drop. Finally, paragraph 3.3.5 shows a force characteristic as function of the displacement. Because of the assumptions that are made when deriving the model, the force variation is expected not to be close to practice.

Since the trends found with the parametric search match the trends found within literature, the first steps of the design process can be taken with the MEC model. However, the accuracy of the model is still unknown. To get an idea of the accuracy of the MEC model, the results of this model have to be compared with other results. These other results can either be obtained by other modelling methods, or by measurements carried out on a test set-up. In the next two chapters, both methods will be discussed.

4 Two-dimensional FEM analysis

Finite Element Method (FEM) analysis is a numerical modelling technique for electromagnetic problems. In the Magnetic Equivalent Circuit (MEC) model the electromagnetic structure was discretised in a limited amount of elements, the flux tubes. In the Finite Element approach, the number of elements is increased extensively. The subdivision of the volume in FEM is called mesh. In two-dimensional FEM, the mesh elements have a triangular shape. After discretising the structure, the electromagnetic laws of Maxwell are solved for all the elements, in terms of the magnetic scalar potential (V_m) and magnetic vector potential (A). From these potentials, the most important parameters in the analysis of an electrical machine are derived. These parameters are: the flux density (B), the magnetic field intensity (H) and the flux linkage of the windings (λ). FEM allows the modelling of complex geometries and nonlinearities, without many restrictions and assumptions. The results of FEM are accurate, but calculation times are correspondingly long. The increasing speed of modern computers makes FEM increasingly a tool for optimisation processing, while in the past it was merely used as check for and fine-tuning of the results found with other models like MEC.

In this project, the software that is used is Ansoft Maxwell 9.0 and 10.0. A FEM software package most of the time consits of three parts (pre-processing, calculation and post-processing). In the first part of the FEM software package, the geometry is constructed. Materials with their specific electromagnetic properties are assigned to elements in the geometry. Current sources and boundary conditions are applied to the model. Finally, the mesh is created. In figure 4.1, an impression of the FEM geometry of the linear tubular actuator is shown. In the second part of the FEM software package, the electromagnetic problem is solved. In the case of Maxwell 9.0 and 10.0, the software has an adaptive mesh. When an error estimate, calculated by the software, is over a selected boundary value, the mesh is refined and the problem is solved again. This procedure is repeated until the required accuracy level is obtained. The third and final part of the software package is the analysis of the simulation results (post-processing).
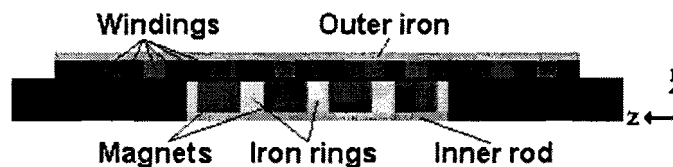
Figure 4.1: Impression of the FEM geometry of the linear tubular actuator.

In the FEM model, two different tubular actuator configurations are created. The first configuration is corresponding to that of the MEC model. This means that there are no insulator rings between the coils. The magnets and iron rings have a length of 6 and 3 [mm], respectively. There is no inner rod in the design, or it will be indicated in the text. The values of all the variables in this configuration can be found in table 3.1. The second configuration has insulator rings placed between the coils. The second configuration actually consists of two different (mover) configurations with an equal pole pitch. The magnet length is either 6 or 8 [mm] and the corresponding length of the iron rings is 4.6 or 2.6 [mm], respectively. Both second configurations are less compact than the first configuration. When constructing the test set-up, the insulator rings between the coils were larger than expected. Therefore, the FEM configuration was adapted to the test set-up configuration. The specifications of the configuration of the test set-up can be found in table B.1.

In the analysis of this chapter, the first configuration is used, except in paragraph 4.1.2 (EMF estimation), section 4.2 (Static thermal analysis) and section 4.4 (Performance analysis), where the second configuration is used. Where indicated, both mover configurations are used. If this is not indicated, the mover configuration with magnets of 6 [mm] is used.

4.1 Magnetostatic analysis

At the start of the evaluation of the linear permanent-magnet tubular motor with FEM, the structure is analysed for static behaviour. The flux distribution is studied throughout the geometry and the EMF waveform and amplitude are derived. With the results of this initial analysis, design changes can be made that can improve the performance of the actuator.

4.1.1 Flux density distribution

As indicated in chapter 3, the flux distribution must be known before a MEC model of an electromagnetic structure can be derived. FEM analysis is a way to investigate the flux distribution. The two most important aspects of the flux distribution are in this case: the direction of the flux lines and the (local) density of the flux lines, or flux density. With the distribution of the flux lines, the flux tubes of the MEC model can be determined. The distribution of the flux lines can also indicate that there is an unwanted leakage flux in the design, which can possibly be minimised by small changes to the design. The flux density can show places of increased density (> 1.5 [7]). In iron elements of the magnetic structure, the increased flux density can cause saturation. The reluctance of the iron drops, and the operation point of the magnet is lowered. Adding extra iron surface can prevent the saturation from occurring. Saturation will easily occur in small spots, especially in areas where the flux lines take a corner. These saturated spots hardly influence the reluctance. Only when the saturation is present in larger areas, there might be a problem.

Figure 4.2: Flux lines in one segment of the linear tubular actuator for: A) no inner rod, B) an inner rod made of soft magnetic material and C) an inner rod made of low permeability material

In figure 4.2, the flux lines of a segment of a linear tubular actuator are shown for three different configurations. Only one segment is shown, but FEM calculates for the total structure (figure 4.1). In figure 4.2 C, the different elements in the configuration are indicated. The radius of the inner rod (if present) is equal to 1.6 [mm]. There is no excitation current in the stator windings in all configurations. Configuration A shows the flux lines when there is no inner rod (the magnet and iron inter-spacers are solid cylinders). In configuration B, a high permeability iron inner rod is used (the magnets and inter-spacers are rings). A large amount of flux lines is going through the inner rod. Configuration C shows the flux lines when the inner rod exists of low permeability air. The results of configuration C do not differ much from configuration A. There is permanent-magnet material missing, but there is hardly any leakage flux through the inner rod. Therefore, the flux that contributes to the force production (the outer iron flux) is significantly higher for configuration C than for configuration B.
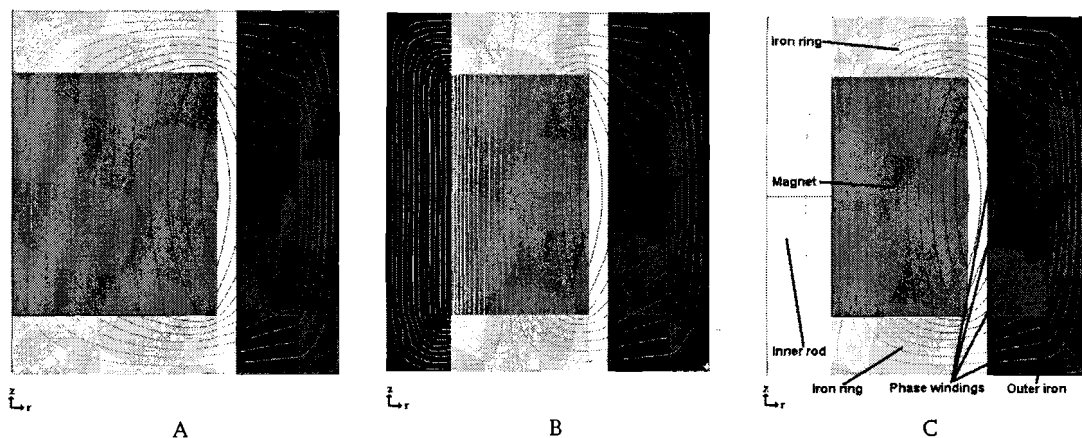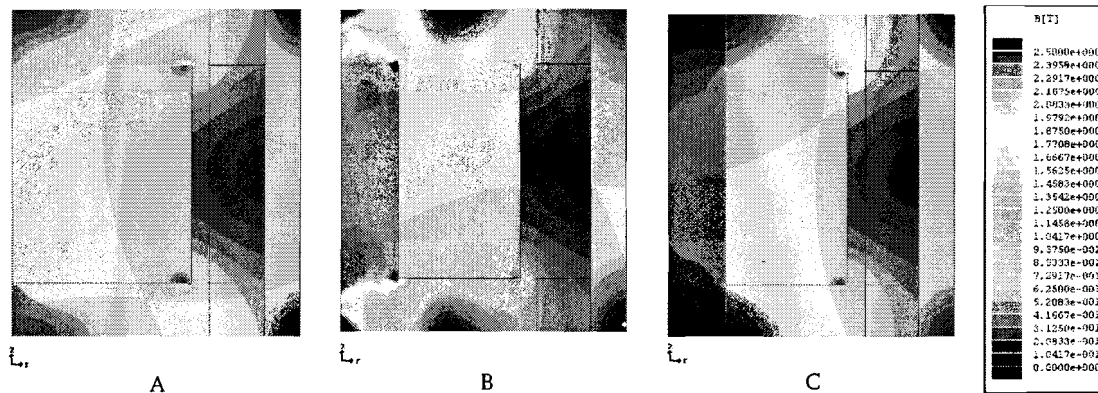
Figure 4.3: Flux density distribution in one segment of the linear tubular actuator for: A) no inner rod, B) an inner rod made of soft magnetic material and C) an inner rod made of low permeability material

The corresponding flux density distribution for the three different configurations is shown in figure 4.3. Configuration A shows the flux density when no inner rod is used; configuration B for an iron inner rod and configuration C for an inner rod made of air. Configuration B shows a highly saturated inner rod (> 2 [T]). In this case, saturation of the iron is an advantage, because without this saturation, the amount of flux lines through the inner rod would even be higher. The flux through the inner rod is unwanted because it does not contribute to the force production. The airgap flux density is low in configuration B because of the large amount of flux 'leaking' through the inner rod. This is also visible by the low flux density level in the outer iron. Configuration C does not differ much from configuration A, only the airgap flux density is somewhat lower. This is visible by the lower flux density level in the outer iron. The airgap flux density of configuration C is significantly higher than that of configuration B.

4.1.2 EMF estimation

In this paragraph, the EMF induced by the linear tubular actuator mover in the phase windings, is estimated by means of FEM. The EMF waveform established this way, can be compared to the EMF waveform measured with a test set-up that will be discussed in section 5.2. Therefore, not the initial configuration, as used for the MEC model is selected, but the geometry of the test set-up. This geometry is differing from the ideal topology on numerous points. The most important difference is that insulator rings are placed in between the coils of the stator. The total stator length has therefore increased from 72 [mm] to 85 [mm]. The mover length is adapted to the stator, to make the pole pitch of the mover equal to three times the coil pitch of the stator. There are two different mover configurations with equal pole pitch (τ_p). The first configuration uses magnets with a length (τ_m) of 8 [mm] and iron rings of 2.6 [mm]. The second configuration uses magnets with a length of 6 [mm] and iron ring of 4.6 [mm]. For both configurations, the pole pitch is 10.6 [mm]. In figure 4.4 the expected EMF waveforms, calculated by FEM are shown for the first configuration. In figure 4.5, the harmonic components of the EMF waveforms of figure 4.4 are shown.

The EMF waveforms of figure 4.4 are not sinusoidal. This is confirmed by the presence of a third harmonic in figure 4.5. Fortunately, in a three-phase system, third harmonics of the three phases cancel out each other when the phases are in y-connection. However, higher harmonic components cause force variations in the actuator as function of the mover displacement. The fundamental of the EMF has an amplitude of approximately 0.20 [V]. The FEM software calculates the EMF for solid copper coils (one turn) and all coils in parallel. To come to the values displayed in figures 4.4 and 4.5 the calculated value is multiplied by 312. This factor (312) is formed by multiplying 8 coils in series per phase winding with 39 turns per coil. This is the configuration of the phase windings in the test set-up. The test set-up will be discussed in chapter 5.
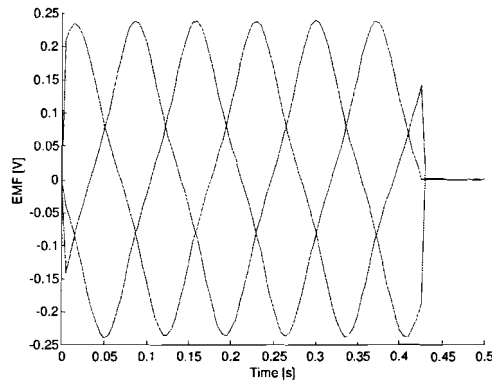
Figure 4.4: *Simulated EMF waveforms (with the 8 [mm] magnets and 2.6 [mm] iron rings mover configuration)*
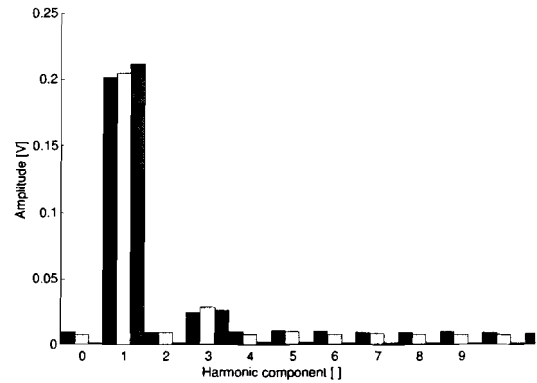
Figure 4.5: *Harmonic components of EMF waveform (with the 8 [mm] magnets and 2.6 [mm] iron rings mover configuration)*

Figures 4.6 and 4.7 show respectively the EMF waveforms and the harmonics of the EMF waveforms, of the second configuration (6 [mm] magnets and 4.6 [mm] inter-spacers). The waveforms are more sinusoidally shaped than the waveforms of the first configuration (8 [mm] magnets and 2.6 [mm] inter-spacers), but the amplitude of the EMF is lower. The amplitude of the fundamental of the EMF of the second configuration is also lower than the amplitude of the fundamental of the first configuration.
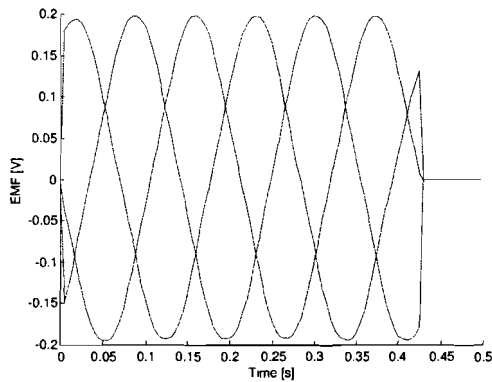
Figure 4.6: *Simulated EMF waveforms (with the 6 [mm] magnets and 4.6 [mm] iron rings mover configuration)*
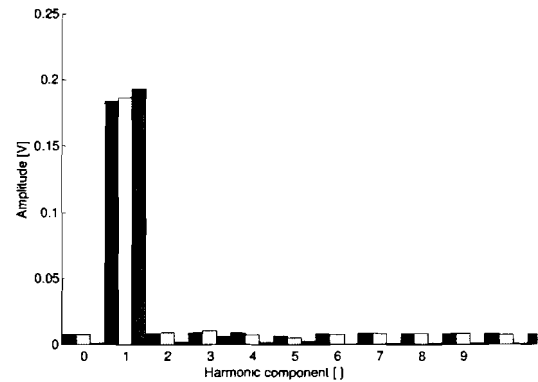
Figure 4.7: *Harmonic components of EMF waveform (with the 6 [mm] magnets and 4.6 [mm] iron rings mover configuration)*

As indicated by [4], force variations in a linear tubular motor are dependent on the ratio of magnet pitch (τ_m) and pole pitch (τ_p). A higher value of this ratio can increase the fundamental of the EMF waveform, but will also increase the force variations of the actuator. When the force variations are not a problem, a higher magnet pitch to pole pitch ratio is one of the possibilities to increase the force production of the actuator.

4.2 Static thermal analysis

The static thermal analysis is another possibility in the FEM software. The difference between a thermostatic analysis and a magnetostatic analysis is that the selected sources are thermal heat sources instead of electrical current sources and the boundaries are defined as thermal boundaries instead of electromagnetic boundaries. Because of the low frequencies that are used to excite the actuator windings the main source of heat is the copper dissipation.

The results of the static thermal analysis will be compared to the results of measurements in a test set-up. The test set-up is therefore the basis of the parameters selected in this test (table 5.1 or table B.1). The copper coils in the test set-up have 39 turns (n_{tc}). The radius of the wound wires (r_w) is 0.185 [mm]. The mean radius of the coils (r_{mc}) is 6.25 [mm]. The resistivity of copper is 1.7×10^{-8} [Ωm]. The resistance of the coils (R_c) can be calculated by:

$$R_c = \frac{\rho l}{A} = \frac{\rho n_{tc} 2\pi r_{mc}}{\pi r_w^2} \qquad (4.1)$$

Filling in the values mentioned above results in a theoretical resistance of: $R_c = 0.242$ [Ω]. For the source described in appendix C2, a RMS current of 1 [A] gives room for applying currents with RMS values that are even 80 % higher. By filling in the current value of 1 [A] in (2.11), the dissipated power per coil is 0.242 [W]. In the test set-up, eight coils are used to create one of the three phase windings, so the total dissipation is 1.94 [W] per phase winding. For the FEM thermal simulation, this results in a power of 2 [W] per phase winding. In the measurements carried out on the test set-up the current is adjusted, so that the power applied to the windings is constant. The example of 1 [A] is used to indicate that 2 [W] is a feasible value of dissipated power per phase, so this value is used in the FEM analysis.

There are three different principles for heat transportation: conduction, convection and radiation. In solid parts of the structure conduction occurs. Conduction can be described by Poisson's equation:

$$\nabla^2 T = -\frac{w}{k} \qquad (4.2)$$

Where T is the temperature in [K], w is the heat source density in [$Jm^{-3}s^{-1}$] and k is the thermal conductivity in [$JK^{-1}m^{-1}s^{-1}$]. For the heat transfer from a heated body to the surroundings, the principles are: radiation and convection. Radiation for a black body can be described by the Stephan-Boltzmann equation:

$$Q_{hf} = e_{sc}\sigma_{SB}A\left(T_s^4 - T_a^4\right) \qquad (4.3)$$

Q_{hf} is the heat flow in [Js^{-1}], A is the area of the surface of the body [m^2], σ_{SB} is the Stephan-Boltzmann constant of 5.67×10^{-8} [$JK^{-4}m^{-2}s^{-1}$], T_s is the temperature of the structure [K] and T_a is the ambient temperature [K]. e_{sc} is a scaling factor used to scale real surfaces to ideal black bodies. The value used in the FEM analysis is estimated with [12] and [13] and has a value of 0.85. Convection can be described by Newton's law:

$$Q_{hf} = \alpha_{conv}A\left(T_s - T_a\right) \qquad (4.4)$$

α_{conv} is the convection heat transfer coefficient [$JK^{-1}m^{-2}s^{-1}$]. This value is strongly dependent on the machine topology. In the simulation, a convection heat transfer coefficient is selected with a value of 10 (selected with help of [12] and [13]).

The results of the thermal simulations are shown in figure 4.8. Figure 4.8 A, B and C show the temperature distribution when 2 [W] is dissipated in respectively 1, 2 and 3 of the phase windings. In configuration B 4 [W] is dissipated in total and in configuration C 6 [W]. The temperature of the outer iron thereby reaches roughly 65°, 80° and 90° for the configurations, respectively. With such high
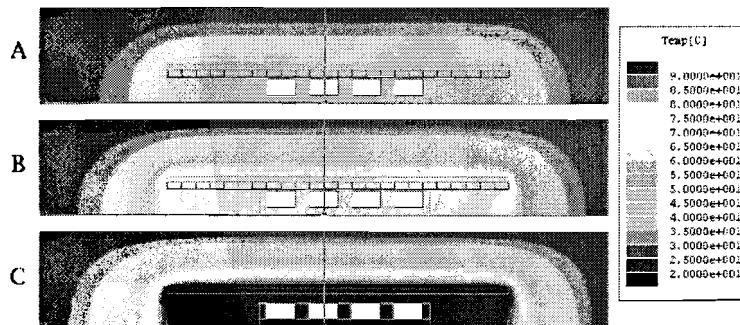
Figure 4.8: Temperature distribution for A) one of the phases, B) two phases and C) three phases dissipating 2 [W] per phase

temperatures, demagnetisation of the magnets is a critical point.

4.3 Optimetrical solutions

In this section, a parametric search is carried out by means of (static) FEM calculations. Where section 3.3 covers the results of the parametric search with the MEC model, this section does the same for FEM analysis. The same parametrical changes as applied in section 3.3 are carried out with the FEM software. The geometry has the same sizes as the sizes used for the MEC calculation. These sizes are listed in table 3.1. The position of the mover is the same as the position for the MEC analysis. When the force is calculated as function of the z-position, the current density in the windings is dependent on the mover position. It is sinusoidally distributed, in a three-phase system with an amplitude of 6.0 10^6 [Am^{-2}]. Contrary to the MEC model calculation, the force is not calculated for one segment, but is calculated over the total mover. Since the mover consists of four segments, as shown in figure 4.1, the results of the MEC model have to be multiplied by a factor four before the calculation results can be compared.

4.3.1 Mover radius

The calculated value of the force produced by the linear tubular actuator as function of the mover radius (radius 4) is shown in figure 4.9. When the mover radius is increasing the inner radius of the electric coils is increasing. Therefore, the electric loading (Q) is decreasing. With this test, an optimal balance can be found between the volume of permanent magnet-material (magnetic loading) and the copper volume (electric loading). Because the FEM results in this section (4.3) must be compared with the MEC model results, there is no inner rod in the configuration (except for paragraph 4.3.3). The maximum force is produced at a mover radius of 4.8 [mm].
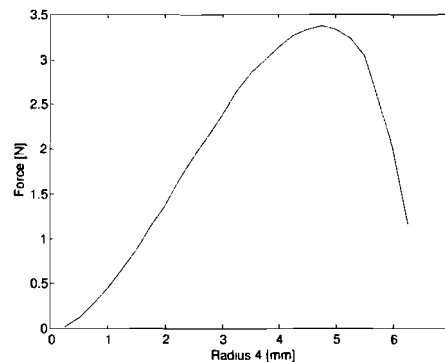
Figure 4.9: Force as function of the mover radius (FEM)

4.3.2 Magnet and iron ring length

Because the limited space in the z-theta module is a major restriction, the optimal force density of the actuator has to be found. In x-direction an integer number of solutions can be found, since only an integer number of actuators can be placed next to each other in x-direction. For the length (z-direction), this is a different story. Over the total length of the z-theta module, several elements must be placed. The linear motor, rotary motor, a sensor system, a vacuum system and bearings are the elements that have to be placed in the limited length. Therefore, the performance of the linear tubular actuator must be known as a function of the actuator length (in z-direction). In figure 4.10 the produced force per meter actuator length is shown as a function of the magnet length (τ_m) and iron ring length (τ_p - τ_m).
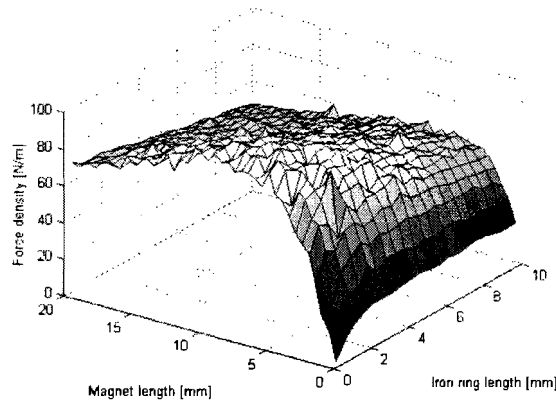
Figure 4.10: Force per meter actuator length as function of the magnet length and iron ring length (FEM)

Figure 4.10 shows similar results as the results found with MEC (figure 3.11). The optimal force density is at the same magnet lengths interval of 6 to 11 [mm], with a maximum around 8 [mm]. The corresponding iron ring length of the optimal configuration is in the interval 1 to 2.5 [mm]. The exact location of a maximum cannot be determined, because the inconsistent meshing of FEM (varying number of mesh triangles) results in noise on the characteristic.

4.3.3 Inner rod radius

Where the inner rod was neglected in the previous two paragraphs, this element is introduced to the actuator design in this paragraph. The inner rod is placed on the z-axis of the actuator. It is used to strengthen the mover. The radius of this rod can be varied, just as the material the rod is made off. By placing an inner rod into the design, space previously occupied by the permanent-magnet volume is now occupied by the inner rod. A path is created for flux that can 'leak' through the inner rod in the centre of the mover, thereby lowering the airgap flux density. As described in paragraph 3.3.3 this is a bigger problem for an iron inner rod than for an inner rod made of material with a relative permeability close to 1.
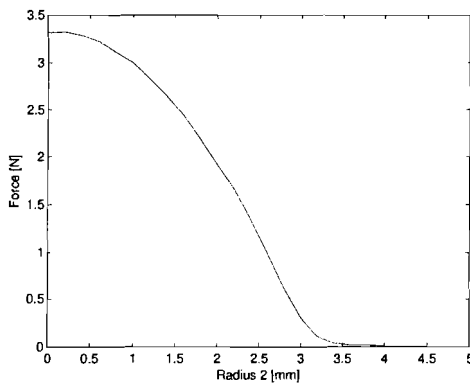
Figure 4.11: Force as function of the inner rod radius (for a steel inner rod) (FEM)
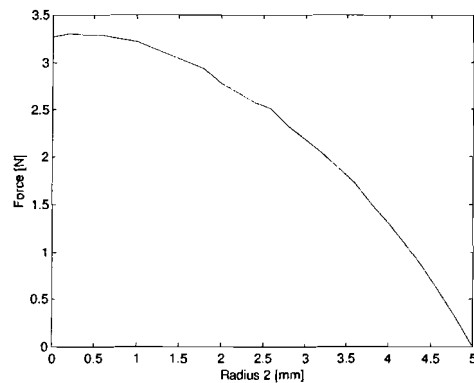
Figure 4.12: Force as function of the inner rod radius (for an aluminium inner rod) (FEM)

In figures 4.11 and 4.12, the force produced by the actuator is shown as a function of the inner rod radius. The mover radius is 5 [mm], so when the inner rod radius is 5[mm], there is no permanent magnet material in the topology. The difference between the figures 4.11 and 4.12 stresses the use of a non-ferromagnetic material for the inner rod. For the FEM calculation of figure 4.12, the material aluminium with a relative permeability of 1.00 is used. For the topology with iron (figure 4.11), the flux

through the inner rod is increasing faster for higher inner rod radius than for aluminium. The factor that limits the force drop in the figure is saturation of the iron. However, when the area of the iron is large enough, the iron does not saturate much. A short circuit for the magnetic flux is created through the inner rod. For a small diameter of the inner rod, there is hardly any difference between an iron or aluminium inner rod.

4.3.4 Outer iron thickness

The influence of the outer iron on the magnetic circuit in the actuator is studied in this simulation. The results can be compared to the results of the MEC model in paragraph 3.3.4. The inner diameter of the outer iron (radius 6) is the only thing that changes. The outer diameter of the outer iron (radius 8) is constant. For a higher value of radius 6, the airgap length is increased. The operation point of the permanent magnet lowers, and the airgap flux density drops. For lower values of radius 6, there is not much space left for the copper windings. There are no windings when radius 6 is 5.5 [mm] and for radius 6 equal to 8 [mm] there is no outer iron. Figure 4.13 shows the results. These results show that the force produced by the actuator increases together with an increasing inner radius of the outer iron. This increment stops when the outer iron starts to saturate. The saturation starts to occur at an inner radius of the outer iron of approximately 7.6 [mm]. The outer iron is then 0.4 [mm] thick.
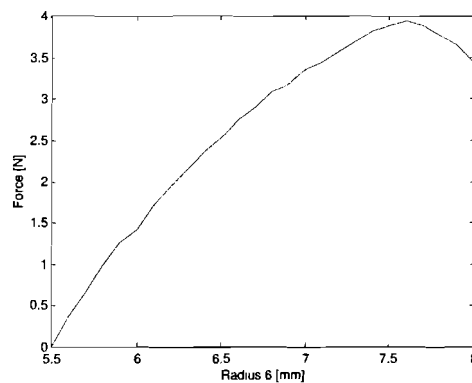
Figure 4.13: Force as function of the inner diameter of the outer iron (FEM)

4.3.5 Z-displacement

In this paragraph, the mover translates over a length equal to the coil pitch. The three-phase sine wave stator currents thereby change over 60 electrical degrees. The results of this simulation are shown in figure 4.14. This figure shows a constant force that is independent of the mover position. It is not possible to find a periodic deviation in the figure, equal to the pole pitch, magnet pitch or any other parametric frequency. The small deviations that are present in the picture can be subscribed to quantisation noise of the changing mesh of the FEM model. Since there is no periodic deviation in the force, the detent force of the stator windings on the iron rings of the mover cannot be obtained in this simulation. This effect will be explained and calculated in section 4.4.
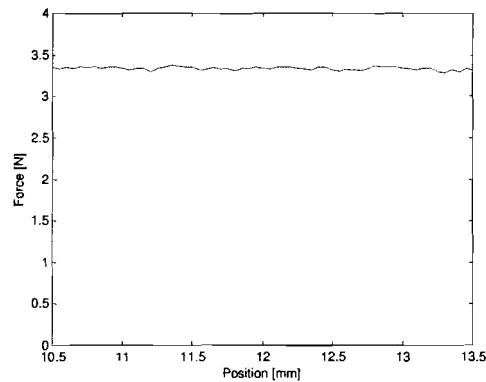
Figure 4.14: Force production as function of the z-displacement (FEM)

4.4 Performance analysis

In the MEC model of chapter 3, the reluctance force was neglected. The reluctance force is the force coming from the excited electric coils on the stator and acting on the iron rings in the mover. The MEC model calculates results for one segment of a linear motor. Therefore, the MEC model did not incorporate the possibility to calculate the cogging force. The cogging force is the force that occurs when the mover reaches one of the stator ends. The shape and magnitude of the reluctance force and cogging force can be calculated by FEM. By removing the permanent magnets from the mover and replacing them with a material with no permanent magnetic properties and an equivalent reluctance, the permeability force can be calculated. The cogging force can be calculated by calculating the force without applying any current to the stator windings.

In figure 4.15, the reluctance force is shown as function of the displacement. The relative permeability of the fictive material, the permanent magnets are replaced with, is 1.1. Note the scale of the vertical axis. When the mover reaches one of the stator ends the detent force increases significantly. However the detent force is smaller than 0.5 % of the total force at every position.
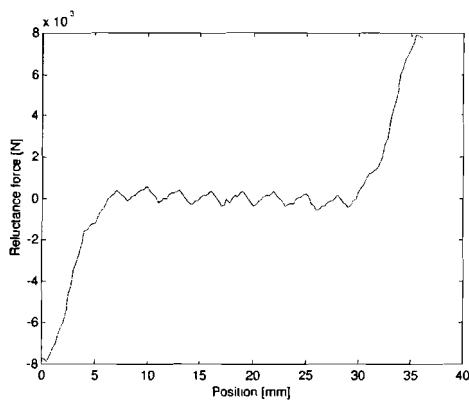
Figure 4.15: Detent force as function of the mover displacement (FEM)
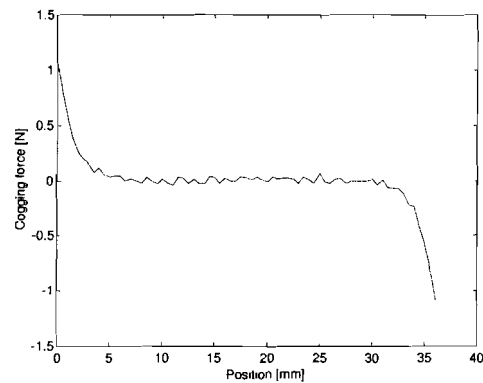
Figure 4.16: Cogging force as function of the mover displacement (FEM)

In figure 4.16, the cogging force is shown as function of the displacement. For position 0 [mm], the mover is again at one end of the stator. The iron ring of the mover then has the same z-position as the start of the copper and iron of the stator. The cogging force is strongly increased in this region.

Contrary to the detent force; the cogging force is a significant part of the total force. At the opposite end of the displacement characteristic the same effect is visible for the other stator end, with an opposite polarity of the force. The first 3 [mm] of the stroke are strongly affected by the cogging force, which is in absolute value going up to approximately 1 [N] at both ends of the stroke.

In paragraph 4.3.2 the results of a parametrical search show that a higher magnet pitch to pole pitch ratio (τ_m/τ_p) gives a higher force production, because the volume of permanent-magnet material is increased. In paragraph 4.1.2, the results of the EMF waveform however show that a higher τ_m/τ_p ratio results in higher harmonic components of the flux distribution in the airgap and therefore force variations. Is there a way to increase the magnet volume without changing the magnet pitch? Can the advantage of a high airgap flux density created by using as much permanent magnet material as possible (instead of iron rings) be combined with the advantage of a sinusoidal distribution of the flux in the airgap? This question is answered by using a Halbach configuration for the permanent-magnet material in the mover. In this configuration, the axially magnetised permanent magnets are not interspaced by iron rings, but by radially magnetised permanent magnets. The Halbach magnet configuration of the mover is shown in figure 4.17. The direction of the magnetisation of the magnets is indicated by white arrows.
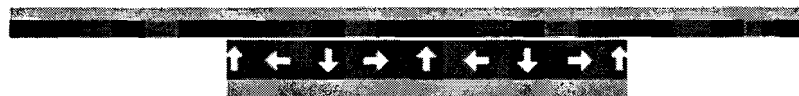
Figure 4.17: Halbach magnet configuration in the mover

The second of the two test set-up configurations (6 [mm] magnets and 4.6 [mm] iron rings as used for figure 4.6 and 4.7) has a sinusoidal EMF. When using the same sizes as this configuration, the results of the EMF waveform for the Halbach configuration and the harmonic components in the EMF are shown in figure 4.18 and figure 4.19, respectively. These figures can be compared to the figures with only axially magnetised magnets (figures 4.4 to 4.7). A Halbach configuration gives a significant rise of the EMF. The amplitude of the first harmonic of the EMF waveform for a Halbach configuration is 0.27 [V]. The amplitudes of the first harmonic of the configurations with only axially magnetised magnets are 0.20 and 0.18 [V], respectively.

According to figure 4.19, there is a small third and fifth harmonic in the EMF waveform of the Halbach configuration. These harmonics are however smaller than the third harmonic in the first test set-up configuration (figure 4.4 and 4.5). Fine-tuning of the sizes of the axially magnetised and radially magnetised magnets can possibly even remove the harmonic components for the Halbach configuration, without changing the amplitude of the EMF waveform significantly. Using a Halbach configuration also eliminates the reluctance forces that are previously described. The Halbach configuration of the mover is therefore a way to increase the performance of the tubular linear actuator.
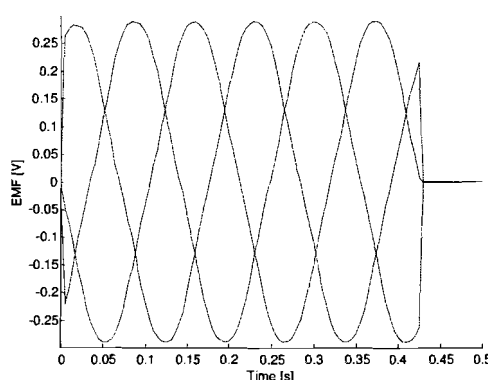
Figure 4.18: Simulated EMF waveform of a Halbach configuration with 6 [mm] axially magnetised magnets and 4.6 [mm] radially magnetised magnets
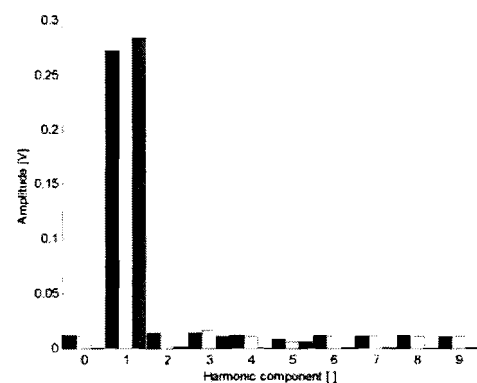
Figure 4.19: Harmonics of the three phases EMF waveform of a Halbach configuration with 6 [mm] axially magnetised magnets and 4.6 [mm] radially magnetised magnets

4.5 Comparison of FEM and MEC results

Theoretically, the differences between the FEM and MEC model are that the MEC model is based on a number of assumptions and a discretisation of the volume in a limited number of elements. The FEM model is based on the discretisation of the volume in a large number of finite elements. The assumptions that are made for the MEC model indicate the weakness of the model. For instance, all flux lines are assumed to run perpendicular to the base inside the different flux tubes. In the MEC model, it is assumed that there is no fringing of flux lines, not even in the airgap. These are two assumptions on which the results of FEM differ from MEC. This can be seen in the flux line plot of figure 4.2 A, B and C. The result of this is that the airgap reluctance calculated in the MEC model is larger than that of the FEM model. The fringing increases the area of the airgap, thereby lowering the airgap reluctance. In addition, the possibility of flux lines to run outside the outer iron is not embedded in the MEC model.

When the results of the FEM simulations are compared to those of the MEC model, there is a trend visible. Generally, the shape of the graphs is (nearly) identical, but there is some deviation in magnitude. The force calculated with the MEC model, is the force produced by one segment. FEM calculates the force for the total structure. When the results of the MEC model are multiplied by a factor four (for four segments in series in the actuator), the force calculated by the MEC model is generally approximately 80 % of the force calculated by the FEM model.

Especially when looking at the paragraphs 4.3.1 and 4.3.3, the figures have the same shape as their MEC equivalent (in the paragraphs 3.3.1 and 3.3.3), only the magnitude is different. For the variable magnet length and iron ring length discussed in paragraph 3.3.4, the maximum force density of the FEM model (figure 4.10) is present at the same magnet lengths as found with the MEC model. The corresponding iron ring thickness at the maximum force density however, is lower for the FEM model than for the MEC model. This is caused by the fact that it is assumed that there is no fringing of the flux lines in the MEC model. For the variable outer iron thickness discussed in paragraph 3.3.4, the saturation of the outer iron in the FEM model does not influence the force production as much as in the MEC model. This is caused by the fact that in the FEM model the flux lines also have the possibility to run outside the outer iron (through the air outside the actuator), while this possibility is not present in the MEC model. Finally, the results of the force as function of the mover displacement also differ because the fringing of the flux in the airgap is neglected in the MEC model. The distribution of the (radial) flux in the airgap is therefore more sinusoidal in the FEM model than in the MEC model. The force production is therefore more constant in the FEM model. The sinusoidal flux distribution in the FEM model results in less force variation.

5 Experimental set-up

5.1 Set-up description

To verify the results obtained by the two different modelling methods (MEC and FEM), a test set-up is built. In the first section of this chapter, the construction of the linear tubular motor for the set-up is described. Dependent on the measurement, different elements are added to the set-up. For the EMF measurements of section 5.2, a device is attached externally, that moves the mover at a constant speed through the stator. Figure 5.1 shows the set-up for this measurement. On the left of this figure a z-theta module is shown, containing a linear actuator and a rotary motor. The tubular motor stator is lying behind the tubular motor mover. For the thermal measurements of chapter 5.3, a thermal camera is used. The force measurement of chapter 5.4 requires the use of a force sensor and a scale to adjust the mover displacement. These added measurement equipment is explained further in the different sections. At the end of the chapter, in section 5.5 the results of the measurements are compared with the modelling results of both modelling methods, MEC and FEM.
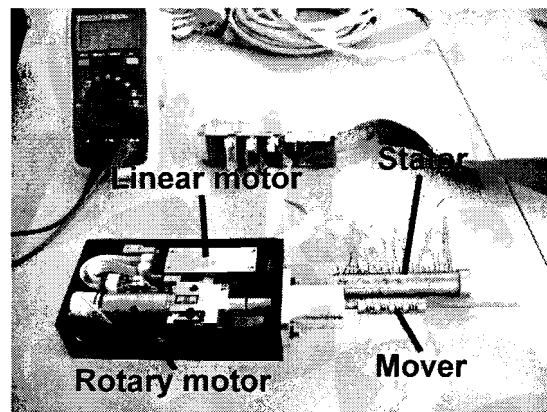
Figure 5.1: Set-up used for the EMF measurements

The base of the experiments is the linear tubular actuator. The actuator consists of two parts, stator and mover. These parts are separated by the airgap. The connection of mover to stator is made without bearings. Ordinary busses at both stator ends keep the inner rod of the mover in the centre of the stator tube.

5.1.1 Mover construction

The mover contains the permanent magnet material. The axially magnetised magnets are alternated with iron separators. An iron inner rod completely fills the hole in the magnetic and iron rings. This inner rod gives stability to the mover. It also forms the interface of the mover to the outer world. For instance, this rod is attached to the force sensor, when the force is measured. The magnets and iron rings are fixed to the rod by an Allen bolt in the iron rings at both mover ends. The sizes of the iron rings at both mover ends are different from the iron ring in between the magnets. These rings are somewhat longer, so they can occupy the bolts. The iron that is used is steel 37, as discussed in paragraph 2.3.3.

The permanent magnet material is a key component in the test set-up construction. The choice has been made to order pre-fabricated magnets. The production of customised magnets would have taken to much time. The choice was made for a neodymium (NdFeB) magnet ring with inner diameter 3.2 [mm], outer diameter 10 [mm] and a length of 2 [mm]. The material grade of the magnet is N38H. The demagnetisation curve of the magnets is shown in appendix B.2. To come to the desired magnet

length, multiple (3 or 4) rings are cascaded, to form a 'single' magnet of 6 [mm] (or 8 [mm]), as shown in figure 5.2.
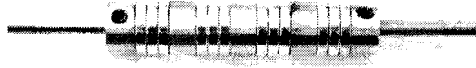
Figure 5.2: Picture of the mover of the set-up with iron rings alternated by three magnet rings

An inner rod has been created that holds the magnet rings. The diameter of the inner rod is therefore 3.2 [mm]. Next, the iron rings have been created, three rings of 3 [mm] separating the magnets and two somewhat larger rings at both ends. Later, due to production problems with the stator, the length of the three iron rings was adapted, so the pole pitch of the mover was matching the coil pitch of the stator. The new iron rings have two different lengths, 2.6 [mm] and 4.6 [mm]. The iron rings of 2.6 [mm] are used in combination with a stack of four permanent magnet rings (of 2 [mm]) to create a pole pitch of 10.6 [mm], and the rings of 4.6 [mm] are used with a stack of three permanent magnet rings (of 2 [mm]) so the pole pitch is also 10.6 [mm]. The latter construction is shown in figure 5.2. The iron rings at both mover ends are 5 [mm] in length.

5.1.2 Stator construction

The stator consists of copper coils and an iron tube. During the construction of the stator, the coils are glued together on an inner rod. When the inner rod is removed, the inner gap of the coils is smooth. Small rings of electric (and also thermal) insulators are glued between the coils. After the coils are glued together, they are shoved into the iron tube. Because the electric connections of the coils need to be on the outside of the iron tube, a slit is made over the entire length of the tube. The coils are then connected to each other outside the iron tube, in the way that is shown in figure 5.3.

The coils are manually wound, and the sizes are estimated from the sizes of the magnet rings (especially outer diameter), and initial calculations. The airgap is chosen to be 0.5 [mm], so the inner diameter of the coils is 11 [mm]. When the orthocyclic windings are formed, the crossing over of the wire is always at the same position of the coil circumference. Therefore, the coils are somewhat thicker at this particular place.

A problem during construction is that the insulation of the coils becomes damaged by the sharp edges of the slit in the iron tube. The damage occurs when the coils are shoved into the iron tube. With the insulation gone, short circuits appear at random places. Covering the sharp edges of the slit with transparent tape solves this problem.
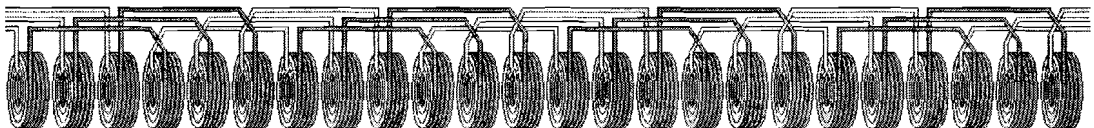
Figure 5.3: Impression of the connection of the coils forming the three phases

The problem mentioned briefly in the previous paragraph, is that the pieces of insulation, placed between the coils, are thicker than accounted for. Because the length of the insulation is added to the coil pitch, the coil pitch is larger than intended. The manually wound coils have a thickness of approximately 2.9 [mm]. Including the insulators, the coil pitch becomes 3.5 [mm]. In table B.1 (appendix B.1) the specifications of the test set-up are listed.

5.2 EMF measurements

The first experiment is a measurement of the induced Electro Motive Force (EMF) in the stator windings. When the mover is moved at a certain speed through the stator coils, the changing magnetic field induces the EMF. This EMF can be estimated by measuring the voltage across the phase windings. Each coil contains 39 turns and eight coils are placed in series per phase. The winding direction is reversed every pole pitch as displayed in figure 5.3.

For this measurement, the tubular motor is attached to a z-theta module as used in previous versions of the AX machines of Assembléon. The stator is fixed to the module housing and the mover is fixed to the translating and rotating nozzle holder. In figure 5.1 the set-up is shown, with the mover attached to the moving parts of the z-theta module. The stator, lying behind the mover in figure 5.1, must be placed over the mover and attached to the z-theta module housing. With the rotation of the z-theta module the mover can be rotated in the stator. This effect can be used to determine whether the measured EMF is rotation angle dependent, although it is expected that there is no dependency on the rotation angle. The translation range of the z-theta module is maximally 27 [mm]. Because the range of motion of the tubular motor is 37 [mm], the EMF waveform can only be measured partially and not for the maximal displacement.
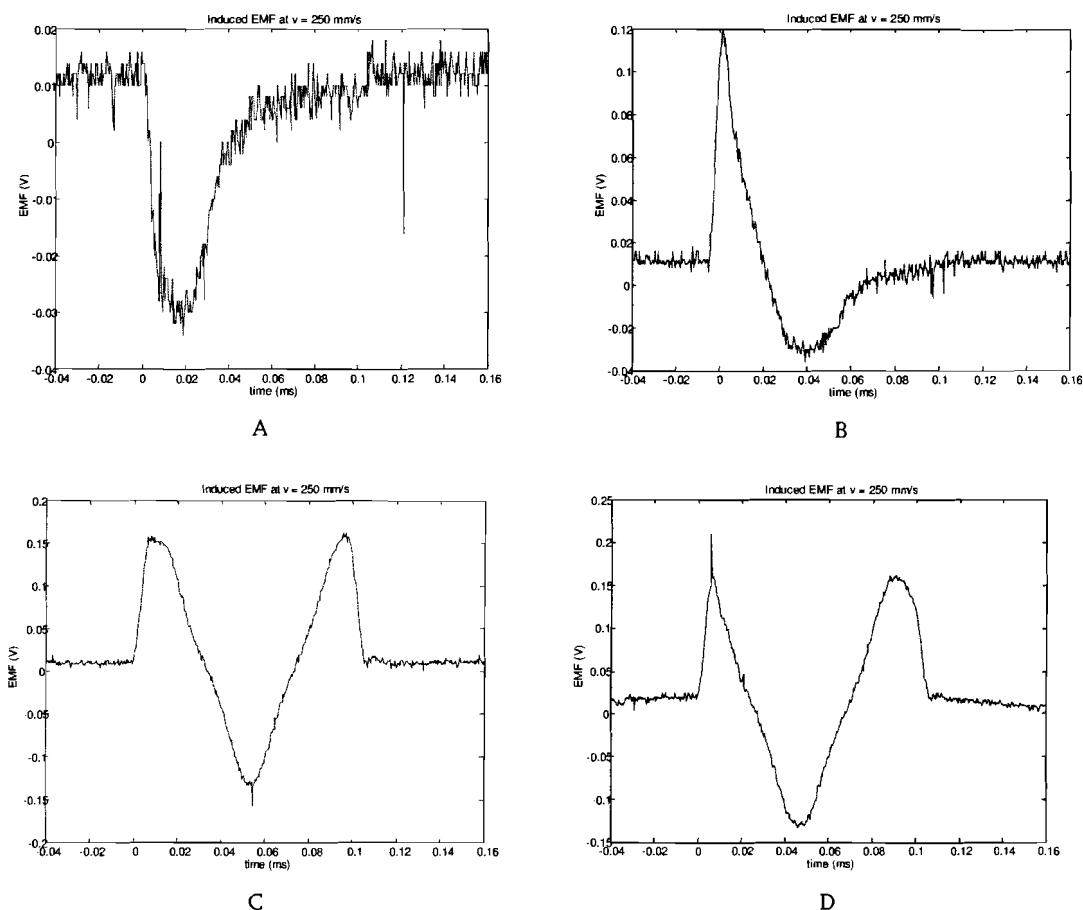
Figure 5.4: Measured EMF waveforms for different coils in the stator

5.2.1 Individual coil EMF measurement

Figure 5.4 A, B, C and D show the measured EMF over individual coils in the stator. The speed of the movement is 0.25 $[ms^{-1}]$. The place of the coils varies from: A at the start of the stroke via B and C to D the middle of the stroke. Over the middle of the stroke, the wave shapes are reversed versions of the shapes of the first stroke half, ending with the reversed shape of A at the mover end. The waveforms are reversed both horizontally and vertically.

From figure 5.4 can be determined that the contribution to the total EMF of the coils at the start and the end of the stroke is minimal. Still these coils are needed to make the force characteristic as constant as possible over the total stroke length. During this test, rotation of the mover with the z-theta module showed that the EMF is not dependent on the rotation angle of the mover inside the stator.

5.2.2 Phase EMF measurement

The measurements for determining the EMF of the phases are carried out with two different mover set-ups. These two set-ups are discussed in section 5.1.1. The number of magnet rings is either 3 or 4, combined with iron inter-spacers that are adapted in length to the number of rings, to make the pole pitch constant. Therefore, the mover geometry can easily be changed without changing the pole pitch of the mover. The stator can remain untouched, since the pole pitch is constant and the coil pitch is adapted to the pole pitch. In the first configuration, a mover segment consists out of four magnet rings (of 2 [mm]) alternated with an iron ring of 2.6 [mm]. In the second configuration, three magnet rings (of 2 [mm]) are used and the iron rings are 4.6 [mm]. For both configurations, the total mover consists of 4 segments. The EMF is measured in two directions, moving the tubular motor mover away from and towards the z-theta module housing. The speed of the movement is set at 0.10 $[ms^{-1}]$.
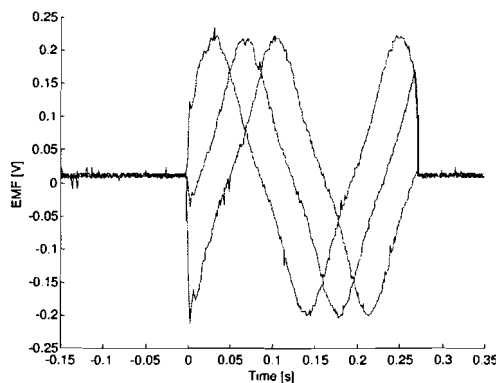
Figure 5.5: EMF waveforms in the windings (with the 8 [mm] magnets and 2.6 [mm] iron rings mover configuration)
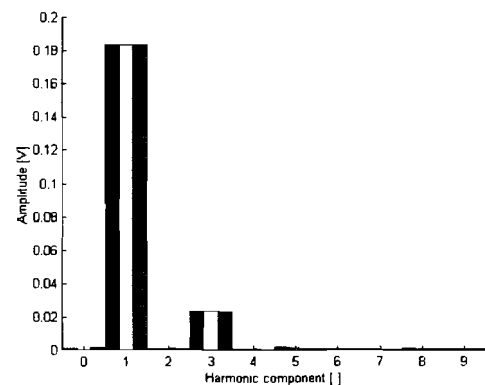
Figure 5.6: Harmonic components of EMF waveform (with the 8 [mm] magnets and 2.6 [mm] iron rings mover configuration)

Figure 5.5 shows the measured EMF of the three phases for the configuration with four magnet rings. The three waveforms have a phase difference of 60°. This phase difference is caused by the fact that one of the phases should be connected with opposite polarity. When the three phases are connected in the right way, a three-phase system with a phase difference of 120° is created. Measuring the EMF backwards gives similar results as discussed in paragraph 5.2.1. Also visible in figure 5.5 is that the waveform of the measured EMF is not sinusoidal. Figure 5.6 shows the amplitude of the harmonic components in the EMF. The figure shows a significant amplitude for the third harmonic. The harmonics in the EMF waveforms are caused by a non-sinusoidal flux distribution in the airgap. Higher harmonic components in this flux distribution increase the force variation in the tubular actuator force-displacement characteristic (see figure 3.18).

In figure 5.7 the measured EMF is shown for three magnet rings alternated with an iron ring of 4.6 [mm]. The phase difference in the signal of the three phases is the same as in the previous configuration. However, the waveform has a more sinusoidal shape. This is confirmed by figure 5.8

showing the harmonic components of this configuration. A small third and fifth harmonic component are visible, so the third harmonic component of the previous configuration has almost disappeared. A disadvantage is that the amplitude of the first harmonic for this configuration is 17 [mV] ($\approx$ 10 %) smaller than the first harmonic of the configuration with 4 magnet rings.
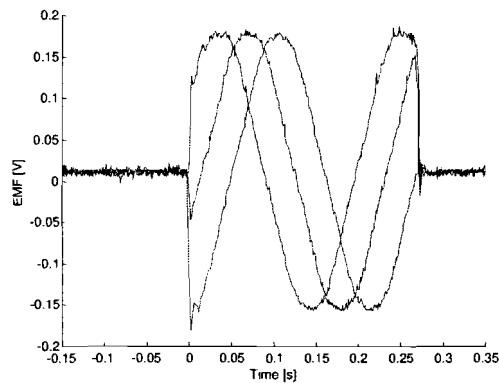
Figure 5.7: EMF waveforms in the windings (for 6 [mm] magnets and 4.6 [mm] iron rings)
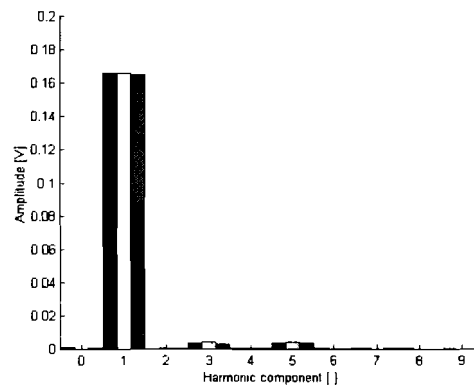
Figure 5.8: Harmonic components of EMF waveform (for 6 [mm] magnets and 4.6 [mm] iron rings)

In the last configuration, the amplitude of the fundamental of the EMF is 0.165 [V], and the velocity of the mover is 0.10 [ms^{-1}] Now the EMF-constant (k_E) can be calculated with (2.21) and (2.32). The calculated value of k_E is 2.86 [Vsm^{-1}]. An estimation of k_E can be calculated with (2.33). Filling in the parametric values of table B.1 and an estimated magnitude for B_I of 0.6 [T], the value of the EMF constant (k_E) is: 2.9 [Vsm^{-1}].

5.3 Force measurements

The force produced by the linear tubular actuator is measured in this section. Therefore, the mover of the linear tubular actuator is attached to a force sensor. The stator is attached to a scale with which the displacement can be adjusted. A picture of the force measurement set-up is shown in figure 5.9. At the right of the picture, the scale is visible. In the centre of the picture the force sensor is shown. The stator, in the top left of the picture, is taken out of the set-up, so the mover is visible. During the measurements, the stator is fed by a sinusoidal three-phase voltage controlled current source. Because the mover is fixed at one position by the scale, the force on the mover is a sinusoidal function of time. The signal of the force sensor is visualised on an oscilloscope, together with the current through one of the phases. A current probe measures this current. Though the magnitude of the current is presumed to be constant, some variations occur. These variations cause variations in the magnitude of the force. A direct link between the magnitude of the current and the simultaneously measured force could not be detected by measurements. Therefore, the signals are averaged over 32 measurements, also because the force sensor produces a significant amount of noise. The averaging reduces the sensor noise and gives a better relation between the averaged force and the averaged current. The maximal displacement that can be achieved with the scale is 20 [mm]. The measurement is influenced by mechanical friction at the end of the stroke. Therefore, the measured stroke is only 16 [mm].
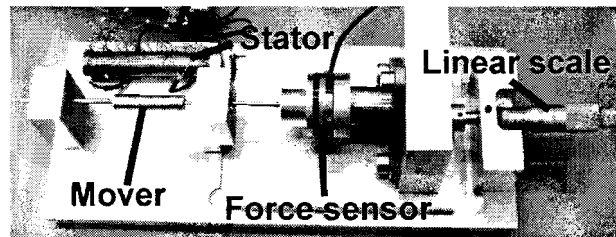
Figure 5.9: Picture of the force measurement set-up

Figure 5.10 shows the measured RMS value of the current through one of the phase windings as a function of the displacement. The peak-to-peak voltage on the current probe is read from an oscilloscope, and converted into a RMS current value. The measured current values in the figure are constant and have an approximate value of 0.71 [A]. The maximal deviation from this value is 2.7 %.
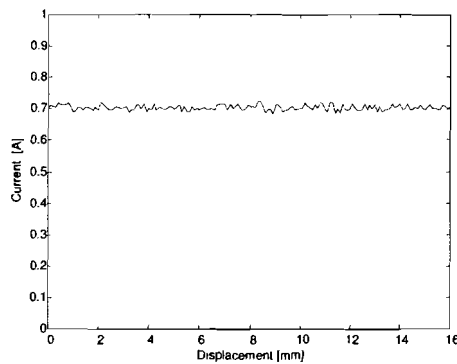
Figure 5.10: RMS value of the current as a function of the displacement
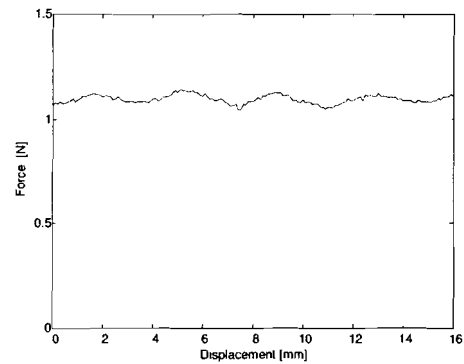
Figure 5.11: Amplitude of the force as a function of the displacement

The amplitude of the force is shown in figure 5.11. The peak-to-peak voltage on the force sensor is read form the oscilloscope, and converted into a peak force value (or force amplitude). The measured force is constant, but is showing significant and periodic deviations. The period of these deviations match the coil pitch (τ_c = 3.5 [mm]). The mean value of the force characteristic is 1.1 [N] and the force variation in this figure has a magnitude of 0.06 [N]. This means that the force variation is approximately 5.5 % of the mean force value.
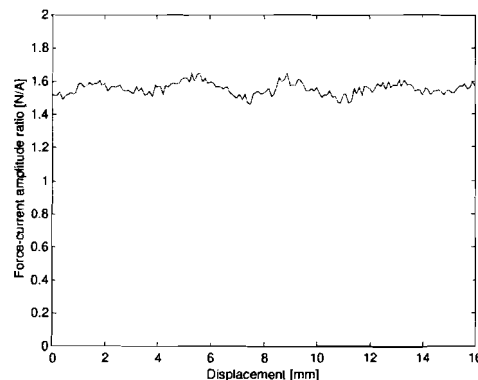
Figure 5.12: Force-current amplitude ratio as function of the displacement

In figure 5.12, the measurements of figure 5.10 and 5.11 are merged into one characteristic. This figure shows the amplitude of the force that is produced divided by the RMS value of the current. The mean value of this ratio is 1.55 $[NA^{-1}]$. The variations in this characteristic have an magnitude of 0.1 $[NA^{-1}]$. This is 6.5 % of the mean value. From this measurement result, the force constant (k_F) can be calculated.

$$k_F = \frac{F}{\hat{i}}$$ (5.1)

In this case, the measured k_F is equal to 1.1 $[NA^{-1}]$. According to (2.23) however, the calculated value of k_F is 2.55.

5.4 Thermal measurements

In figure 5.13, the temperature rise in the stator of the tubular linear actuator is shown as a function of the time. A constant power of 2, 4 and 6 $[W]$, respectively is dissipated in the stator. This power is created by a DC current that is varied in time to keep the power constant. The power that is dissipated is equally distributed over the three phases. Therefore, the three phases are connected in series. The temperature is measured by a thermocouple in the middle of the stator. This is the place where the permanent magnetic material is located. The temperature of the magnetic material must be kept low, to keep the magnets from demagnetisation. A temperature dependent demagnetisation curve of the permanent magnetic material that is used in the test set-up, is shown in appendix B.2, figure B.3.
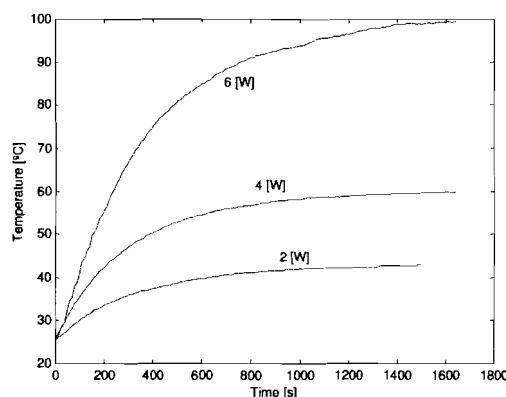
Figure 5.13: Thermal measurement results

Figure 5.13 shows that for a total dissipated power of 4 $[W]$ the temperature within the stator rises up to 60 $[°C]$. From figure B.3 can be derived that this should not give any problems with demagnetising the magnets, since the knee-point of the demagnetisation curve is below the horizontal axis for temperatures up to 80 $[°C]$. From figure 3.13 can be derived that for an inner rod radius of 1.6 $[mm]$, the magnet flux (ϕ_{mag}) is approximately 5.8 10^{-5} $[Vs]$. This means that the operation point of the magnet is located at a flux density value (B_{op}) of:

$$B_{op} = \frac{\phi_{mag}}{A_{mag}} = \frac{\phi_{mag}}{\pi\left(r_4^2 - r_2^2\right)}$$ (5.2)

With the sizes of table B.1, B_{op} is approximately 0.82 $[T]$. Demagnetisation due to a drop of the operation point below the knee-point is not even present at 110 $[°C]$ for this operation point, according to figure B.3. However, due tot the temperature rise in the actuator, the remanence of the magnet drops. The operation point is therefore lower than calculated with (5.2).

Allowing the coils to reach temperatures up to 100 $[°C]$, could result in failures within the windings, like short-circuits. Because delicate parts must be handled with the nozzle, the temperature of the tubular actuator is not allowed to rise too much. 60 $[°C]$ is in that case already a high value. To what

extend the heat produced in the linear motor contributes to a temperature rise in the nozzle, is dependent on the total configuration. It can therefore only be estimated, when the total actuation system is designed.

5.5 Measurement and modelling comparison

The results of the measurements can be compared with the results of the FEM model of chapter 4. In the first paragraph, the EMF waveforms are compared. In the second paragraph, the force characteristics are compared. The force constant (k_f) that is found with FEM is compared with the measured force constant.

5.5.1 EMF

The EMF waveforms modelled with FEM (figures 4.4 to 4.7) are compared with the measured waveforms (figures 5.5 to 5.8). The EMF waveforms that are measured have a slightly lower magnitude than the EMF waveforms of the FEM model. The shape of the measured waveforms is equivalent to that of the modelled waveforms. This is confirmed by the figures showing the harmonic components of the different configurations. The amplitude of the harmonics is a bit smaller for the measured EMF waveforms, but the harmonics components are proportional.

5.5.2 Force characteristic

In the measured force characteristic (figure 5.12) a force variation is visible with a frequency that is equal to the pole pitch (τ_p). In the FEM model, hardly any position dependency can be found for the force. The magnitude of the force is 3.3 [N] for the FEM model at a current density of 6.0 $[Amm^{-2}]$. The area of the coils (A_c) is 7.1 $[mm^2]$, so the total number of ampere turns in the FEM model is 42.6 [A]. For a coil configuration with 39 turns per coil (as in the test set-up), this would mean a current of 1.1 [A]. Now the force magnitude of the FEM model can be compared with the magnitude of the measurements. In the FEM model the force per (virtual) ampere is (3.3/1.1 =) 3.0 $[NA^{-1}]$. In the measurement, this ratio is 1.1 $[NA^{-1}]$.

5.5.3 Conclusion

In section 4.5, it was shown that there is a significant difference between the results of MEC and FEM. The magnitude of the forces calculated with MEC is approximately 0.8 times the magnitude of the forces calculated with FEM. This is a significant difference, but present in all simulations. The results of the EMF estimation of the FEM model and the measurements differ by a factor 1.04. The force constants determined by FEM and by the measurements however differ by a factor 2. From this, it can be concluded that most likely an error has been made in the force measurement. This error could be caused by a misalignment of the force sensor and the tubular motor mover. Because of this misalignment, a large amount of friction is present in the measurement system. This friction influences the force measurement. Another possibility is that the magnets are demagnetised by the high stator temperature. A third possibility is that the averaging carried out by the oscilloscope results in a lower force value. Inconsistent triggering might cause this effect. However, both signals (current and force) are triggered on the current signal. The inconsistent triggering should then effect both the current and the force. As discussed before, there is no good relation between a single measured current and the force measured at the same time. Therefore, the triggering might influence the measurement. That the difference between the FEM and measurement result is exactly a factor 2 could also indicate that a mistake has been made in the reading and conversion of the force measurement results from the oscilloscope.

6 Design flow

The goal of the project is to create a module that accommodates two z-theta actuation systems in the same dimensions in which currently one z-theta actuation system is placed. A z-theta actuation system consists of: actuator(s), encoder(s), bearings and a vacuum system. These parts of the system can be separately designed for the rotary and linear part of the system, but a combination of both degrees-of-freedom into one system can be beneficial. For instance, a linear encoder and a rotary encoder both occupy space in the z-theta module. When both encoders are combined into one encoder system, precious space can be saved. This space becomes available to other parts of the actuation system.

Section 6.1 treats the design process of the z-theta actuation system. The actuation system consists of several parts. One of these parts is the linear actuator. The design process of the actuation system is started in this report by designing the linear actuator. The design process of the linear actuator is treated in section 6.2. In section 6.3 the dimensioning of the coils in the linear actuator is treated. After the design process is completed and the coils are dimensioned, the final linear actuator design is presented in section 6.4.

6.1 General design

The design process of the z-theta actuation system consists of several steps. Step 1 in this process is the definition of the task. The goal and requirements of the design task have to be specified. After these elements are set, an inventory is made of the constraints that are created by setting the goal and requirements. Next, a strategy is set to come to an optimal actuation system. The design process is only partially completed, so no optimal actuation system is derived. However, the optimisation process of one part of the actuation system is shown in section 6.2.

6.1.1 General design goal

In this case, the task definition is relatively simple. The z-theta actuation system that has to be designed must meet the following requirements:
1) It must have an equivalent or even better performance than the current system,
2) It must have a higher bandwidth than the current system,
3) It must be small, so it can be placed twice in the dimensions of the current system,
4) It must be compatible with the current pick-and-place machines.

The first goal is the most difficult one. The word performance in this requirement can be interpreted in multiple ways. In this case, performance must be interpreted in terms of pick-and-place actions. The number of pick-and-place actions that can be reached with the designed actuation system, must minimally be equal to the number of pick-and-place actions that can be reached with the current system. The fact that two actuation systems can be placed in one z-theta module causes a significant gain in pick-and-place actions per hour. The number of pick-and-place actions that can be reached is mainly dependent on the system configuration itself. This is because the load of the actuation system (the SMD parts) is so small that it does not influence the total mass of the actuation system. More information over the pick-and-place machines can be found in chapter 1. The information concerning the current z-theta module is available in section 1.4.

6.1.2 General design constraints

Since the z-theta actuation system will be used with the current pick-and-place machines, the actuation system must be compatible with these machines. This constraint can be divided in several parts. The first and most important part is that the shape and dimensions of the z-theta module has to remain the same. This makes it possible to place the module on the current pick-and-place machines with minor modifications. The (place and shape of the) connectors, that connect the module to the rest of the machine, are not changed. A second part of the compatibility constraint is that the actuation system is designed in such a way that the electrical sources that are present in the current machines can be used for the excitation of the actuators in the system.

6.1.3 Strategy

After the goal, requirements and constraints are estimated, a literature study is started to make an inventory of implementations that meet the demands. Roughly, these implementations can be divided into three concept groups. These groups have been treated in section 1.5. Based on the literature, the most promising concept is chosen and investigated more extensively. Another concept must be chosen, when during the investigation the chosen concept appears not to be able to satisfy the demands.

The most promising actuation system concept is in this case the combined actuator concept. This concept consists of two separate actuators, one for the linear motion and one for the rotation. This splits the requirements of the total actuation system into two parts. The total actuation system must be able to perform according to the requirements, but the available volume is divided over two actuators. First, the linear actuator is studied. The implementation of a rotary actuator is however kept in mind. This report is in first place an investigation of a possible implementation of a linear actuator. This actuator is designed in such a way that it will be able to work together with a rotation actuator. Whether the requirements of the total actuation system can be met, can only be estimated. This depends on the design of the rest of the parts in the actuation system. The flowchart of the design process of the linear tubular actuator is shown in figure 6.1. This design process can also be used for the design of the rotary machine.
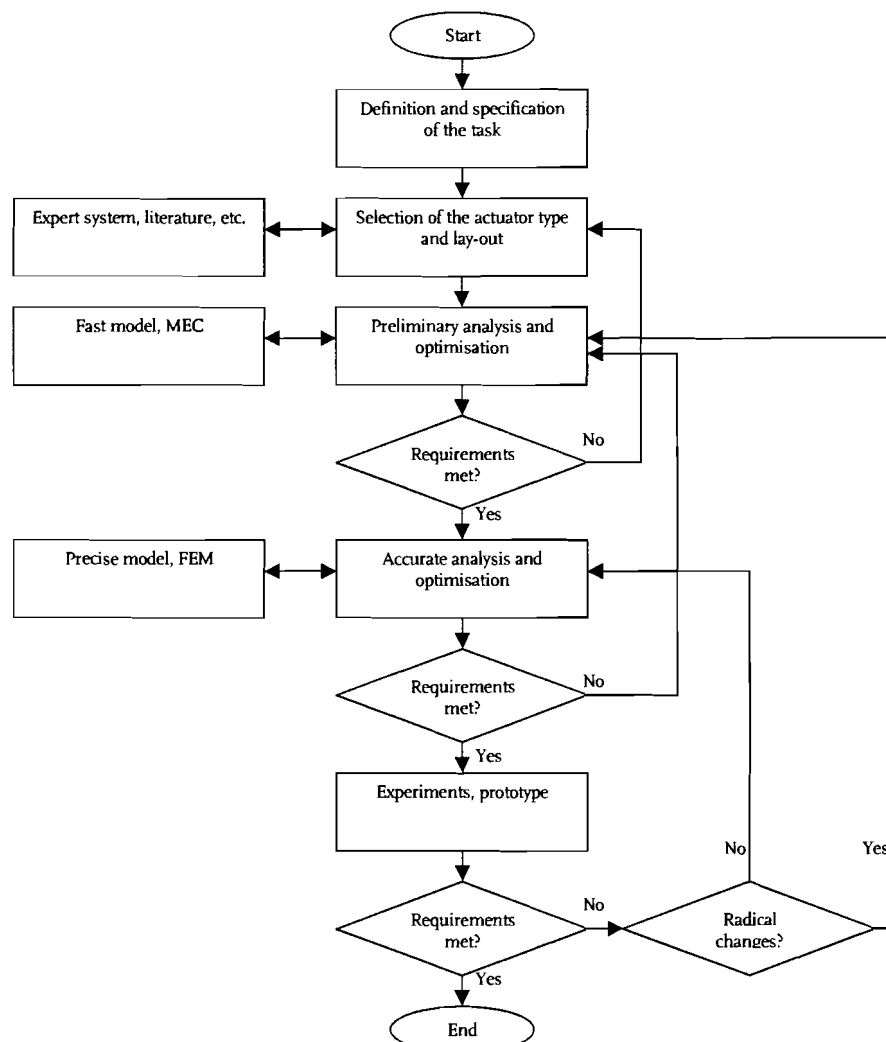
Figure 6.1: Flowchart of the linear tubular actuator design process
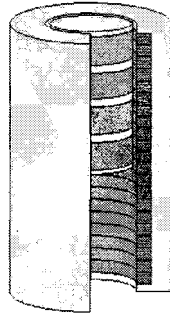
Figure 6.2: Impression of the tubular actuator

6.2 Linear tubular actuator design

The volume that was expected to be available for a linear actuator resulted in the choice for a tubular linear actuator. An impression of a tubular actuator is shown in figure 6.2. After the global geometry of the linear tubular actuator is determined, the design is optimised to meet the (expected) specifications as good as possible. This section describes the steps that need to be taken to accomplish the optimal linear tubular actuator design. In this section, the design (and optimisation) process of the linear tubular actuator is illustrated. How the models of chapter 3 and 4 fit in this process is explained. The flowchart of the design process of the linear tubular actuator is shown in figure 6.1.

6.2.1 Estimated tubular actuator requirements

As described in section 6.1, the goal is to design a linear actuation system that will be used in a pick-and-place machine. The movement interval of the linear z-actuator is just one of the elements in the duty cycle. By limiting the time needed for the linear motion, the total duty cycle time can be reduced. The way to get to a faster linear movement is a higher movement velocity. The movement velocity however is merely limited by the frequency and the voltage of the electrical sources. The frequency of the electrical source is not a limitation in the range it is needed here (< 10 [Hz]). The stator coils can be designed in such a way that the voltage of the electrical source is more than sufficient. However, still the velocity is limited.

This is caused by the fact that increasing (acceleration) and decreasing (deceleration) the velocity is also present in the duty cycle. The maximal speed that is reached is now dependent on acceleration (and deceleration). When the acceleration time is too long, the actuator will not be able to reach the maximum velocity. The study for limiting the time needed for a linear z-stroke is now transformed in a study for increasing the acceleration in the actuation system.

The equation that describes the relation of the force [N] produced by the actuator (F) and the acceleration [ms^{-2}] of the mover (a_m) is:

$$F = m_m a_m \tag{6.1}$$

In this equation, m_m is the total mass that needs to be moved. Incorporated in this mass is the mass of the mover of the linear tubular actuator itself. However, more elements in the actuation system need to be moved. The mass of these elements has to be added to m_m. Some parts of the sensor system for instance have to be placed on the mover. Since the total mass that needs to be moved by the actuator is not known at this stage (it can only be predicted) it is difficult to estimate a maximum acceleration. It is also hard to predict what percentage of the total mass will be taken by the mass of the linear tubular actuator mover. Therefore, not the acceleration but the force that is produced by the actuator is investigated.

Only when the mover radius changes, there is a significant change in the mass of the mover of the tubular actuator. Since the mass density of iron (7400 $[kgm^{-3}]$) and the mass density of permanent magnet material (7350 $[kgm^{-3}]$) are nearly the same, the magnet-pitch (τ_m) to pole-pitch (τ_p) ratio, hardly influences the tubular actuator mover mass.

Paragraphs 4.1.2 and 5.2.2 show that a high force output can be obtained with a configuration that also shows high force variations as function of the mover position. Though the mean value of the force is higher than the value obtained with a different configuration, the force variations could result in the preference for an option with a flat force characteristic. Force variations can to some extent be compensated by the control firmware, but this has consequences for the system. The nominal exciting current for instance can get lower, because a higher peak current value is needed for force variation compensation.

6.2.2 Estimated tubular actuator constraints

Since the linear tubular actuator will be placed twice within the current z-theta housing, some restrictions in the dimensions of the actuator originate. In chapter 2, it was indicated that the actuators must be placed next to each other in x-direction to enable a good backward compatibility with the different feeders. The restriction for the total diameter of the actuator (D_{act}) is therefore:

$$D_{act} \leq 16 \ [mm] \tag{6.2}$$

Placing the z actuator and theta actuator on the same axis can benefit the bandwidth of the system. The axial length of the theta actuator however is not clear. Besides that, there is also space needed for a vacuum system, a sensor system and bearings. Therefore, it is not possible to estimate a maximal length of the tubular actuator (in z-direction). That there is a limit to this length is clear.

The force produced by an (tubular) actuator shows less force variations for a multi-phase (≥ 2 phases) electrical system. Because there are several one-phase and three-phase electrical sources available within the pick-and-place machine configuration, one of the three-phase sources is chosen as the source for the tubular actuator. The specifications of this source are listed in appendix C.2. The most important specifications are:

$$n_{ph} = 3 \tag{6.3}$$
$$\hat{i}_{max} = 2.5 \ [A] \ (= 1.8 \ [A] \ RMS) \tag{6.4}$$
$$V_{DC,s} = 46 \ [V] \ (\pm 4 \ [V]) \tag{6.5}$$

Where n_{ph} is the number of phases, $\hat{i}_{max}$ is the peak current of the source and $V_{DC,s}$ is the DC supply voltage.

6.2.3 Tubular actuator strategy

After the type of actuator is selected and the initial dimensions of the actuator are estimated, preliminary calculations can give an indication of the performance of the actuator. In order to achieve the optimal actuator performance some parameters have to be fine-tuned. These parameters are:

- The mover radius,
- The pole pitch and magnet pitch,
- The radius of the inner rod,
- The thickness of the outer iron,
- The number of turns per coil.

In the parametrical search, the different parameters are dependent on each other. Changing one parameter changes the magnetic circuit in the structure. This can have as result that the maximum of another parameter changes to another value. It is therefore impossible to estimate the optimal configuration with looking at the different parametric variables only once. Some iterations are needed to find an optimal configuration. As an example, the variables radius 4 (r_4) and radius 6 (r_6) are chosen; r_4 is the outer radius of the mover $[mm]$ and r_6 is the inner radius of the outer iron $[mm]$. In between the radii, the airgap and the copper windings are located. Therefore, radius 6 is always at least 0.5 $[mm]$ larger than radius 4 $(r_6 > r_4 + 0.5)$. When the mover radius (r_4) changes, the maximum force produced by the actuator shifts to another value of r_6.

6.2.4 Tools

For the optimisation, several tools are used. The first steps in the optimisation process are made with the MEC model described in chapter 3. The MEC model is a program written in Matlab. This program calculates the force output of the actuator as function of the tubular actuator configuration. The force is calculated by a Lorentz volume integral (3.13). The configuration is changed by varying the dimensions of the structure. The calculation is an iterative process because of the saturation that occurs in the different flux paths. Only when all reluctances of the flux tubes are stably converged, a solution can be found. The calculation is carried out in a fraction of a second, so the program is able to calculate numerous set-ups (> 100) within a couple of minutes. The different input parameters are stored in the input table. The corresponding output results are stored in the output table. When investigating the magnet and iron ring length for instance, not only the force is calculated but also a force density (force divided by the sum of the magnet and iron ring length) is calculated. The input parameters are shown in table 3.1. In most cases, the output table contains at least these output results:
- Flux in the different paths in the structure,
- Flux density in different flux tubes in the structure,
- Mass of the mover of the tubular actuator,
- Force and acceleration produced by the actuator, or force per meter of actuator length,
- Electrical loading,
- The number of iterations needed to calculate the set-up.

In some cases, extra output results are added to the output table. All the output results listed above can be used in the process of finding the optimal configuration. The last parameter (number of iterations) is stored in the output table because there is a maximum for the number of iterations set at the input. This prevents the program from infinitely long calculations for solutions that do not converge. A check bit warns the output for a non-converged solution. Fortunately, this error table stays empty for most calculations and the solution converges in 20 to 25 iterations.

After a rough estimation of the optimal solution is calculated with the MEC model, a second modelling method (FEM) is used to refine the results of the MEC model. This method, discussed in chapter 4, is a more accurate method but also a more time-consuming method. Another advantage of FEM over MEC is that the FEM model is able to calculate the force as function of the displacement while this is not incorporated in the MEC model. This way the force variations as function of the displacement can be estimated. With FEM, it is also possible to estimate the EMF waveform, which is a different method of studying the force variation. A more sinusoidal EMF will result in less force variation.

The biggest advantage of the FEM model over the MEC model is that the FEM model makes a calculation over the total structure while MEC only calculates one segment. Therefore, FEM is able to give an estimation of end effects. These end effect occur at both mover ends, and are especially present (disturbing the general force characteristic) when the mover reaches one of the stator ends, as shown in section 4.4. Because FEM calculates the force by a change in magnetic (co)energy (virtual work), it is able to calculate the end effects. By this way of force calculation, FEM is able to calculate cogging and reluctance forces. The reluctance force is caused by the iron rings (placed between the magnets) that are retracted into the coils when the coils are excited. The reluctance force is significantly smaller than the force calculated with the Lorentz method (< 0.5 %). Cogging force occurs when the mover reaches one end of the stator. The magnetic field of the mover pushes the mover to the centre of the stator. Cogging force is a significant part of the total force and therefore brings significant differences in the two calculation methods (Lorentz method for MEC and the virtual work method for FEM).

6.2.5 Results

The highest force output of the tubular actuator with an outer radius of 8 [mm] is obtained for a structure where there is no inner rod in the design and the outer iron has a thickness of 0.4 [mm]. This configuration is the electromagnetic optimum for the actuator. This does not imply that this is the practical optimum of the actuator, since mechanical aspects are not considered in this study. To

ensure enough (mechanical) mover stiffness (and a cheap mover production process) an inner rod has to be present in the design. This inner rod has to be rigid, to add stability to the mover. The inner rod also forms the connection of the mover to the other parts in the actuation system (as bearings and the nozzle). The outer iron on the stator also has to be rigid, to provide a stable connection for the actuator to the outer world.

The highest force output occurs when the iron rings, that separate the magnets, have a minimal length $(\tau_p - \tau_m)$ without having too much saturation in the iron rings (1 to 2 [mm]). It is hard to indicate where this point is exactly located, because the iron rings form a corner for the flux paths. The flux lines enter the rings axially and leave the rings radially. Therefore, there is some local saturation, but this does not decrease the airgap flux significantly. According to [8], the force produced is maximal when τ_m/τ_p is approximately 0.85. The highest force output however comes with a drawback. The radial flux distribution in the airgap is far from sinusoidal. Therefore, the amount of force variation as function of the mover displacement is high. The normalised force variation (the force variation divided by the mean value of the force) has a minimum when τ_m/τ_p is approximately 0.6 to 0.7.

The mover radius at which the force produced by the actuator reaches a maximum is located between 4.8 and 6.5 [mm]. This is mainly dependent on the thickness of the outer iron. For a thin outer iron, the optimal mover radius is larger than for a thick outer iron. For the (electromagnetic) optimal outer iron thickness of 0.4 [mm], the optimal mover radius is 6.3 [mm].

6.3 Coil dimensioning

6.3.1 Number of turns

After the optimisation process is completed, the volume in which the coils must be placed is determined. For the test set-up, the coils are designed to match an electrical source that is already available. The specifications of this source are in appendix C.2. The way of winding is orthocyclic. This winding lay-out is chosen because the fill factor of the strands for orthocyclic windings is relatively high compared with the fill factor of straight (scramble) wound coils. A disadvantage of orthocyclic windings is that the place where the turns shift to another position is constant. From this effect, a swelling of the coil originates at this position. The coils are therefore not completely round. Pressing the coils in a mould can solve this problem. This is however too complex and too expensive when building a test set-up.

When the dimensions of the coil are set and the specification of the electrical source is known, the number of turns can be calculated using the voltage equation:

$$V = R_w I + \frac{d\phi}{dt} = R_w I + n_{atw} \frac{d\phi_{turn}}{dx} v_m \tag{6.6}$$

where V is the supply voltage [V], R_w is the resistance of a winding [Ω], I is the winding current [A], ϕ is the flux caught by a winding, n_{atw} is the number of turns per winding that catch the changing flux [ ], ϕ_{turn} is the flux that is caught by a single turn [Vs] and v_m is the speed of the mover [ms^{-1}]. The number of turns per winding that catch the flux is not equal to the total number of turns. This is only half of the total number of turns, since the stator length is twice the length of the mover:

$$n_{atw} = \tfrac{1}{2} n_{cw} n_{tc} \tag{6.7}$$

where n_{cw} is the number of coils per winding (is equal to 8 [ ] in the selected configuration), n_{tc} is the number of turns per coil [ ]. The induced EMF per turn (e_t [V]) is:

$$e_t = -\frac{d\phi_{turn}}{dx} v_m = \frac{e}{n_{atw}} \tag{6.8}$$

where e is the total EMF [V]. By FEM calculations, it is estimated that at the (maximum) speed of 0.1 [ms^{-1}], the induced EMF per turn (e_t) is approximately $0.65 \cdot 10^{-3}$ [V].

The resistance of a winding (R_w) is equal to:

$$R_w = n_{cw} n_{tc} \frac{\rho_{copper} l_{tm}}{A_t} = n_{cw} n_{tc}^2 \frac{\rho_{copper} \pi D_{cm}}{k_f A_c} \qquad (6.9)$$

where ρ_{copper} is the resistivity of copper (= 1.7 10^{-8} [Ωm]), l_{tm} is the mean length of a turn [m], and A_t is the copper area of a turn [m^2]. D_{cm} is the mean diameter of a coil [m], k_f is the fill factor of the orthocyclic wound coils (with an estimated value of 0.7 [ ]) and A_c is the area of the coil [m^2]. The area per coil is determined by the dimensions of the configuration. The maximum number of turns can be calculated with (6.6) to (6.9). Based on the electric properties of the coils and the used electrical source, the maximum number of turns is approximately 250, when using the coil dimensions of the test set-up (table 5.1).

6.3.2 Thermal restrictions

In the previous paragraph, the maximum number of turns per coils is estimated. This maximum is calculated from the specifications of the electrical source. However, another factor limits the number of turns or the current through them. (6.6) consists of two parts, one for the resistive character of the windings (RI) and one for the EMF ($d\phi/dt$). The resistive character of the windings causes electrical energy to be converted into heat. When too much heat is produced, the temperature of the actuator rises drastically. This effect is unwanted because of two reasons. The first reason is that the heat of the actuator is transferred to the surroundings of the actuator. In the surroundings of the actuator is the nozzle and attached to the nozzle are the SMD parts. The SMD parts however can be delicate parts that can be destroyed by (sudden) temperature rises. The second reason is that the magnet characteristic is temperature dependent (figure 2.4). Especially the knee point of the characteristic is shifted to a higher B-value and lower H-value for a higher temperature. When the operation point of the magnet drops below the knee point, the magnet will lose its magnetisation irreversibly.

The temperature rise of the actuator not only depends on the heat produced in the actuator, but also on the ability of the actuator to lose heat to the surroundings. This is dependent on the configuration and can be estimated by means of FEM. The estimation process is treated in section 4.2. With this model, an estimation can be made of the power [W] that can be dissipated in the tubular actuator stator, without overheating the actuator. The total power that is dissipated is equally distributed over the three phase windings. The hysteresis losses are considered negligible, because the frequency of the applied currents is low. This frequency is a function of the mover speed (v_m) and the pole pitch (τ_p):

$$f = \frac{v_m}{2\tau_p} \qquad (6.10)$$

The frequency of the applied currents is maximally 5 [Hz] when the maximal mover velocity is 0.1 [ms^{-1}]. At such low frequencies, hysteresis losses are minimal. Because the copper losses are dominant, a maximum dissipation per winding can be estimated with FEM. When the current (I [A]) through the phase windings is known, a maximum number of turns per coil can be estimated with (6.8) and with the maximum dissipated power per winding (P_{win} [W]):

$$P_{win} = \frac{1}{3} P_{elec} = I^2 R_{win} \qquad (6.11)$$

where P_{elec} is the total dissipated power over three windings. For a maximum total power dissipation of 4 [W] and a continues current of 1.0 [A] the maximum number of turns per coil is approximately 45, when using the coil dimensions of the test set-up (table 5.1).

The duty cycle is also important when investigating the thermal behaviour. When the peak force (and peak current) is not constantly required, the heat production in the actuator can be temporarily higher than the (constant heat production) limit, without reaching a temperature that can damage the actuator or the SMD components. Dynamics of the temperature changes have to be investigated in this case.

6.4 Final tubular actuator design

The initial design of the tubular actuator is optimised for the (statically) produced force. The number of turns per coil is adapted to fit the specifications of the amplifier. The results of the optimisation process are shown in table 6.1. The length of the magnets (l_{mag}) and iron rings (l_{ir}) are chosen in such a ratio that the force density of the actuator is as high as possible while still providing a rather sinusoidal EMF. The force density can be increased by choosing a higher l_{mag} (8 [mm]) and a lower l_{ir} (2 [mm]), but this is at the cost of a non-sinusoidal EMF.

Table 6.1: Optimisation results

Parameter	Description	Value [*unit*]
r_2	Outer radius of inner rod	0.0 [mm]
r_4	Outer radius of the mover	4.8 [mm]
r_5	Inner radius of the stator (= inner radius of electric loading)	$r_4 + 0.5 = 5.3$ [mm]
r_6	Inner radius of outer tube (= outer radius of electric loading)	7.6 [mm]
r_8	Outer radius of outer tube (= total diameter)	8.0 [mm]
τ_m (= l_{mag})	Magnet pitch (= Length of the magnet)	6.5 [mm]
l_{ir}	Length of the iron rings (= τ_p - τ_m)	4.0 [mm]
τ_p (=L)	Pole pitch (= Total length (= l_{mag} + l_{ir}))	10.5 [mm]
τ_c	Coil pitch (= $\tau_p/3$)	3.5 [mm]
n_{ic}	Number of turns per coil (for the selected electrical source (6.3) to (6.5))	30 - 45 [ ]

When an inner rod is placed in the mover, a path is created for leakage flux through the inner rod and permanent magnetic material is removed for the inner rod. Both effects cause a lower flux in the outer iron and therefore a lower force production in the actuator. However, when the inner rod has a small radius (r_2) and a low permeability material is used for this rod, the influence of the inner rod is minimal as shown in the paragraphs 3.3.3 and 4.3.3. As shown in paragraph 3.3.3, the presence of an inner rod can even be helpful for increasing the operation point of the permanent magnets.

For the inner radius of the outer iron tube, 7.6 [mm] is chosen. The outer radius of the outer iron is 8.0 [mm]. This makes the outer iron rather thin (0.4 [mm]). The optimisation is carried out for the magnetic circuit and not for mechanical aspects of the actuator. The thin outer iron can result in insufficient (mechanical) stator stiffness. A mechanical study is not in the scope of this M.Sc. project.

7 Conclusion and recommendations

7.1 Conclusions

- The idea of using a tubular linear actuator comes from a literature study. The expectation is that a tubular linear actuator can be combined with a rotary actuator in a smart way. This would save precious space and increase the mechanical bandwidth.

- An initial calculation is carried out, to estimate the force that can be produced by a tubular actuator, within an expected limited volume.

- An analytical model (MEC) of a segment of the linear tubular actuator is made. Saturation of iron is calculated iteratively in this model. The MEC model is used for a preliminary optimisation of the actuator.

- The accuracy of the MEC model is low. The shape of the characteristics after the optimisation process with MEC corresponds to the shape of the characteristics found with FEM. The magnitude of the force found with both methods however differs up to 20 %.

- A FEM model of the linear tubular actuator is made in Ansoft Maxwell 2D, version 9 and 10. With FEM, the (optimisation carried out with the) MEC model is checked and the performance of the actuator is analysed.

- A test set-up is realised. With this set-up, the EMF of the actuator is measured and the force produced by the actuator is measured as a function of the mover displacement.

- The EMF predicted by FEM is nearly identical to the measured EMF. There is a significant difference in the predicted (FEM) and measured force constant. The cause of this difference is not clear.

- An initial thermal study shows that thermal issues are critical in the tubular actuator design in this report. Demagnetisation of the permanent magnets can be a problem.

7.2 Recommendations

- In this report, the optimisation of the tubular linear actuator is based on a magnetostatic approach. For further optimisation of the tubular actuator, measurements of the dynamics and FEM transient analysis can be used.

- After the linear actuator is designed, the actuation system is completed with a rotary actuator. This is not a straightforward process. This process will require modifications of the tubular actuator configuration.

- A smart combination of the linear tubular actuator and a rotary actuator can be beneficial for minimisation of the actuation system. This combination can influence the requirements and the performance of both parts. How the parts can be combined optimally must be studied further.

- The measurements carried out on the test set-up showed a good correspondence to the results of FEM for the EMF estimation. For the force measurement however, the results differ a lot from the results of FEM. The cause of the difference has to be investigated. As probable

causes, friction in the test set-up and demagnetisation of the magnets (by overheating) can be presented.

- This report covers an electromagnetic study toward the linear tubular actuator. For an optimal configuration, mechanical aspects also have to be considered.

- In section 4.4, a Halbach configuration is introduced as a possible improvement for the actuator performance. To what extent a Halbach configuration is an improvement and the (economical and parametrical) consequences of a Halbach configuration require a further study.

- In this report, a tubular actuator configuration is chosen with a long stator and short mover. The advantage of this configuration is that there is no cogging for most of the mover position interval (only when the mover reaches the end of the stator). A disadvantage of this configuration is a higher copper loss, due to windings that are excited but do not contribute to the force production. When copper losses are an issue, a different configuration with short stator and long mover can be considered.

References

[1]   US patent # 5789830: "In-Line Rotational Drive."

[2]   J.F. Gieras and M. Wing, "Permanent Magnet Motor Technology", second edition, Marcel Dekker, Inc., 2002, New York, ISBN 0824707397.

[3]   A.E. Fitzgerald and C Kingsley, S.D. Umans, "Electric Machinery", sixth edition, Mc Graw Hill, New York, ISBN 0073660094.

[4]   J. Wang and D. Howe, G.W. Jewell, "Analysis and Desigh Optimization of an Improved Axially Magnetized Tubular Permanetn-Magnet Machine", IEEE Transactions on Energy Conversion, vol. 19, no. 2, June 2004, pages 289 – 295.

[5]   J. Wang and G.W. Jewell, D. Howe, "A General Framework for the Analysis and Design of Tubular Linear Permanent Magnet Machines", IEEE Transactions on Magnetics, vol. 35, no. 3, May 1999, pages 1986 – 2000.

[6]   N. Bianchi and S. Bolognani, F. Tonel, "Design Criteria of a Tubular Linear IPM Motor", IEEE Electrical Machines and Drives Conference (IEMDC) 2001, pages 1 – 7.

[7]   J. Wang and D. Howe, "Analysis of axially magnetized, iron-cored, tubular permanent magnet machines", IEE Proceedings on Power Applications, vol. 151, no.2, March 2004, pages 144 - 150.

[8]   J. Wang and D. Howe, G.W. Jewell, "Analysis and Design of an Improved Axially Magnetised Tubular Permanent Magnet Machine Topology", IEEE Transactions on Energy Conversion, vol. 19, no. 2, June 2004, pages 289 – 295.

[9]   V. Ostovic, "Dynamics of Saturated Electric Machines", Springer-Verlag, New York, ISBN 0387970797.

[10]   J.R. Hendershot Jr. and T.J.E. Miller, "Design of Brushless Permanent-Magnet Motors", First Edition, Magna Physics Publications, 1994, ISBN 1881855031.

[11]   Birch, Lecture notes, University of Sheffield.

[12]   R. Remsburg, "Thermal Design of Electronic Equipment", CRC Press, 2001, ISBN 0849300827.

[13]   J.E. Sergent and A. Krum, "Thermal Management Handbook for Electronic Assemblies", McGraw-Hill, 1998, ISBN 0070266999.

Appendix A

A.1 MEC model procedures

A.1.1 Procedure of the MEC function

This procedure creates an input table with configuration variables. The function uses the function Satcal (A.1.2) to calculate the output parameters of each configuration. The output results are stored in an output table.
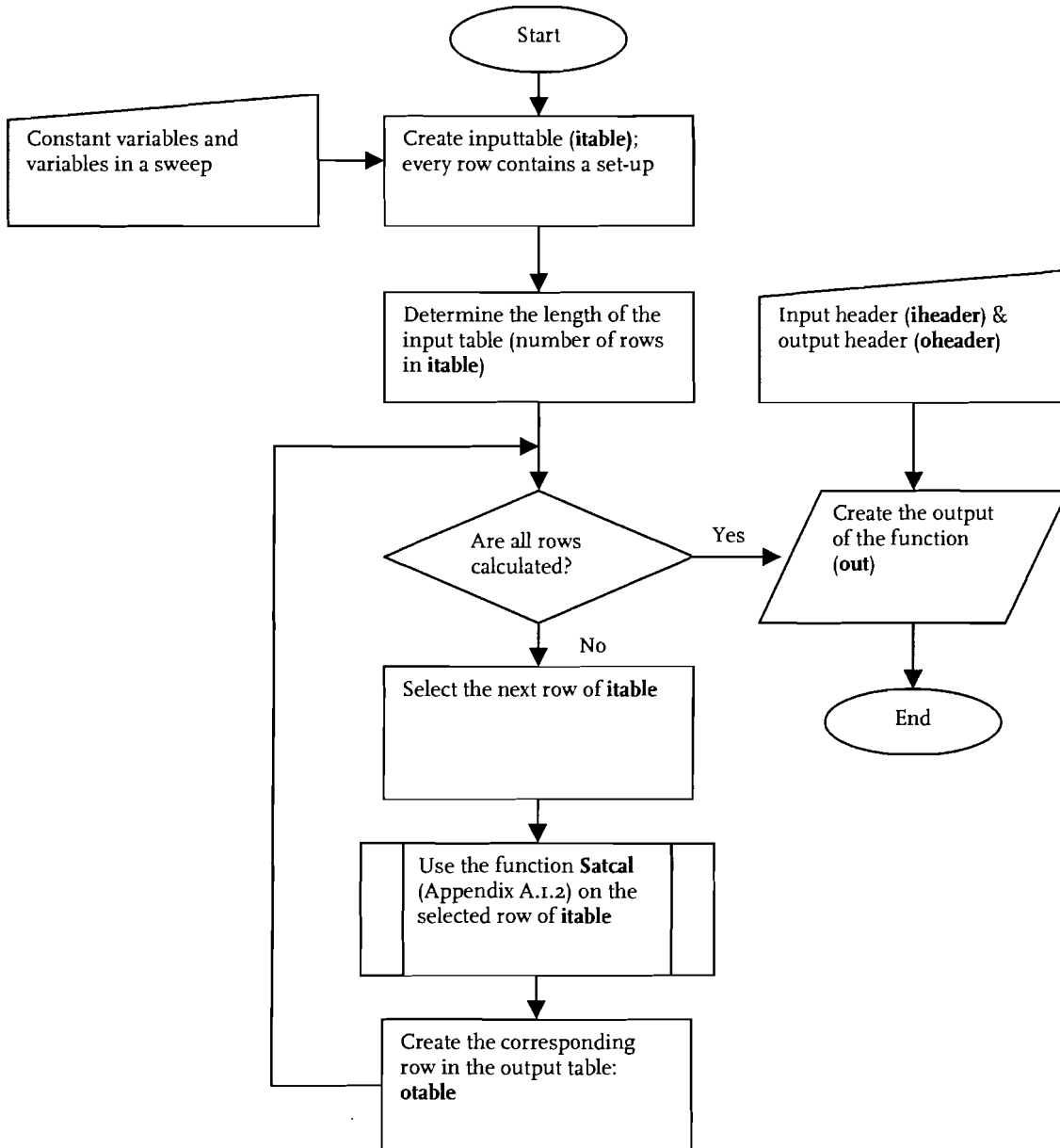
A.1.2 Procedure of the Satcal function

Start

Initial value of current relative permeability values for every flux tube: 50

Initial value of previous relative permeability values for every flux tube: 1

Set-up variables of MEC are provided when calling this function

Current value of the relative permeability of every flux tube (μ_c)

Previous value of the relative permeability of every flux tube (μ_p)

Calculate the area of the base of all flux tubes

1 iteration delay

Is $|\mu_c - \mu_p| < \varepsilon$ for all flux tubes   Yes

No

Calculate new values of relative permeability for all iron flux tubes ($\mu_{cal} = {}^1/_6 \, (\mu_c + 5\mu_p)$)

Calculate new values of relative permeability for all iron flux tubes ($\mu_{cal} = {}^1/_6 \, (\mu_c + 5\mu_p)$)

Use the function **Network** (Appendix A.1.3) with the μ_{cal} values

Use the function **Network** (Appendix A.1.3) with the μ_{cal} values

Calculate the B-field in the iron flux tubes

Calculate mass of the mover, force, acceleration and B-fields

Use the function **Bhchar*** to determine a new relative permeability value (μ_n)

Send data back to the **MEC** function (appendix A.1.1)

End

This procedure determines the saturation of soft magnetic elements in the configuration by means of an iterative calculation. The function uses the function Network (A.1.3) to calculate the reluctance network for each iteration. The Satcal function also calculates output results of the MEC model and returns these results to the MEC function (A.1.1).

*BHchar
This function is a look-up table containing the B-H characteristic of the soft magnetic iron. BHchar determines a new relative permeability value (μ_n) by means of (cubic) interpolation

A.1.3 Procedure of the Network function

```
                        ( Start )
                            │
                            ▼
            ┌───────────────────────────┐
            │ Set-up variables of MEC and│
            │ permeability values are    │
            │ provided when calling this │
            │ function                   │
            └───────────────────────────┘
                            │
                            ▼
            ┌───────────────────────────┐
            │ Calculate the reluctance of│
            │ the different flux tubes   │
            │                            │
            └───────────────────────────┘
                            │
                            ▼
┌──────────────────────┐  ┌───────────────────────────┐
│ Reluctance network   │  │ Calculate the flux over the│
│ scheme               │─▶│ different paths in the     │
│ (figure A.1)         │  │ scheme                     │
└──────────────────────┘  └───────────────────────────┘
                            │
                            ▼
                    / Send data back  /
                   / to the Satcal   /
                  / function        /
                 / (appendix A.1.2)/
                            │
                            ▼
                        ( End )
```
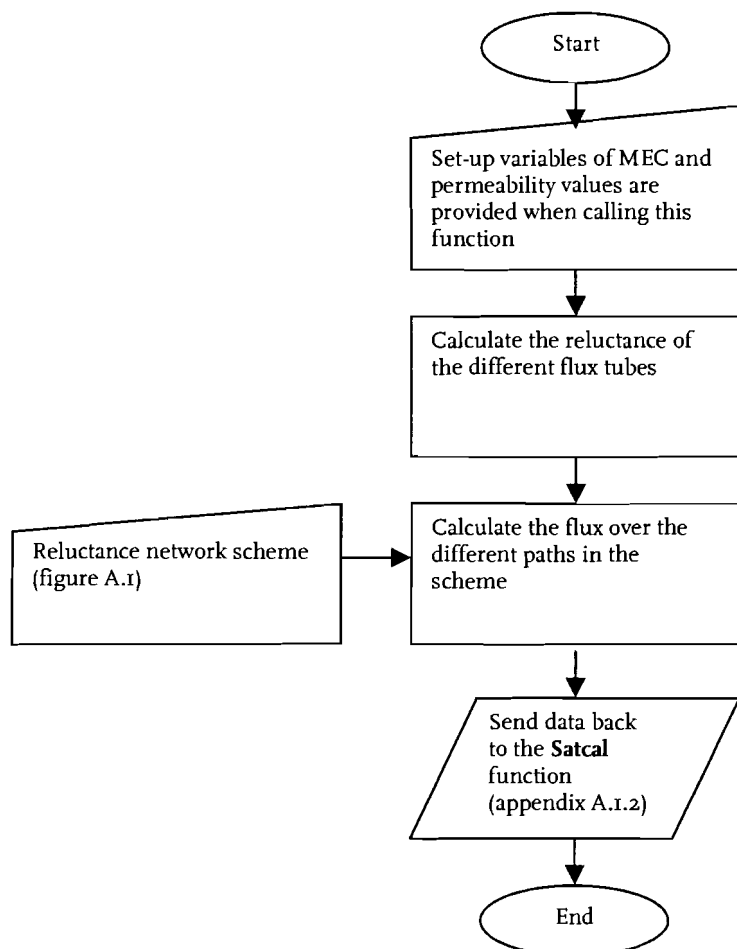
This function calculates the flux in different paths in the structure. It receives permeability values of soft magnetic elements in the structure from the Satcal function (A.1.2).
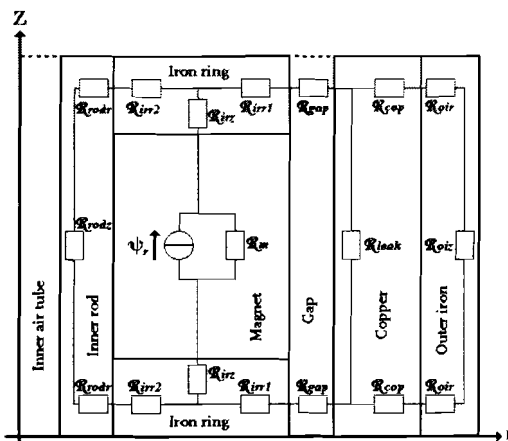
Figure A.1: MEC model reluctances
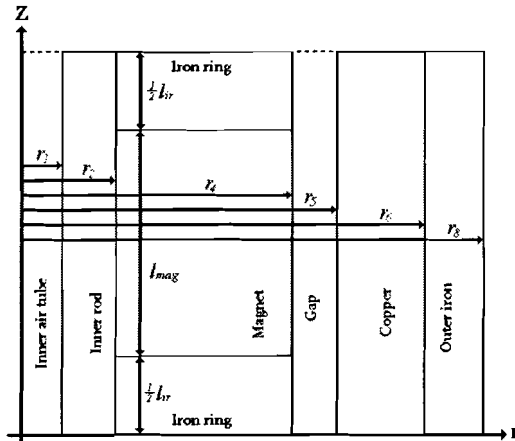
Figure A.2: MEC model variables

A.2 MEC reluctance calculation

In figures A.1 and A.2 the reluctances and variables of the MEC model are shown respectively. In table A.1 the equations are givens with which the reluctances can be calculated from the variables.

Table A.1: Reluctance calculation formulas

Parameter	Equation	Note
$\mathcal{R}_m$	$\dfrac{l_{mag}}{\mu_{mag}\pi\left(r_4^2 - r_2^2\right)}$	$\mu_{mag} = 1.05\,\mu_0$
$\mathcal{R}_{irz}$	$\dfrac{\frac{1}{4}l_{ir}}{\mu_{irz}\pi\left(r_4^2 - r_2^2\right)}$	μ_{irz} is calculated iteratively
$\mathcal{R}_{irr1}$	$\dfrac{1}{\mu_{irr1}\pi l_{ir}}\ln\left(\dfrac{2r_4}{r_2 + r_4}\right)$	μ_{irr1} is calculated iteratively
$\mathcal{R}_{irr2}$	$\dfrac{1}{\mu_{irr2}\pi l_{ir}}\ln\left(\dfrac{r_2 + r_4}{2r_2}\right)$	μ_{irr2} is calculated iteratively
$\mathcal{R}_{rodr}$	$\dfrac{1}{\mu_{rodr}\pi l_{ir}}\ln\left(\dfrac{r_2}{r_1}\right)$	μ_{rodr} is calculated iteratively
$\mathcal{R}_{rodz}$	$\dfrac{l_{mag} + \frac{1}{2}l_{ir}}{\mu_{rodz}\pi\left(r_2^2 - r_1^2\right)}$	μ_{rodz} is calculated iteratively
$\mathcal{R}_{gap}$	$\dfrac{1}{\mu_0\pi l_{ir}}\ln\left(\dfrac{r_5}{r_4}\right)$	-
$\mathcal{R}_{leak}$	$\dfrac{l_{mag} + \frac{1}{2}l_{ir}}{\mu_0\pi\left(r_6^2 - r_4^2\right)}$	-

$\mathcal{R}_{cop}$	$\dfrac{1}{\mu_0 \pi l_{ir}} \ln\left(\dfrac{r_6}{r_5}\right)$	-
$\mathcal{R}_{oir}$	$\dfrac{1}{\mu_{oir} \pi l_{ir}} \ln\left(\dfrac{r_6 + r_8}{2 r_6}\right)$	μ_{oir} is calculated iteratively
$\mathcal{R}_{oiz}$	$\dfrac{l_{mag} + \frac{1}{2} l_{ir}}{\mu_{oiz} \pi \left(r_8^2 - r_6^2\right)}$	μ_{oiz} is calculated iteratively

A.3 MEC magnetic and electric analogies

In table A.2, the analogy between magnetic fields, electrostatic fields and electric fields is shown [9]. There is one difference in the analogy between electric and magnetic fields. To maintain a certain energy level in a magnetic field, no external support is needed. In an electric field the energy is irreversibly converted into heat, therefore a source is needed to maintain a constant energy level. When all quantities in a magnetic field are constant, the energy stored in the field is constant, while under the same conditions the energy lost in an electric field increases proportional to the time.

Table A.2: Magnetic and electric analogies

	Type of Field		
	Magnetic	Electrostatic	Electric
Material constant	μ	ε	σ
Flux or current density	$\vec{B}$	$\vec{D}$	$\vec{J}$
Field strength	$\vec{H}$	$\vec{E}$	$\vec{E}$
Reluctance / Capacitance / Resistance	$R_m = \displaystyle\int_0^l \dfrac{dx}{\mu(x) A(x)} = \dfrac{n^2}{L}$	$R_{es} = \displaystyle\int_0^l \dfrac{dx}{\varepsilon(x) A(x)} = \dfrac{1}{C}$	$R_{el} = \displaystyle\int_0^l \dfrac{dx}{\sigma(x) A(x)}$
Potential difference	$MMF = \displaystyle\int_0^l H dl$	$V = \displaystyle\int_0^l E dl$	$V = \displaystyle\int_0^l E dl$
Flux / Charge / Current	$\phi = \displaystyle\int B dA = \dfrac{MMF}{R_m}$	$Q = \displaystyle\int D dA = \dfrac{V}{R_{es}} = VC$	$I = \displaystyle\int J dA = \dfrac{V}{R_{el}}$

A.4 MEC model Matlab files

In this section of the appendices, some Matlab files of the MEC model are shown. The MEC function in A.4.1. calculates several output parameters as a function of the mover radius (r_4). The MEC function uses the functions Satcal and Network for the calculation. The MEC function in A.4.1 is configured to calculate the output results for various values of r_4 (the mover radius).

A.4.1. Matlab file of the MEC function

```
%'MEC.m' is the base of a MEC model of a linear tubular motor.
%
%   MEC stands for magnetic equivalent circuit. Together with
%   the subfunctions 'satcal.m' and 'network.m', 'MEC.m' calculates
%   output parameters for various input configurations.
%
%   The linear tubular motor is a tubular motor with interior magnets.
%   The magnets are axially magnetised.
%
%   In MEC.m an input table is created ('inputtable'). In this table
%   the parametric and other input variables are stored.
%   Each row in this table represents a different set-up.
%   The different columns in the inputtable contain the variables.
%   The name of the variable that correspond to the column
%   are stored in the same column in the 'inputheader'.
%
%   MEC.m then uses the file 'satcal.m' to calculate the
%   output results for each row of the 'inputtable'.
%   The output of satcal.m is stored in the 'outputtable'.
%   Each row of the 'outputtable' corresponds to the same
%   row of inputs in the 'inputtable'. Each column contains
%   a different output. The name of the output that corresponds
%   to that column is in the same column in the 'ouputheader'.
%
%   At the end of MEC.m the 'inputtable' and 'inputheader' are
%   combined in a struct: 'inp' and the 'outputtable' and 'outputheader'
%   are combined in a struct: 'outp'. Finally both structs
%   ('inp' and 'outp') are combined in a struct: 'struct'.
%
%   The results of the MEC model (MEC.m) can then be analysed.
%   'bldfig.m' is specially designed to analyse the results of 'MEC.m'.
%   To run 'bldfig.m', type: "bldfig" at the prompt.
%
%   Questions & info: Rob.Smetsers@gmail.com

clear;
clc;

%Inputvariables
%For the different radii and lengths the units are in [mm]

Br = 1.2;%Magnet remanent flux density
J = 6e6;%Current density is in A-mm^2 (ampere per square millimeter)
r1 = 0;%Radius 1 = outer diameter of the inner vacuum tube (no iron) = inner diameter of
the iron inner rod
r2 = 0;%Radius 2 = outer diameter of iron inner rod = inner diameter of the magnets
%r4 = variable; %Radius 4 = outer diameter of the magnets = inner diameter of airgap
airgap = 0.5; %The length of the airgap is 0.5 [mm]
%r5 = r4 + airgap; %The outer radius of the airgap = inner radius of the copper
r6 = 7;%The outer radius of the copper = inner radius of the outer iron = 7 [mm]
r8 = 8;%The outer radius of the outer iron = total radius of the tubular actuator = 8 [mm]
lmag=6; %The length of the magnets = 6 [mm]
lir=3;%The length of the iron inner spacer rings

bound=0.005;% While loop in satcal is continued untill the difference between current
%and previous saturation permeability < (bound*100) %, for all permeabilities!
maxit=700;% Maximum number of iterations. After this number of iterations, the process is
stopped.
```

```
%When the process is stopped, a checkbit ('check') warns for a non-converged solution.
%All the output parameters are set to 0 in this case.

i=0;%Initialisation of the parameter that stands for the current row of the inputtable

%Variables that are in a sweep
for r4 = r2+0.1: 0.1: r6-0.6
    i=i+1;

    %Creation of the inputtable
    inputtable(i,1)=Br;
    inputtable(i,2)=J;
    inputtable(i,3)=r1;
    inputtable(i,4)=r2;
    inputtable(i,5)=r4;
    inputtable(i,6)=airgap;
    inputtable(i,7)=r6;
    inputtable(i,8)=r8;
    inputtable(i,9)=lmag;
    inputtable(i,10)=lir;
    inputtable(i,11)=bound;
    inputtable(i,12)=maxit;
end

total = length(inputtable); % = i

%inputheader
inputheader = {'Br [Vs/m²]' 'J [A/m²]' 'Radius 1 [mm]' 'Radius 2 [mm]' 'Radius 4 [mm]'
'Airgap [mm]' 'Radius 6 [mm]' 'Radius 8 [mm]' 'Magnet length [mm]' 'Iron ring length [mm]'
'Boundary [%]' 'Maximum number of iterations []'};


%The 'inputtable' and 'inputheader' are completed so now the calculation of outputs is
started.

outputheader = {'Total flux [Vs]' 'Outer iron flux [VS]' 'Inner rod flux [Vs]' 'Leakage
flux [Vs]' 'Outer iron flux density [Vs/m²]' 'Inner rod flux density [Vs/m²]' 'Air gap
flux density [Vs/m²]' 'Electric loading [A/m]' 'Force [N]' 'Force to mass ratio [N/kg]'
'Mass [kg]' 'Inertia [kgm]' 'Number of iterations []' 'Force to mass + 0.025 ratio [N/kg]'
'Force to mass + 0.05 ratio [N/kg]' 'Force to mass + 0.075 ratio [N/kg]' 'Force to mass +
0.100 ratio [N/kg]' 'Check-bit'};

for j=1:total
    [phi1,phi2,phi3,Boiz,Brodz,Bgap,Q,F,mass,inertia,n,check] = satcal(inputtable(j,:));

    if check == 0 %Check is a checkbit for a converged solution, if a configuration has no
converged solution this bit is 1.
        outputtable(j,1)=phi2+phi3; %The total flux
        outputtable(j,2)=phi1; %The flux that is contributing to the force production (=
outer iron flux)
        outputtable(j,3)=phi3; %The flux (leaking) through the inner rod
        outputtable(j,4)=phi2-phi1; %The (axial) leakage flux in the airgap and copper
        outputtable(j,5)=Boiz; %The (axial) flux density in the outer iron
        outputtable(j,6)=Brodz; %The (axial) flux density in the inner rod
        outputtable(j,7)=Bgap; %The (radial) flux density in the airgap
        outputtable(j,8)=Q; %The electric loading
        outputtable(j,9)=F; %The force
        outputtable(j,10)=F/mass; %The force divided by the mover mass
        outputtable(j,11)=mass; %The mover mass
        outputtable(j,12)=inertia; %The mover inertia (= not calculated)
        outputtable(j,13)=n; %The number of iterations needed for the calculation
        outputtable(j,14)=4*F/(4*mass+25e-3); %For a 4 segment tubular motor 25 gram is
added to the mover mass
        outputtable(j,15)=4*F/(4*mass+50e-3); %                 "              50      "
        outputtable(j,16)=4*F/(4*mass+75e-3); %                 "              75      "
        outputtable(j,17)=4*F/(4*mass+100e-3); %                "             100      "
        outputtable(j,18)=check; %Check bit == 0 for converged solution

    else %if there are convergence problems; check != 0
        outputtable(j,1)=0;
        outputtable(j,2)=0;
```

```
            outputtable(j,3)=0;
            outputtable(j,4)=0;
            outputtable(j,5)=0;
            outputtable(j,6)=0;
            outputtable(j,7)=0;
            outputtable(j,8)=0;
            outputtable(j,9)=0;
            outputtable(j,10)=0;
            outputtable(j,11)=0;
            outputtable(j,12)=0;
            outputtable(j,13)=0;
            outputtable(j,14)=0;
            outputtable(j,15)=0;
            outputtable(j,16)=0;
            outputtable(j,17)=0;
            outputtable(j,18)=0;
    end
end


%creation of the structs 'inp', 'outp' and 'structx'

inp = struct('header',{inputheader},'table',{inputtable});
outp = struct('table',{outputtable},'header',{outputheader});
structx = struct('inputstruct',inp,'outputstruct',outp);
```

A.4.2 Matlab file of the Satcal function

```
%'satcal.m' is an iterative calculation of a reluctance network of a tubular linear motor.
%
%   The input(s) of 'satcal.m' is (are) generated in 'MEC.m'
%   'satcal.m' uses 'network.m' to calculate the flux in the different parts of the
scheme, for every iteration.
%
%   The output of 'satcal.m' is returned to and stored in the 'outputtable' of 'MEC.m'
%
%   A B-H characteristic of the iron is present in 'newbhs.m'. The function 'newbhs.m'
calculates from the input
%   'B' (a flux density in [Vs/m^2]) a new permeability of the (saturated) iron (u = B/H),
by a spline interpolation
%   of the B-H characteristic.

function [phi1,phi2,phi3,Boiz,Brodz,Bgap,Q,force,mass,inertia,n,check] = satcal(a);

%a = [Br,J,r1,r2,r4,r5,r6,r8,lmag,lir,bound,nmax]
%a is a row in the inputtable of 'MEC.m'

%The parameters that come from 'MEC.m'
Br = a(1,1);
J = a(1,2);
r1 = a(1,3);
r2 = a(1,4);
r4 = a(1,5);
airgap = a(1,6);
r5=r4+airgap;
r6 = a(1,7);
r8 = a(1,8);
lmag = a(1,9);
lir = a(1,10);
lir1 = 0.5*lir; %lir1 is extra parameter used to simplify calculation
bound = a(1,11);
nmax = a(1,12);

%Fixed other parameters
u0 = 4*pi*1e-7;% u0 is the permeability of vacuum
umag = 1.05*u0;% the permeability of the permanent magnetic material
rhomag = 7350;% mass density of magnetic material
rhoir = 7400;% mass density of iron
```

```
%Start of the iterative saturation calculation

check = 0; %check = a check-bit to verify a converged iterative solution

%Calculation of areas of flux tubes, remember that an area of a flux cube with
%flux in r-direction is not constant but increases with r. Therefor, a mean
%area is calculated. The area is calculated at the mean radius of the flux tube.

Aoiz = pi*((r8)^2-(r6)^2)*1e-6; % area or outer iron in z-direction
Aoir = pi*(r6+r5)*lir*1e-6; % mean value of area of outer rod in r-direction
Airr1 = ((3*r4+r2)/2)*pi*lir*1e-6;%2*pi*1/2*lir*....
Airr2 = ((r4+3*r2)/2)*pi*lir*1e-6;
Airz = pi*(r4^2-r2^2)*1e-6;
Arodr = pi*((3*r2+r1)/2)*lir*1e-6;
Arodz = pi*(r2^2-r1^2)*1e-6;

%Initial values of relative permeabilities
ureloiz=50;
ureloir=50;
urelirr1=50;
urelirr2=50;
urelirz=50;
urelrodr=50;
urelrodz=50;

%Initial previous values of relative permeabilities (differ from initial values, or
%solution is already converged!)
ureloizp=1; %Make sure 1 - (urel... / urel...p) >> bound
ureloirp=1;
urelirr1p=1;
urelirr2p=1;
urelirzp=1;
urelrodrp=1;
urelrodzp=1;

n=0; %Initialisation of the parameter that stands for the current iteration

%Check the convergence for iron parts saturation

%If 1 - (relative permeability now / relative permeability previous) > boundary value:
%recalculate the total structure, untill a converged solution, or the maximum number of
%iterations is reached

while abs(1-ureloiz/ureloizp)>bound | abs(1-ureloir/ureloirp)>bound | abs(1-
urelirr1/urelirr1p)>bound | abs(1-urelirr2/urelirr2p)>bound | abs(1-
urelirz/urelirzp)>bound | abs(1-urelrodr/urelrodrp)>bound | abs(1-
urelrodz/urelrodzp)>bound
    % calculate absolute permeabilities
    uoiz=ureloiz*u0;
    uoir=ureloir*u0;
    uirr1=urelirr1*u0;
    uirr2=urelirr2*u0;
    uirz=urelirz*u0;
    urodr=urelrodr*u0;
    urodz=urelrodz*u0;

    % calculate the airgap flux (phi1) and inner rod flux (phi2); use r5 and not airgap
(contrary to this function!)
    [phi1,phi2,phi3] = network
(Br,J,r1,r2,r4,r5,r6,r8,lmag,lir,uoiz,uoir,uirr1,uirr2,uirz,urodr,urodz,umag);

    % calculate the fluxdensity in respectively:
    Boiz = phi1/Aoiz;%The outer iron in z-direction
    Boir = phi1/Aoir;%The outer iron in r-direction
    Birr1 = phi2/Airr1;%The iron inter-spacer rings in r-direction on the outside (towards
airgap)
    Birr2 = phi3/Airr2;%The iron inter-spacer rings in r-direction on the inside (towards
inner rod)
    Birz = (phi2+phi3)/Airz; % The iron inter-spacer rings z-direction
```

```
if Arodz==0;   %If there is no inner rod (r2==r1)
    Brodr=0;
    Brodz=0;
else
    Brodr = phi3/Arodr;% The inner rod in r-direction
    Brodz = phi3/Arodz;% The inner rod in z-direction
end

% Axial flux in outer iron
uoizp=uoiz;
[uoizn,check1]=newbhs(Boiz);
% check1,-2,-3,-4,-5,-6 and -7 are checklists to register problems (out of bounds B-H
curve) in the errortable
ureloizp=uoizp/u0;
ureloizn=uoizn/u0;
if uoizn == 0
    ureloiz = 1;
else
    ureloiz=(5*ureloizp+ureloizn)/6;
end
uoirz = u0*ureloiz;

% Radial flux in outer iron
uoirp=uoir;
[uoirn,check2]=newbhs(Boir);
% check1, 2, 3 and 4 are checkbits to register problems in the errortable
ureloirp=uoirp/u0;
ureloirn=uoirn/u0;
if uoirn == 0
    ureloir = 1;
else
    ureloir=(5*ureloirp+ureloirn)/6;
end
uoir = u0*ureloir;

% Outer radial flux in iron rings
uirr1p=uirr1;
[uirr1n,check3]=newbhs(Birr1);
urelirr1p=uirr1p/u0;
urelirr1n=uirr1n/u0;
if uirr1n == 0
    urelirr1 = 1;
else
    urelirr1=(5*urelirr1p+urelirr1n)/6;
end
uirr1 = u0*urelirr1;

% Inner radial flux in iron rings
if Arodz==0
    urelirr2=1;
else
    uirr2p=uirr2;
    [uirr2n,check4]=newbhs(Birr2);
    urelirr2p=uirr2p/u0;
    urelirr2n=uirr2n/u0;
    if uirr2n == 0
        uirr2 = 1;
    else
        urelirr2=(5*urelirr2p+urelirr2n)/6;
    end
end
uirr2 = u0*urelirr2;

% Axial flux in iron rings
uirzp=uirz;
[uirzn,check5]=newbhs(Birz);
urelirzp=uirzp/u0;
urelirzn=uirzn/u0;
if uirzn == 0
    urelirz = 1;
else
```

```
        urelirz=(5*urelirzp+urelirzn)/6;
    end
    uirz = u0*urelirz;

    % Radial flux in inner rod
    if Arodz==0
        Brodr = 0;
        urelrodr = 1;
    else
        urodrp=urodr;
        [urodrn,check6]=newbhs(Brodr);
        urelrodrp=urodrp/u0;
        urelrodrn=urodrn/u0;
        if urodrn == 0
            urelrodr = 1;
        else
            urelrodr=(5*urelrodrp+urelrodrn)/6;
        end
    end
    urodr = u0*urelrodr;

    % Axial flux in inner rod
    if Arodz==0
        Brodz=0;
        urelrodz = 1;
    else
        urodzp=urodz;
        [urodzn,check3]=newbhs(Brodz);
        urelrodzp=urodzp/u0;
        urelrodzn=urodzn/u0;
        if urodzn == 0
            urelrodz = 1;
        else
            urelrodz=(5*urelrodzp+urelrodzn)/6;
        end
    end
    urodz = u0*urelrodz;


    n=n+1;

    if n>nmax
        check =1;
        fprintf('over the maximum number of iterations \n')
        n=nmax;
        a
        break
    end


    %The final calculation of the flux:

    [phi1,phi2,phi3] = network
(Br,J,r1,r2,r4,r5,r6,r8,lmag,lir,uoiz,uoir,uirr1,uirr2,uirz,urodr,urodz,umag);
    Boiz = phi1/Aoiz;
    if Arodz==0
        Brodz = 0;
    else
        Brodz = phi3/Arodz;
    end

    Bgap = phi1/(pi*(r6+r4)*lir*1e-6);

    lforce = min((lmag+lir)/6,lir1);%the hight (in z-direction) of the volume of the
lorentz-integral
    if lforce == lir1
        force = 2*(J*phi1)*(lforce/(lir1))*(r6-r5)*1e-3;
    elseif lir>lforce
        force = ((2*(J*(phi1/lir1))*lforce*(r6-r5)*1e-3) + ((lir1-lforce))*J*(phi1/lir)*(r6-
r5)*1e-3) ;%2*cos(pi/3)=1
    end
```

```
   mass = (Airz*lmag*1e-3*rhomag) + (2*Airz*lir1*1e-3*rhoir) +(pi*(r2^2-r1^2)*1e-
9*(lmag+2*lir1)*rhoir);

   inertia = 0;%A calculation of the inertia is not incorporated in this function yet'

   Q = J*(r6-r5);%The electric loading in [A/m]

end
```

A.4.3 Matlab file of the Network function

```
%'network.m' calculates a MEC model circuit for a subpart of a linear tubular machine
%using the parameters (Br,J,l1,r2,r4,r5,r6,l8,lmag,lir) it receives from 'satcal.m'
%
%    'network.m' returns: (phi1, phi2, phi3)
%    © RobSmetsers@gmail.com
%
%    This function is not written for a slotted stator but can be modified easily
%
%               _____   _____  phi3  phi1  _____    _____  phi1 _____    _____
%           -|_____|-|_____|-----------|_____|-----------|-------- |--------|---
%            | Rrodr  Rirr2  |              Rir1    Rgap  |    Roop    Roir   |
%            |                 |               |           |           |          |
%            |                 | | Rirz       |           |           |          |
%            |                 | |            |           |           |          |
%            |                 |              |           |           |          |
%            |                 |   |-------    |           |          |
%            | |               |   | |        | |         | |        | |
%  % Rroor   | |         phi(  '  )  | |Rmag   | | Rleak   | | Roiz
%            | |               |    | |        | |         | |        | |
%            |                 |     |          |           |          |
%            |                 | |-------       |           |          |
%            |                 |               |           |          |
%            |                 |   | |         |           |          |
%            |                 |   | | Rir2    |           |          |
%            |                 |   | |         |           |          |
%            | _____         |   _____     |  _____   _____   |
%           -|_____|-|_____|------------|_____|-----|_____|-----|_____|---
%              Rrodr   Rir2              Rir1      Rgap      Roor    Roir
%
% units are in mm
%
function [phi1,phi2,phi3]= inrodcal
(Br,J,r1,r2,r4,r5,r6,r8,lmag,lir,uoiz,uoir,uirr1,uirr2,uirz,urodr,urodz,umag)

u0 = 4*pi*1e-7;% u0 permeability of vacuum

r3 = (r4+r2)/2;%extra parameters that help in the calculation
r7 = (r8+r6)/2;
lir1 = 0.5*lir;
lir2 = 0.5*lir1;

if r4==r8
    phi1 = 0;
    phi2 = 0;
elseif r6==r8
    phi1 = 0;
    phi2 = 0;
else
    Amag = pi*((r4)^2-(r2)^2)*1e-6;
    phi = Br*Amag;
    Rmag = (lmag*1e-3)/(umag*Amag);

    Aoiz = pi*((r8)^2-(r6)^2)*1e-6;
    Roiz = ((lmag+lir1)*1e-3)/(uoiz*Aoiz);
```

```
    Roir = (1/(2*pi*uoir*lir1*1e-3))*log(r7/r6);

    %these 1 must be changed when using a slotted stator
    Rgap = (1/(2*pi*u0*lir1*1e-3))*log(r5/r4);
    Rcop = (1/(2*pi*u0*lir1*1e-3))*log(r6/r5);

    Rirr1 = (1/(2*pi*uirr1*lir1*1e-3))*log(r4/r3);

    Airz = pi*((r4)^2-(r2)^2)*1e-6;
    Rirz = (lir2*1e-3)/(uirz*Airz);

    Aleak =  pi*((r6)^2-(r4)^2)*1e-6;
    Rleak = ((lmag+lir1)*1e-3)/(u0*Aleak);


    if r2-r1==0
        Rrod = 10e100;
        Rirr2 = 10e100;
        Arod = 0;
    else
        Rirr2 = (1/(2*pi*uirr2*lir1*1e-3))*log(r3/r2);
        Rrodr = (1/(2*pi*urodr*lir1*1e-3))*log(r2/((r2+r1)/2));
        Arod = pi*((r2)^2-(r1)^2)*1e-6;
        Rrodz = ((lir1+lmag)*1e-3)/(urodz*Arod);
        Rrod = 2*Rrodr + Rrodz;
    end


    % calculation of equivalent reluctance
    Rrep1 = Roiz+2*(Rcop+Roir);
    Rrep2 = par(Rrep1,Rleak);
    Rrep3 = Rrep2+2*(Rirr1+Rgap);
    Rrep4 = Rrod+2*(Rirr2);
    Rrep5 = par(Rrep3,Rrep4);
    Rrep6 = Rrep5+2*Rirz;
    % calculation of circuit flux phic = phi2 + phi3 (see scheme)
    phic = (Rmag/(Rmag+Rrep6))*phi;
    % calculation of phi2 and phi3
    if r2-r1==0
        phi3 = 0;
    else
        phi3 = (phic*Rrep3)/((Rrep3+Rrep4));%originally Rrep4-Rrep3 and Rrep 5-Rrep4
    end

    phi2 = (phic*Rrep4)/(Rrep4+Rrep3);

    if abs(phic-(phi2+phi3))>1e-10
        fprintf ('\n reluctance calculation error! phic %d phi2 %d phi3 %d',phic, phi2,
phi3)
    end

    phil = (phi2*(Rleak))/(Rrep1+Rleak);

end

%extra function that calculates a replacement reluctance of two parallel reluctances.
function [Rreplace]=par(R1,R2)
Rreplace=(R1*R2)/(R1+R2);
```

Appendix B

B.1 Test set-up specifications

In figure B.1, an impression of the test set-up is shown. Half of the total mover is shown in this figure, and one fourth of the total stator is shown. In table B.1, values are assigned to the lengths in figure B.1.
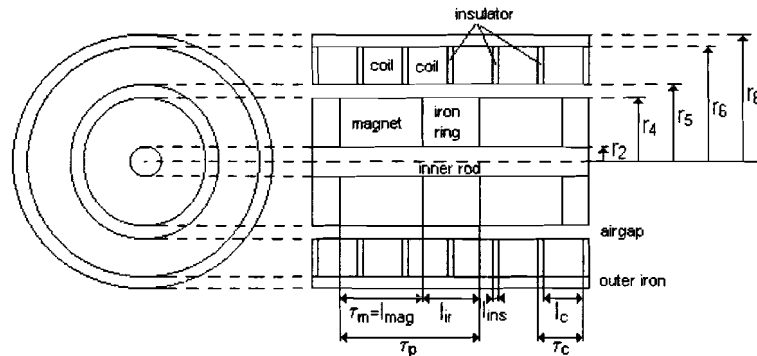

Figure B.1: *Impression of the test set-up*

Table B.1: Specifications of the test set-up

Parameter	Description	Value [unit]
τ_m	Magnet pitch (= l_{mag} (the magnet length))	6.0 / 8.0 *[mm]
τ_p	Pole pitch (= $l_{mag} + l_{ir}$ (where l_{ir} is the iron ring length))	10.6 [mm]
τ_c	Coil pitch (= 1/3 ($l_{mag} + l_{ir}$))	3.5 [mm]
r_2	Inner rod outer radius	1.6 [mm]
r_4	Mover outer radius	5.0 [mm]
r_5	Coil inner radius	5.5 [mm]
r_6	Coil outer radius	7.6 [mm]
r_8	Stator outer radius	8.5 [mm]
l_c	Length of the coil	2.9 [mm]
l_{ins}	Length of the insulators in between the coils	0.6 [mm]
n_{wc}	Number of windings per coil	39 [ ]
n_{cp}	Number of coils per phase	8 [ ]
n_m	Number of magnets on the mover	4 [ ]
n_{pp}	Number of pole pairs on the mover	2 [ ]
n_{ph}	Number of phases	3 [ ]
l_{mov}	Total mover length (iron rings at mover end included)	48 [mm]
l_{stat}	Total stator length for the coils (for the outer iron)	85 [mm] (90 [mm])
R_c	Resistance per coil	0.3 – 0.45 [Ω]
L_c	Inductance per coil	22 – 25 [μH]
R_{win}	Resistance per winding	3.5 – 3.7 [Ω]
L_{win}	Inductance per winding	250 – 300 [μH]

B.2 Permanent magnet specifications

The grade of the neodymium permanent magnet rings used in the test set-up is N38H. The characteristics of this Nd-Fe-B grade are shown in figure B.2 and B.3.
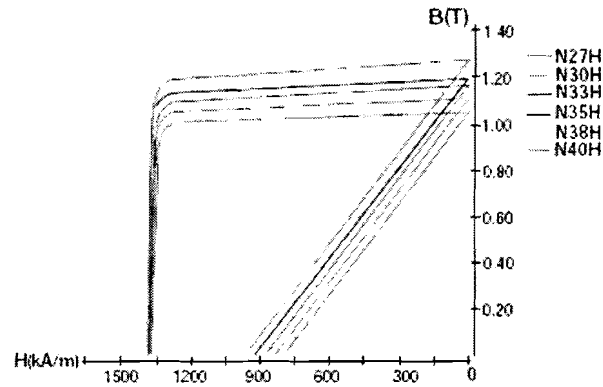

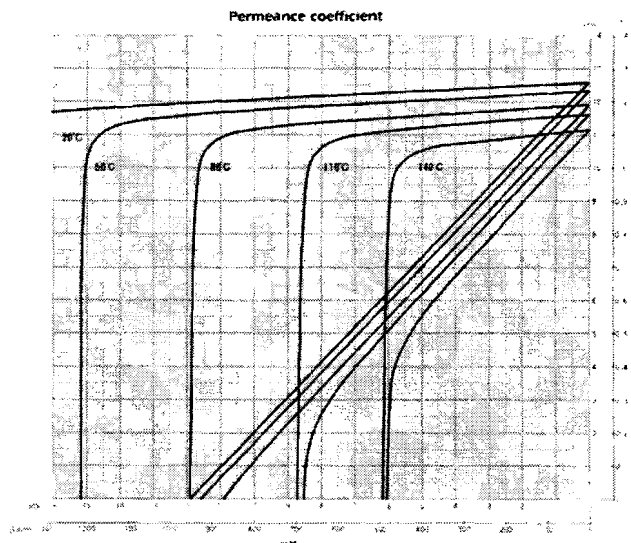*Figure B.2: The demagnetisation curve of various Nd-Fe-B grades*

Figure B.3: Temperature dependent demagnetisation curve of N38H

The operation point of the permanent-magnet material is derived in section 5.4. The magnetic flux density of the operation point is approximately 0.82 [T].
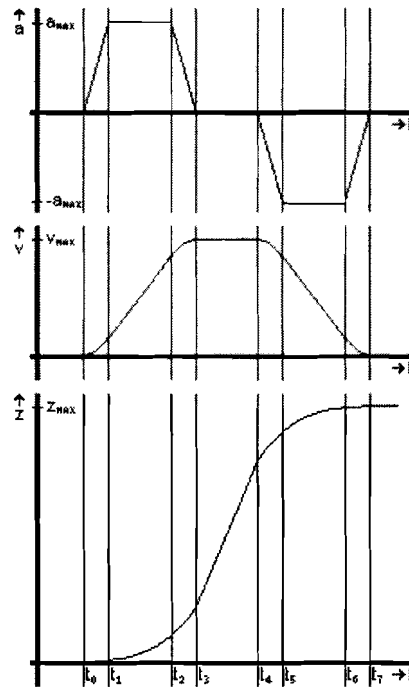
Appendix C

C.1 Linear motion analysis

Figure C.1: Profile of acceleration (a), velocity (v) and z-position (z) in one transition.

Movements of the actuator in z-direction are present in step 2, 4, 7 and 9 of the duty cycle (table 1.1). A profile of a translation containing acceleration (a), velocity (v) and z-position (z) is shown in figure C.1. The maximal jerk, acceleration and velocity of the current linear actuator are shown in table 2.1. Now, one translational stroke of the actuator as shown in figure C.1 will be analysed.

The jerk is identical for increasing and decreasing acceleration, so the time needed for reaching the maximum acceleration from zero acceleration and vice versa (in figure C.1: t_0 to t_1, t_2 to t_3 etc.) is:

$$t_{jt} = \frac{a_{max} - a_{min}}{j_{max}} = \frac{40}{12500} = 3.2 \cdot 10^{-3} \, [s]$$ (C.1)

It takes 3.2 ms before maximum acceleration or deceleration is reached. The time for constant acceleration and deceleration is $(t_1$ to t_2 and t_5 to t_6 in figure C.1):

$$t_{at} = \frac{v_{max}}{a_{max}} - t_{jt} = \frac{0.5}{40} - 3.2 \cdot 10^{-3} = 9.3 \cdot 10^{-3} \, [s]$$ (C.2)

The maximum acceleration (or deceleration) is present during $10.2 \cdot 10^{-3}$ $[s]$ in a transition between minimum and maximum velocity.

The time, the velocity of the translational stroke is constant, is $(t_3$ to t_4 in figure C.1) for the maximum stroke length of $30 \cdot 10^{-3}$ $[m]$:

$$t_{vt} = \frac{\Delta z_{max}}{v_{max}} - \frac{v_{max}}{a_{max}} - \frac{a_{max}}{j_{max}}$$

$$= \frac{30 \cdot 10^{-3}}{0.5} - \frac{0.5}{40} - \frac{40}{12500} = 44.3 \cdot 10^{-3} \, [s] \qquad (C.3)$$

The mover translates 44.3 10^{-3} $[s]$ at the maximum velocity of 0.5 $[ms^{-1}]$. For one translation from minimal z-position to extreme z-position (30 10^{-3} $[m]$) the time needed is:

$$t_{mt} = \frac{\Delta z_{max}}{v_{max}} + \frac{v_{max}}{a_{max}} + \frac{a_{max}}{j_{max}}$$

$$= \frac{30 \cdot 10^{-3}}{0.5} + \frac{0.5}{40} + \frac{40}{12500} = 75.7 \cdot 10^{-3} \qquad [s] \qquad (C.4)$$

C.2 Amplifier specification

Table C.1: Amplifier specifications

Type	Voltage controlled current source
Number of phases	3
Waveform	Genuine sinewave
Peak current per phase (rms current)	2.5 A (1.8 A rms)
Supply voltage (DC) (V_s)	46 V (± 4 V)
Voltage control	SVPWM

Appendix D

D.1 Specification sheet tubular actuator prototype

	Symbol	Unit	Simulation	Measurement
Actuator type		3-phase linear slotless synchronous		
Peak current (RMS)(Amplifier specification)	I_{peak}	[A]	1.8	
Peak force	F_{peak}	[N]	7.6	2.8
Max. continuous current (RMS) (coils @ 60 °C)	I_{cont}	[A]	0.7	
Continuous force	F_{cont}	[N]	3.0	0.8
Max. continuous power loss (coils @ 60 °C)	P_{cont}	[W]	4	
Force constant (F_{cont}/I_{cont})	k_F	$[NA^{-1}]$	4.2	1.6
EMF constant	k_F	$[Vsm^{-1}]$	3.1	2.9
Actuator constant	S	$[N^2W^{-1}]$	2.3	0.2
Pole pitch	T_p	[mm]	10.6	
Magnet pitch	τ_m	[mm]	6.0 or 8.0	
Resistance per phase	R_{ph}	$[\Omega]$	-	3.6
Inductance per phase	L_{ph}	[mH]	-	0.27
Length of mover	l_{mov}	[mm]	43	
Length of stator	l_{stat}	[mm]	85	